Title

Structural basis of NAD^+-cleavage activity by animal and plant TIR domains with functions in cell-death pathways

Authors

Shane Horsefield[1§], Hayden Burdett[1§], Xiaoxiao Zhang[2,3§], Mohammad K. Manik[1§], Yun Shi[4§], Jian Chen[2,3], Tiancong Qi[5], Jonathan Gilley[6,7], Jhih-Siang Lai[1], Maxwell X. Rank[1], Lachlan W. Casey[1], Weixi Gu[1], Daniel J. Ericsson[8], Gabriel Foley[1], Robert O. Hughes[9], Todd Bosanac[9], Mark von Itzstein[4], John P. Rathjen[3], Jeffrey D. Nanson[1], Mikael Boden[1], Ian B. Dry[10], Simon J. Williams[3], Brian J. Staskawicz[5], Michael P. Coleman[6,7], Thomas Ve[1,4*], Peter N. Dodds[2*] and Bostjan Kobe[1*]

Affiliations

[1]School of Chemistry and Molecular Biosciences, Institute for Molecular Bioscience and Australian Infectious Diseases Research Centre, University of Queensland, Brisbane, QLD 4072, Australia

[2]Agriculture and Food, Commonwealth Scientific and Industrial Research Organisation, Canberra, ACT 2601, Australia

[3]Plant Sciences Division, Research School of Biology, The Australian National University, Canberra 2601, Australia

[4]Institute for Glycomics, Griffith University, Southport, QLD 4222, Australia

[5]Department of Plant and Microbial Biology, University of California - Berkeley, Berkeley, California 94720, USA

[6]John van Geest Centre for Brain Repair, Department of Clinical Neurosciences, University of Cambridge, ED Adrian Building, Forvie Site, Robinson Way, Cambridge CB2 0PY, UK

[7]Babraham Institute, Babraham, Cambridge, CB22 3AT, UK

[8]Macromolecular Crystallography (MX) Beamlines, Australian Synchrotron, Melbourne, VIC 3168, Australia.

[9]Disarm Therapeutics, 400 Technology Square, 10th Floor, Cambridge, MA 02139 USA

[10]Agriculture and Food, Commonwealth Scientific and Industrial Research Organisation, Urrbrae, SA 5064, Australia

[§]These authors contributed equally to this work.

*Correspondence to: Bostjan Kobe (b.kobe@uq.edu.au), Thomas Ve (t.ve@griffith.edu.au), Peter Dodds (Peter.Dodds@csiro.au)

Short Title

NADase activity of animal and plant TIR domains

Abstract

SARM1 (sterile-α and TIR motif containing protein 1) plays a central role in NAD^+ depletion during Wallerian degeneration, a process that eliminates damaged axons following nerve injury and is shared with many neuropathies. We determined crystal structures of its SAM (sterile-α motif) and TIR (Toll/interleukin-1 receptor) domains. The tandem SAM domains form an octamer; mutations that disrupt the oligomeric structure impair axon degeneration. The TIR domain structure displays closest similarity to plant TIR domains. Like those from SARM1, the TIR domains from plant immune receptors L6 (flax) and RUN1 (grapevine) cleave NAD^+ into nicotinamide and ADP-ribose. Mutation of the predicted catalytic glutamate residue abolishes NADase activity as well as cell-death signaling *in planta*. The crystal structures of SARM1 TIR domain bound to ribose and RUN1 TIR domain bound to $NADP^+$ show that the ligand binds to a cleft conserved in SARM1 and RUN1. NAD^+ cleavage by TIR domains may represent a signaling mechanism in animal and plant cell-death pathways.

Main text

The TIR (Toll/interleukin-1 receptor (IL-1R)) domains are usually found in multi-domain proteins involved in innate immunity pathways in animals and plants (*1*). In mammals, TIR domains are located in the cytoplasmic regions of Toll-like receptors (TLRs) and IL-1Rs, as well as in the cytosolic adaptor proteins involved in inflammatory signaling downstream from these receptors (*2*). In these molecules, TIR domains function as protein-interaction modules; molecular and structural characterisation of TIR-domain signaling complexes in the TLR4 pathway has suggested a nucleated assembly of open-ended complexes consistent with the SCAF (signaling by cooperative assembly formation) mechanism prevalent in innate immunity pathways (*3-7*). The protein SARM1 functions both as a TLR adaptor and as a key executor of axon degeneration (*8-12*). In plants, TIR domains are most commonly found as the N-terminal signaling domains of cytoplasmic plant NLRs (nucleotide-binding (NB)/leucine-rich repeat (LRR) resistance (R) proteins). Plant NLRs directly or indirectly recognize effector proteins from pathogens and initiate defense responses, including the hypersensitive response (HR) characterized by localized cell death at the site of infection (*13*).

Axon degeneration is a hallmark of many neurological disorders (*14*), and understanding the molecular basis of SARM1-induced neuronal cell death may offer novel therapeutic options. Axonal injury is associated with the breakdown of NAD^+ (nicotinamide adenine dinucleotide) (*15*) and SARM1 was shown to accelerate NAD^+ depletion in nerves post-injury (*12, 16*). SARM1 is a modular protein with several domains (Fig. 1A). SARM1 lacking the armadillo (ARM) domain is constitutively active, suggesting that this domain has an autoinhibitory role (*17*). By contrast, disruption of the tandem sterile-α motif (SAM) domains abolishes SARM1 function

(*17*). SAM domains are found in numerous proteins with diverse roles and often form homo- or heterodimers and polymers (*18, 19*). Co-immunoprecipitation experiments suggest that the tandem SAM domains of SARM1 can mediate self-association of SARM1 (*17*). Forced self-association of SARM1 TIR domains induces axonal degeneration in the absence of injury, as a result of rapid NAD^+ depletion (*12*), and the TIR domain has recently been shown to have NAD^+-cleavage activity (*20*). Plant TIRs possess cell-death signaling capacity (*13*), but interacting partners or direct signaling pathway have not been defined to date.

In the current study, we determined the crystal structures of the tandem SAM domains and of the TIR domain of human SARM1, revealing the structural bases of self-association of the protein through its SAM domains and the enzymatic activity catalyzed by its TIR domain. SARM1 and plant TIR domain structures are highly similar and we show that TIR domains from the plant immune receptors L6 (flax, *Linum usitatissimum*) and RUN1 (grapevine, *Muscadinia rotundifolia*) also have NADase activity; we demonstrate the mechanistic basis through structural analysis. Collectively, this work suggests a conserved signaling mechanism involving nucleotide cleavage in cell-death pathways and provide a basis for rational drug design in the treatment of axonopathies.

Crystal structure of SARM1 tandem SAM domains reveals an octameric ring

Analysis of the tandem SAM domains of human SARM1 (residues 409-561, $hSARM1^{tSAM}$), produced in *E. coli,* by size-exclusion chromatography (SEC) coupled with multi-angle light scattering (MALS), suggested an octameric arrangement (Fig. 1B). A comparable average molecular mass was observed using the complementary

technique small-angle X-ray scattering (SAXS) (Fig. S1). In the crystal structure of hSARM1^{tSAM} (2.7 Å resolution; Table S1), each of the two SAM domains (hSARM1^{SAM1}, hSARM1^{SAM2}) adopts a characteristic five-α-helix bundle (α1-α5) separated by a 10-amino-acid linker (residues 477-486) (Fig. S2, S3; Table S2). In the asymmetric unit of the crystal, eight copies of hSARM1^{tSAM} form a ring (Fig. 1C). There are three major protein interaction interfaces in the octamer: an intramolecular hSARM1^{SAM1}:hSARM1^{SAM2} interface (1034 Å^2); and two intermolecular interfaces between the hSARM1^{SAM1} domains (966 Å^2) and between the hSARM1^{SAM2} domains (685 A^2; Fig. S4; Table S4).

Typically, SAM domains form open-ended polymeric structures (*19, 21*). SAM domains from 'translocation Ets leukemia', polyhomeotic, tankyrase-1, tankyrase-2, and caskin-1 polymers form open-ended left-handed helical assemblies via head-to-tail interactions of "ML" (mid-loop) and "EH" (end-helix) surfaces, with an axial rise and rotation per SAM domain subunit of 7.5-13.6 Å and 45-60°, respectively (Fig. S5). Superposition of these SAM domain polymers onto the hSARM1^{tSAM} octamer reveals that the ML:EH interfaces are similar, but the novel rigid association of the two SAM domains in hSARM1 results in no axial rise per hSARM1^{tSAM} subunit, with the 45° rotation per hSARM1^{tSAM} subunit leading to ring formation.

Oligomerization of SAM domains is necessary for the axon degeneration function of SARM1

Based on the hSARM1^{tSAM} crystal structure, we designed point mutations to disrupt the interaction interfaces and prevent octamer formation. All the tested single-residue mutations to alanine either resulted in insoluble proteins or showed no disruption of the

oligomer (Fig. S6). Therefore, we designed a mutant (hSARM1$^{tSAM(5Mut)}$) with five hydrophobic interface residues converted to arginines or aspartates (L442R, I461D, L514D, L531D, V533D; Fig. 1D, S4E-G). This mutant protein was soluble and monomeric based on SEC-MALS (Fig. 1B), as was its mouse counterpart mSARM1$^{tSAM(5Mut)}$ (Fig. S7). We then compared the abilities of exogenously expressed full-length, wild-type mSARM1^{wt} and mSARM1^{5Mut} to overcome the robust delay to injury-induced (Wallerian) degeneration of neurites in *Sarm1*$^{-/-}$ superior cervical ganglion (SCG) neuron cultures. Whereas mSARM1^{wt} restored rapid Wallerian degeneration, mSARM1^{5Mut} was expressed but essentially non-functional (Fig. 1E, S8). SAM-mediated oligomerization therefore plays a pivotal role in the axon degeneration activity of SARM1.

Crystal structure of SARM1^{TIR} domain reveals similarities to plant TIR domains

The TIR domain of human SARM1 (residues 560-700, hSARM1^{TIR}) expressed in *E. coli* behaves as a monomer in solution (SEC-MALS; Fig. S9). Its crystal structure (1.8 Å resolution; Fig. 2A; Table S1) shows more similarity with plant and TLR^{TIR} domains (DALI (*22*); Fig. 2B; Table S4) than bacterial TIR domains (as suggested by sequence analyses (*23*)). These comparisons also reveal close similarities with enzymes such as the bacterial *N*-glycosidase MilB that cleaves the nucleotide hydroxymethyl-CMP (cytidine 5'-monophosphate; Fig. 2C; Table S4). The structure of hSARM1^{TIR} contains a cleft (consisting of residues from the βA strand, the AA and BB loops, and the αB and αC helices; the elements of secondary structure are labelled sequentially (*1*)) with a bound glycerol molecule (glycerol was used as cryoprotectant). This region superimposes closely with the catalytic sites of MilB, as well as human CD38,

including a conserved catalytic glutamate residue (E103 in MilB, E226 in CD38) (Fig. 2C-D, S10). Structural evidence and the association of hSARM1 with NAD^+ depletion suggested it may bind NAD^+. Molecular docking analyses show that the cleft can accommodate the NMN portion of NAD^+, analogously to nucleotides binding to MilB and CD38 (Fig. S11). Using NMR (following the peak intensities of ^1H resonances of NAD^+ and its products; Fig. S12) and fluorescence (following the increase of fluorescence upon cleavage of the NAD^+ analogue εNAD, nicotinamide $1,N^6$ s-ethenoadenine dinucleotide (*24*)) assays, we observed that at high concentrations (5-20 μM), $hSARM1^{TIR}$ and $dSARM1^{TIR}$ (TIR domain from *Drosophila* SARM1) cleaved NAD^+ into nicotinamide (Nam) and ADP-ribose (ADPR) (Fig. 3A-B, S12, S13). We also observed that $hSARM1^{TIR}$ could cleave $NADP^+$ (into Nam and ADP-ribose 2'-phosphate [ADPRP]), but not NMN (nicotinamide mononucleotide), NaAD (nicotinic acid adenine dinucleotide) or FAD (flavin adenine dinucleotide) (Fig. S13). While this work was in progress, similar results were reported by Essuman et al (*20*), using HPLC-based assays. The E642A mutation in $hSARM1^{TIR}$ abolishes the NAD^+-cleavage activity, as do alanine mutations of the conserved active site residues Y568, R569, and R569+R570 (RRAA; Fig. 3A, S13).

The disproportional increase of $hSARM1^{TIR}$ activity with concentration suggests that self-association may be important for enzymatic activity (Fig. S13B), consistent with known mechanisms of TIR domain function (*3, 6, 25*). In agreement with the SAM domains facilitating self-association of the TIR domains in hSARM1, we observed that both the SAM and TIR domains of *Caenorhabditis elegans* SARM1 ($cSARM1^{tSAM-TIR}$), were required for NADase activity (Fig. 3B). The lower NADase activity of $cSARM1^{tSAM-TIR}$ compared to $hSARM1^{TIR}$ is consistent with the delay in neuronal cell-death in *C. elegans* (*26*). Kinetic parameters of $hSARM1^{tSAM-TIR}$ (expressed in NRK1-

HEK293T cells) were determined using a mass spectrometry-based assay (Fig. S14); several NAD^+ analogs showed moderate inhibition of this protein (Table S5).

The crystal packing of $hSARM1^{TIR}$ features two major self-association interfaces, an asymmetric BB loop-mediated one (796 $Å^2$) analogous to that observed in the MAL^{TIR} filament (*3*), and a pseudo-symmetric one (1452 $Å^2$) similar to the AE interface in plant TIRs (although largely mediated by the αA helices) (*6, 25*) (Fig. 2E-F, S15, S16; Table S6). Mutations in the BB-loop (D594A, E596K and G601P), αA helix (L579A) and EE loop (H685A) reduce the NADase activity of $hSARM1^{TIR}$ (Fig. 3A, S13), suggesting that both the BB-loop and AE interfaces observed in the $hSARM1^{TIR}$ crystals are functionally important (*12*).

In the crystal structure of the inactive BB-loop mutant $hSARM1^{TIR(G601P)}$ ("ligand-free"; 2.1 Å resolution; Table S1), the BB-loop interaction is modified, while the AE interface is intact (Fig. S17A). The BB loop folds over the catalytic cleft, with residue K597 inserted into the active site and interacting with E642 (via water molecules; no glycerol is present; Fig. S17B). This conformation may represent the inactive state $hSARM1^{TIR}$, presumably stabilized in this protein by the BB-loop mutation. In agreement, the K597E mutant of hSARM1 is active in NAD^+ depletion in axons (*26*). The structure of the inactive AE-interface mutant $hSARM1^{TIR(H685A)}$ (3.0 Å resolution; Table S1) reveals that the interactions between Y568, H685 and R570 in the AE interface are modified (Fig. S17C), yet the BB-loop interface is intact. Molecular dynamics simulations of monomeric and oligomeric $hSARM1^{TIR}$ reveal that the active site region is less flexible in the oligomeric form (Fig. S18, Table S7), suggesting that self-association may stabilize the BB-loop and the αB-helix region, reversing inhibition of the BB loop due to folding into the catalytic cleft. Jointly, our results suggest that

both the BB-loop and AE-interface interactions are required to stabilize the fully active enzyme conformation.

In NADases, a catalytic glutamate typically interacts with the C2 and C3 hydroxyl groups of the ribose, attached to the nicotinamide moiety in NAD^+. In the $hSARM1^{TIR}$ structure, E642 forms hydrogen bonds with the C2 and C3 hydroxyl groups of the glycerol molecule. Attempts to generate crystals of $hSARM1^{TIR}$ or its mutants bound to NAD^+-related ligands led to the structure of $hSARM1^{TIR}$ bound to ribose (1.8 Å resolution, Fig. S19). The C2 and C3 hydroxyl groups interact with the E642 carboxylate, with other hydroxyls interacting with Y568, R570, and D594. A chloride modelled near the ribose C5 atom, R569 and R570 likely occupies the position of the phosphate group attached to the C5 atom in the NMN moiety of NAD^+. The structure of the $hSARM1^{TIR(G601P)}$ (”MES-bound”; 1.7 Å resolution Table S1) bound to a molecule of MES (2-(N-morpholino) ethanesulfonic acid; Fig. S19F-H) also shows interaction of E642 and Y568 with the heterocyclic ring (replacing the interaction with K597), and R569 and R570 with the sulfonic-acid group of MES, which is located in a similar position to the chloride ion in the structure of the $hSARM1^{TIR}$:ribose complex. MES has been found to mimic ligands in other nucleotide-binding proteins (*27-29*).

Plant TIR domains cleave NAD^+

Plant TIR domains are found in NLRs, which recognize pathogen effector proteins and trigger HR, a process usually associated with localized cell death, to restrict pathogen infection. Isolated plant TIR domains can trigger cell death when transiently expressed *in planta,* in the absence of the corresponding pathogen effector proteins (referred to as autoactivity), dependent on two self-association interfaces (*6, 30*). Due to their

involvement in cell death and their structural similarities with hSARM1^{TIR}, we tested if plant TIR domains can also cleave NAD^+. At high protein concentrations, purified TIR domains from the NLRs L6 and RUN1 were capable of cleaving NAD^+ into Nam and ADPR (Fig. 3C). The catalytic activities were lower than that of hSARM1^{TIR} (Fig. 3D). As hSARM1^{TIR}, they were also able to cleave $NADP^+$ but not FAD (Fig. S20). Activity was not observed for the purified TIR domains from the NLRs RPS4, SNC1, RPP1, RPV1 or ROQ1 (Fig. S21A-B). When *E. coli* lysates (rather than pure proteins) were tested using an enzyme-linked cycling NAD^+-cleavage assay (*31*), NADase activity was observed also for RPS4^{TIR} (Fig. S22). Mutations of the residue equivalent to hSARM1^{TIR} E642 in L6^{TIR} and RUN1^{TIR} (E135A and E100A, respectively) abolished NAD^+-cleavage activity (Fig. 3C, S23A).

Self-association is important for the NADase activity of hSARM1^{TIR} and cell-death activities of plant TIRs. In agreement, addition of Ni-NTA beads to 6xHis-tagged L6^{TIR} and RUN1^{TIR} (Fig. S21C, S23B) and macromolecular crowding agents including PEG400 and PEG3350 (simulating crowded environment inside cells) stimulated NADase activities of L6^{TIR} and RUN1^{TIR}, and led to measurable activities for SNC1^{TIR}, RPP1^{TIR} and ROQ1^{TIR} (Fig. S21A-D).

Attempts to capture NAD^+-related ligands in crystals led to the structure of RUN1^{TIR} bound to $NADP^+$ (Fig. 3E-F, S24; Table S1). A molecule of Bis-Tris (2,2-bis(hydroxymethyl)-2,2',2"-nitrilotriethanol), a component of the crystallization solution, is in the catalytic site, while $NADP^+$ interacts with the periphery of the active site. W96 forms a face-to-face aromatic stacking arrangement with the adenosine group of $NADP^+$, with the C2' phosphate of the adenosine ribose in $NADP^+$ forming H-bonds with R34, G35, E36 and R39. The analogous C5' phosphate protrudes away from the binding site and the Nam moiety has no interpretable electron density. Bis-Tris interacts

with F33, G35, D60 and the catalytic E100. Mutations to residues in the proposed catalytic site affect effector-independent and effector-dependent HR in TIR domains and full-length NLRs, respectively (Table S8). Conserved residue mutation R34A, S94A, W96A, E100A in RUN1^{TIR} also greatly reduce NAD$^+$-cleavage activity (Fig. S21E). Double mutation of two arginine residues in the BB loop of RUN1^{TIR} (R64A+R65A) greatly increased NAD$^+$-cleavage activity (Fig. S21E, S23C-D). Mutation of the conserved glutamate in RUN1$^{TIR(R64A+R65A)}$ also abrogates NAD$^+$-cleavage activity (Fig. S21E).

Like most TIR domains, RUN1^{TIR} behaves as a monomer in solution (Fig. S25). In the crystals of RUN1^{TIR}, however, both the AE (1400 Å^2) and DE (1140 Å^2) interfaces common in plant TIR domains (*6, 25*) are observed (Fig. S26), comparable to the crystals of Arabidopsis SNC1^{TIR} (*6*). Mutations in the AE and DE interfaces of L6 perturb self-association of L6^{TIR} in solution and its cell-death signaling activity *in planta* (*6, 32*). Slight reduction in NADase activity was observed for the AE and DE interface mutants F79A, and R164E and K200R in L6^{TIR}, respectively (Fig. S23); importantly, PEG3350 did not stimulate the activity of interface mutants. Mutations in the proposed catalytic interface of L6^{TIR} (I104A and W131A) also resulted in a slight reduction in NAD$^+$-cleavage activity (Fig. S21F).

Implications of NADase activity for plant immunity

The observed NADase activity of plant TIR domains may play a role in the cell-death function of plant NLRs, possibly by a mechanism similar to hSARM1. To investigate whether hSARM1^{TIR} possesses cell-death activity in plants, the gene constructs encoding the C-terminal regions of hSARM1 were expressed transiently in *N.*

benthamiana leaves. Expression in *N. benthamiana* of hSARM1$^{tSAM\text{-}TIR}$, but not hSARM1^{TIR} or hSARM1^{tSAM}, induced cell death (Fig. 4A, S27A). Disruption of hSARM1$^{tSAM\text{-}TIR}$ oligomerisation by introduction of the five mutations (hSARM1$^{tSAM(5Mut)\text{-}TIR}$) abrogated cell death, indicating the need for SAM domain-induced hSARM1^{TIR} self-association in the cell-death process *in planta*. The E642A mutation in the hSARM1$^{tSAM\text{-}TIR}$ construct also disrupted cell death, implicating NAD^+-cleavage in the process.

Plant TIR-containing NLR signaling requires the downstream signaling component EDS1 (*33*). However, hSARM1$^{tSAM\text{-}TIR}$ induced HR when transiently expressed in *N. benthamina* eds1-1 knockout (*34*) lines (Fig. S28), implicating a mechanism different to plant TIR-induced HR, or NADase activity involving a separate pathway distinct from the EDS1-mediated signaling pathway.

Mutation of the conserved catalytic glutamate in each of L6^{TIR}-YFP, RUN1^{TIR}-YFP, SNC1^{TIR}-YFP and RPS4^{TIR}-YFP abrogated effector-independent HR in *N. benthamiana* (Fig. 4B, S27B). Mutation of the conserved glutamate (E135A) in the full-length L6 NLR abolished its ability to induce cell death in the presence of the AvrL567 ligand (Fig. 4C, S27C). Likewise, this mutation abolishes effector-independent signaling by the constitutively active L6^{D541V} variant (*35*). Strikingly, RUN1$^{TIR(R64A+R65A)}$, which has increased NAD^+-cleavage activity, also increased the strength of HR of YFP and Myc fusion proteins (Fig. S29). Consistent with the abrogated HR phenotypes observed for glutamate mutants, the data clearly implicate TIR NADase activity in the cell-death process.

Fusion of the oligomerising hSARM1^{tSAM} domain to L6^{TIRd28}-Myc, SNC1^{TIR}-Myc, RPS4^{TIR}-Myc and RUN1^{TIR}-Myc enhanced the cell-death induction of these proteins in

N. benthamiana, while fusion of the non-oligomerising hSARM1$^{tSAM(5Mut)}$ did not (Fig. 4D and S27D). Thus, like hSARM1^{TIR} neuronal degeneration activity, plant TIR-induced HR requires both the catalytic glutamate and the ability of the TIR to self-associate.

Bioinformatic analysis of TIR domains

For protein families with very limited sequence similarities, such as the TIR domains, phylogenetic analyses using sequence-based evolutionary models are not reliable (*36*). We therefore used a recently developed evolutionary model that is based on secondary structure (*37*) to construct a phylogeny of proteins structurally similar to hSARM1^{TIR} and plant TIR domains (Fig. S30). This analysis suggests that TIR domains are part of a large superfamily of enzymes, which includes a number of structurally-related proteins (not usually associated with TIR domains) that bind nucleotides (e.g. glycosyltransferases, nucleoside hydrolases and flavodoxins) or carbohydrates (e.g. bacterial isomerases) in the analogous region of the protein.

NAD$^+$-cleavage and cell-death activities of TIR domains

Here, we provide the first structural information for SARM1, a central effector of injury-induced axon degeneration. The structure of SARM1^{TIR} led us to further demonstrate NAD$^+$-cleavage activity for the TIR domains from plant NLRs.

The oligomeric structure of hSARM1^{tSAM} is different from other characterized SAM domains; the available data suggest their oligomerization is required for axon degeneration to aid self-association of TIR domains (Fig. 1). The ARM domain (by

interaction with the SAM and TIR domains) is suggested to hold hSARM1 in an inactive state (*17*); an unknown mechanism removes this auto-inhibition after axonal injury, allowing the TIR domains to self-associate, which activates the NADase activity and leads to axon degeneration (Fig. S31). Full-length SARM1 has been reported to self-associate (*12*), suggesting it may be constitutively oligomeric.

The structure of hSARM1^{TIR} shows closest similarities to the TIR domains from plant NLRs and TLRs (Fig. 2). The putative catalytic glutamate is structurally conserved in plant TIR domains, and they show NAD^+-cleavage activity. Although TLR TIR domains also have glutamate residues in the analogous region, these are not found in the same spatial locations (Fig. 2). Interestingly, the equivalent glutamate appears to be conserved in many bacterial TIR domains, and some bacterial TIR domains have been shown to possess NAD^+-cleavage activity (*38*); however, in the two bacterial TIR domains with known structures (*39-42*), the analogous regions of the proteins differ from those in hSARM1^{TIR} and plant TIR domains, with the Cα of the glutamate is located >6 Å away (Fig. 2). The active site of hSARM1^{TIR} is also structurally similar to the ecto-domain of the transmembrane glycoprotein CD38 (Fig. S10**)**.

The structures of hSARM1^{TIR} and RUN1^{TIR} in the presence of ligands uncover specific substrate:enzyme interactions, as supported by our modelling of substrate binding (Fig. S11). The ligand-bound structures represent excellent starting points for structure-based inhibitor design to target neurodegenerative disease.

The structures also shed light on the likely conformational changes required for the activation of NAD^+-cleavage activity and the possible role of TIR-domain self-association in the process. The "ligand-free" hSARM1$^{TIR(G601P)}$ structure suggests that when not engaged in intermolecular interactions, the BB-loop K597 residue interacts

with the catalytic glutamate (E642). Considering further the R64A+R65A mutation in RUN1, the BB loop may act as a gate for ligand entry. We propose that the activation model may include the following steps: before activation, the interaction of BB-loop K597 with E642 prevents enzymatic activity; presumably, the N-terminal domain of hSARM1 stabilizes this conformation. Upon axon injury, the SAM-domain assembly facilitates TIR domain association (analogous to the NLRs causing caspase-recruitment domain association (*43*)) through the BB-loop interface, removing K597 from its inhibitory interaction. Further TIR-domain association through the AE interface facilitates the interactions of H685 and R570, leading to optimal configuration of the active site, NAD^+ cleavage and axon degeneration.

TIR domains have a flavodoxin fold common to many proteins with diverse functions, and our bioinformatic analyses suggest evolutionary relationships between TIR domains and other structurally related proteins. Our analyses reveal that the TIR domains from hSARM1 and plant NLRs are related to a number of proteins with enzymatic activities such as nucleotide and carbohydrate hydrolysis, consistent with the observed NAD^+-cleavage activity in these TIR domains. The TIR domains in some other branches may have lost enzymatic activity but retained scaffolding protein:protein interaction functions.

Downstream signaling by plant NLR TIR domains has remained a mystery despite substantial efforts by many groups, with no direct signaling partners identified. Could the observed NAD^+-cleavage activity of TIR domains represent the "effector function" (*25*) responsible for the signaling event? Plant TIR-domain cell-death signaling is EDS1-dependent (*33*). However, $hSARM1^{tSAM\text{-}TIR}$ induces cell death in *eds1-1 N. benthamiana* lines. $hSARM1^{TIR}$ hydrolyzes NAD^+ much more rapidly than the plant TIR domains examined and thus may be causing necrosis through depletion of NAD^+

and in turn ATP, as suggested for axons. Plant TIRs may signal cell death via a more controlled pathway mediated by EDS1 (Fig. S31B). Alternatively, the NAD^+ hydrolysis catalysed by plant TIRs may be part of a different pathway to the EDS1-mediated signaling pathway.

Consequently, the products of NAD^+ hydrolysis may be involved in cell-death signaling. Cyclic ADPR (cADPR), produced by $hSARM1^{TIR}$ (*20*) and CD38 (*28*), has been shown to stimulate Ca^{2+} influx as part of NLR-mediated HR through Ca^{2+}-channels, and is also involved in both abscisic-acid and salicylic-acid signaling pathways (*44*). NaADP is also involved in Ca^{2+} signaling in plants, although the enzymes responsible for its synthesis are unknown (*45*). It is possible that the NB domains of plant NLRs could play a role in the hydrolysis of NAD^+, by providing an oligomeric platform for TIR-domain self-association, binding of the ADP group of NAD^+ and removing the cleaved ADPR group. Proteins structurally related to TIR domains have nucleotide-transfer activities (e.g. ADP-ribosylation), and many ADP-ribosylases show low enzymatic activity in the absence of the target of ribosylation (*46*), which could explain the low NADase activities of plant TIR domains. Alternatively, the low NADase activities may be due to poor self-association abilities of isolated plant TIR domains, supported by the stimulation of activity using affinity beads, macromolecular crowding reagents and in cell lysates, or NAD^+ may not be the preferred substrate (many NADases show high substrate promiscuity (*47*)). In summary, our results provide a foundation for future work on the role of NADase activity in plant immunity, and development of inhibitors of axon degeneration.

References and Notes

1. T. Ve, S. J. Williams, B. Kobe, Structure and function of Toll/interleukin-1 receptor/resistance protein (TIR) domains. *Apoptosis* **20**, 250-261 (2015).
2. N. J. Gay, M. F. Symmons, M. Gangloff, C. E. Bryant, Assembly and localization of Toll-like receptor signalling complexes. *Nat. Rev. Immunol.* **14**, 546-558 (2014).
3. T. Ve, P. R. Vajjhala, A. Hedger, T. Croll, F. DiMaio, S. Horsefield, X. Yu, P. Lavrencic, Z. Hassan, G. P. Morgan, A. Mansell, M. Mobli, A. O'Carroll, B. Chauvin, Y. Gambin, E. Sierecki, M. J. Landsberg, K. J. Stacey, E. H. Egelman, B. Kobe, Structural basis of TIR-domain-assembly formation in MAL- and MyD88-dependent TLR4 signaling. *Nat. Struct. Mol. Biol.* **24**, 743-751 (2017).
4. P. R. Vajjhala, T. Ve, A. Bentham, K. J. Stacey, B. Kobe, The molecular mechanisms of signaling by cooperative assembly formation in innate immunity pathways. *Mol. Immunol.* **86**, 23-37 (2017).
5. S. Latty, J. Sakai, L. Hopkins, B. Verstak, T. Paramo, N. A. Berglund, N. J. Gay, P. J. Bond, D. Klenerman, C. E. Bryant, Activation of Toll-like receptors nucleates assembly of the MyDDosome signaling hub. *Elife* **7**, (2018).
6. X. Zhang, M. Bernoux, A. R. Bentham, T. E. Newman, T. Ve, L. W. Casey, T. M. Raaymakers, J. Hu, T. I. Croll, K. J. Schreiber, B. J. Staskawicz, P. A. Anderson, K. H. Sohn, S. J. Williams, P. N. Dodds, B. Kobe, Multiple functional self-association interfaces in plant TIR domains. *Proc. Natl. Acad. Sci. U. S. A.* **114**, E2046-E2052 (2017).
7. M. T. Nishimura, R. G. Anderson, K. A. Cherkis, T. F. Law, Q. L. Liu, M. Machius, Z. L. Nimchuk, L. Yang, E. H. Chung, F. El Kasmi, M. Hyunh, E. Osborne Nishimura, J. E. Sondek, J. L. Dangl, TIR-only protein RBA1 recognizes a pathogen effector to regulate cell death in Arabidopsis. *Proc. Natl. Acad. Sci. U. S. A.* **114**, E2053-E2062 (2017).
8. M. Carty, R. Goodbody, M. Schroder, J. Stack, P. N. Moynagh, A. G. Bowie, The human adaptor SARM negatively regulates adaptor protein TRIF-dependent Toll-like receptor signaling. *Nat. Immunol.* **7**, 1074-1081 (2006).
9. P. Panneerselvam, J. L. Ding, Beyond TLR signaling-the role of SARM in antiviral immune defense, apoptosis & development. *Int. Rev. Immunol.* **34**, 432-444 (2015).
10. J. M. Osterloh, J. Yang, T. M. Rooney, A. N. Fox, R. Adalbert, E. H. Powell, A. E. Sheehan, M. A. Avery, R. Hackett, M. A. Logan, J. M. MacDonald, J. S. Ziegenfuss, S. Milde, Y. J. Hou, C. Nathan, A. Ding, R. H. Brown, Jr., L. Conforti, M. Coleman, M. Tessier-Lavigne, S. Zuchner, M. R. Freeman, dSarm/Sarm1 is required for activation of an injury-induced axon death pathway. *Science* **337**, 481-484 (2012).
11. Y. Kim, P. Zhou, L. Qian, J. Z. Chuang, J. Lee, C. Li, C. Iadecola, C. Nathan, A. Ding, MyD88-5 links mitochondria, microtubules, and JNK3 in neurons and regulates neuronal survival. *J. Exp. Med.* **204**, 2063-2074 (2007).
12. J. Gerdts, E. J. Brace, Y. Sasaki, A. DiAntonio, J. Milbrandt, SARM1 activation triggers axon degeneration locally via NAD(+) destruction. *Science* **348**, 453-457 (2015).

13. P. N. Dodds, J. P. Rathjen, Plant immunity: towards an integrated view of plant-pathogen interactions. *Nat. Rev. Genet.* **11**, 539-548 (2010).
14. J. Gerdts, D. W. Summers, J. Milbrandt, A. DiAntonio, Axon self-destruction: new links among SARM1, MAPKs, and NAD+ metabolism. *Neuron* **89**, 449-460 (2016).
15. J. Wang, Q. Zhai, Y. Chen, E. Lin, W. Gu, M. W. McBurney, Z. He, A local mechanism mediates NAD-dependent protection of axon degeneration. *J. Cell Biol.* **170**, 349-355 (2005).
16. Y. Sasaki, T. Nakagawa, X. Mao, A. DiAntonio, J. Milbrandt, NMNAT1 inhibits axon degeneration via blockade of SARM1-mediated NAD(+) depletion. *Elife* **5**, (2016).
17. J. Gerdts, D. W. Summers, Y. Sasaki, A. DiAntonio, J. Milbrandt, Sarm1-mediated axon degeneration requires both SAM and TIR interactions. *J. Neurosci.* **33**, 13569-13580 (2013).
18. M. J. Knight, C. Leettola, M. Gingery, H. Li, J. U. Bowie, A human sterile alpha motif domain polymerizome. *Protein Sci.* **20**, 1697-1706 (2011).
19. F. Qiao, J. U. Bowie, The many faces of SAM. *Sci. STKE* **2005**, re7 (2005).
20. K. Essuman, D. W. Summers, Y. Sasaki, X. Mao, A. DiAntonio, J. Milbrandt, The SARM1 Toll/interleukin-1 receptor domain possesses intrinsic NAD+ cleavage activity that promotes pathological axonal degeneration. *Neuron* **93**, 1334-1343 e1335 (2017).
21. M. Bienz, Signalosome assembly by domains undergoing dynamic head-to-tail polymerization. *Trends Biochem. Sci.* **39**, 487-495 (2014).
22. L. Holm, L. M. Laakso, Dali server update. *Nucleic Acids Res.* **44**, W351-355 (2016).
23. Q. Zhang, C. M. Zmasek, X. Cai, A. Godzik, TIR domain-containing adaptor SARM is a late addition to the ongoing microbe-host dialog. *Dev. Comp. Immunol.* **35**, 461-468 (2011).
24. G. Pergolizzi, J. N. Butt, R. P. Bowater, G. K. Wagner, A novel fluorescent probe for NAD-consuming enzymes. *Chem. Commun.* **47**, 12655-12657 (2011).
25. S. Nimma, T. Ve, S. J. Williams, B. Kobe, Towards the structure of the TIR-domain signalosome. *Curr. Opin. Struct. Biol.* **43**, 122-130 (2017).
26. D. W. Summers, D. A. Gibson, A. DiAntonio, J. Milbrandt, SARM1-specific motifs in the TIR domain enable NAD+ loss and regulate injury-induced SARM1 activation. *Proc. Natl. Acad. Sci. USA* **113**, E6271-E6280 (2016).
27. N. Czudnochowski, A. L. Wang, J. Finer-Moore, R. M. Stroud, In human pseudouridine synthase 1 (hPus1), a C-terminal helical insert blocks tRNA from binding in the same orientation as in the Pus1 bacterial homologue TruA, consistent with their different target selectivities. *J. Mol. Biol.* **425**, 3875-3887 (2013).
28. Q. Liu, R. Graeff, I. A. Kriksunov, H. Jiang, B. Zhang, N. Oppenheimer, H. Lin, B. V. Potter, H. C. Lee, Q. Hao, Structural basis for enzymatic evolution from a dedicated ADP-ribosyl cyclase to a multifunctional NAD hydrolase. *J. Biol. Chem.* **284**, 27637-27645 (2009).
29. S. Han, J. A. Craig, C. D. Putnam, N. B. Carozzi, J. A. Tainer, Evolution and mechanism from structures of an ADP-ribosylating toxin and NAD complex. *Nat. Struct. Biol.* **6**, 932-936 (1999).

30. X. Zhang, P. N. Dodds, M. Bernoux, What do we know about NOD-like receptors in plant immunity? *Annu. Rev. Phytopathol.* **55**, 205-229 (2017).
31. Y. Gibon, F. Larher, Cycling assay for nicotinamide adenine dinucleotides: NaCl precipitation and ethanol solubilization of the reduced tetrazolium. *Anal. Biochem.* **251**, 153-157 (1997).
32. M. Bernoux, T. Ve, S. Williams, C. Warren, D. Hatters, E. Valkov, X. Zhang, J. G. Ellis, B. Kobe, P. N. Dodds, Structural and functional analysis of a plant resistance protein TIR domain reveals interfaces for self-association, signaling, and autoregulation. *Cell Host Microbe* **9**, 200-211 (2011).
33. M. Wiermer, B. J. Feys, J. E. Parker, Plant immunity: the EDS1 regulatory node. *Curr. Opin. Plant Biol.* **8**, 383-389 (2005).
34. A. Schultink, T. Qi, A. Lee, A. D. Steinbrenner, B. Staskawicz, Roq1 mediates recognition of the Xanthomonas and Pseudomonas effector proteins XopQ and HopQ1. *Plant J.* **92**, 787-795 (2017).
35. M. Bernoux, H. Burdett, S. J. Williams, X. Zhang, C. Chen, K. Newell, G. J. Lawrence, B. Kobe, J. G. Ellis, P. A. Anderson, P. N. Dodds, Comparative analysis of the flax immune receptors L6 and L7 suggests an equilibrium-based switch activation model. *Plant Cell* **28**, 146-159 (2016).
36. C. P. Ponting, R. R. Russell, The natural history of protein domains. *Annu. Rev. Biophys. Biomol. Struct.* **31**, 45-71 (2002).
37. J. S. Lai, B. Rost, B. Kobe, M. Boden, Evolutionary model of protein secondary structure capable of revealing new biological relationships. *bioRxiv* 563452, doi: 10.1101/563452 (2019).
38. K. Essuman, D. W. Summers, Y. Sasaki, X. Mao, A. K. Y. Yim, A. DiAntonio, J. Milbrandt, TIR domain proteins are an ancient family of NAD(+)-consuming enzymes. *Curr. Biol.* **28**, 421-430 e424 (2018).
39. S. L. Chan, L. Y. Low, S. Hsu, S. Li, T. Liu, E. Santelli, G. Le Negrate, J. C. Reed, V. L. Woods, Jr., J. Pascual, Molecular mimicry in innate immunity: crystal structure of a bacterial TIR domain. *J. Biol. Chem.* **284**, 21386-21392 (2009).
40. M. Alaidarous, T. Ve, L. W. Casey, E. Valkov, D. J. Ericsson, M. O. Ullah, M. A. Schembri, A. Mansell, M. J. Sweet, B. Kobe, Mechanism of bacterial interference with TLR4 signaling by Brucella Toll/interleukin-1 receptor domain-containing protein TcpB. *J. Biol. Chem.* **289**, 654-668 (2014).
41. B. Kaplan-Turkoz, T. Koelblen, C. Felix, M. P. Candusso, D. O'Callaghan, A. C. Vergunst, L. Terradot, Structure of the Toll/interleukin 1 receptor (TIR) domain of the immunosuppressive Brucella effector BtpA/Btp1/TcpB. *FEBS Lett.* **587**, 3412-3416 (2013).
42. G. A. Snyder, D. Deredge, A. Waldhuber, T. Fresquez, D. Z. Wilkins, P. T. Smith, S. Durr, C. Cirl, J. Jiang, W. Jennings, T. Luchetti, N. Snyder, E. J. Sundberg, P. Wintrode, T. Miethke, T. S. Xiao, Crystal structures of the Toll/Interleukin-1 receptor (TIR) domains from the Brucella protein TcpB and host adaptor TIRAP reveal mechanisms of molecular mimicry. *J. Biol. Chem.* **289**, 669-679 (2014).
43. M. Matyszewski, W. Zheng, J. Lueck, B. Antiochos, E. H. Egelman, J. Sohn, Cryo-EM structure of the NLRC4(CARD) filament provides insights into how symmetric and asymmetric supramolecular structures drive inflammasome assembly. *J. Biol. Chem.* **293**, 20240-20248 (2018).

44. L. Hunt, F. Lerner, M. Ziegler, NAD – new roles in signalling and gene regulation in plants. *New Phytol.* **163**, 31-44 (2004).
45. B. Gakière, J. Hao, L. De Bont, P. Pétriacq, A. Nunes-Nesi, A. R. Fernie, NAD+ biosynthesis and signaling in plants. *Crit. Rev. Plant Sci.* **2018**, 1-49 (2018).
46. N. J. Oppenheimer, A. J. Handlon, in *The Enzymes,* D. S. Sigman, Ed. (Academic Press, 1992).
47. H. C. Lee, Structure and enzymatic functions of human CD38. *Mol. Med.* **12**, 317-323 (2006).
48. M. Landau, I. Mayrose, Y. Rosenberg, F. Glaser, E. Martz, T. Pupko, N. Ben-Tal, ConSurf 2005: the projection of evolutionary conservation scores of residues on protein structures. *Nucleic Acids Res.* **33**, W299-302 (2005).

Acknowledgements

We acknowledge the use of the University of Queensland Remote Operation Crystallization and X-Ray Diffraction (UQ-ROCX) Facility and the macromolecular crystallography (MX) and small/wide angle X-ray scattering (SAXS/WAXS) beamlines at the Australian Synchrotron, Victoria, Australia. MD simulations were performed on the High Performance Computing Cluster "Gowonda" at Griffith University. We thank Nicholas Deerain for technical contributions.

Funding

The work was supported by the National Health and Medical Research Council (NHMRC grants 1107804 and 1160570 to BK, TV; 1071659 to BK; and 1108859 to TV) and Australian Research Council (ARC; DP160102244 and DP190102526 to BK, PND). BK is NHMRC Principal Research Fellow (1110971) and ARC Laureate Fellow (FL180100109). TV is the recipient of ARC DECRA (DE170100783). JC is the recipient of a Chinese Scholarship Council (CSC) post-graduate scholarship. YS is Griffith University Postdoctoral Fellow. JG was supported by the UK Medical Research Council and MPC by the John and Lucille van Geest Foundation. MKM is supported by the Australian Government Research Training Program (RTP).

Author Contributions

Designed research: SH, HB, XZ, MKM, YS, JG, ROH, TB, SJW, TV, PD, BK; performed research: SH, HB, XZ, MKM, YS, JG, JC, LWC, TQ, JSL, WG, MXR, DJE, GF, ROH, TB, TV; analyzed data: SH, HB, XZ, MKM, YS, JG, LWC, ROH, TB, JSL, MXR, DJE, GF, MvI, JPR, JDN, MB, IBD, BJS, SJW, MPC, TV, PND,

BK; wrote the paper: SH, HB, XZ, MKM, YS, TV, BK; edited and contributed to writing: all authors.

Competing interests

BK is a consultant for Disarm Therapeutics. BK and SH receive research funding from Disarm Therapeutics.

Data and materials availability

Coordinates and structure factors for all crystal structures determined in this study have been deposited in the Protein Data Bank (see Supplementary Information).

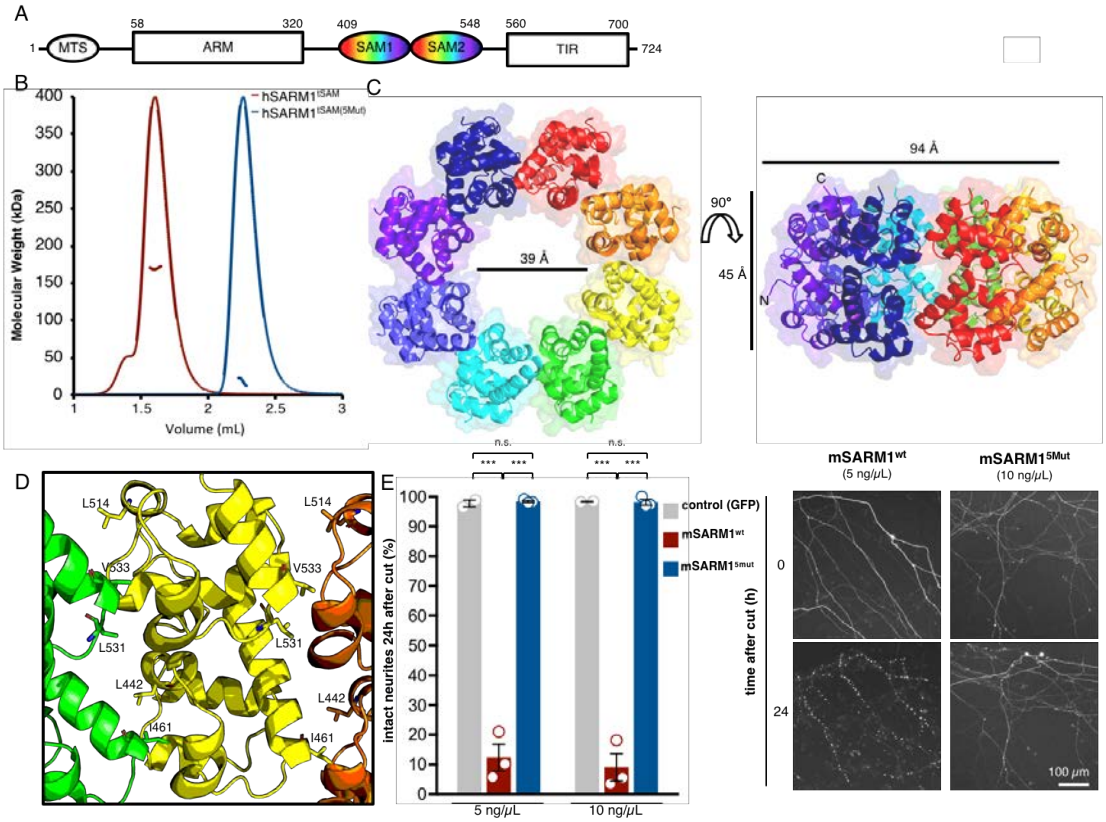

Fig. 1. Octameric structure of hSARM1^{tSAM} is important for function. (**A**) Schematic diagram of the SARM1 domain architecture. (**B**) Solution properties of hSARM1^{tSAM} (wild-type; red) and hSARM1$^{tSAM(5Mut)}$ (blue), analyzed by SEC-MALS. Peaks indicate the traces from the refractive index (RI) detector during SEC; the lines under the peaks correspond to the average molecular mass distributions across the peak. The average molecular mass of hSARM1^{tSAM} is 169.8 kDa (± 0.5%), most consistent with an octamer (theoretical molecular mass 161.9 kDa). (**C**) Cartoon representation of the octameric ring assembly of hSARM1^{tSAM} molecules observed in the asymmetric unit of the crystal. (**D**) Residues mutated in hSARM1$^{tSAM(5Mut)}$. (**E**) Exogenously expressed mSARM1^{wt}, but not mSARM1^{5Mut} restores the ability of *Sarm1*$^{-/-}$ neurites to degenerate after cut. Constructs for mouse SARM1 variants were injected along with DsRed vector (40 ng/µL) to allow visualisation of neurites of the injected neurons. The percentage of intact neurites at 24 h after cut, relative to those present at the time of

transection, is plotted (left, individual values and means ± SEM are shown). Representative images of cut neurites at the time of transection (0 h) and at 24 h are shown (right). mSARM1^{5Mut} does not promote degeneration of cut *Sarm1*$^{-/-}$ neurites even at the highest concentration used (n.s. = not significant [$p > 0.05$] and *** $p < 0.001$, separate one-way ANOVA for each concentration with Tukey's multiple comparison tests). mSARM1^{5Mut} is expressed at the expected size and at a higher level than mSARM1^{wt} both in injected SCG neurons and transfected HEK cells (Fig. S8).

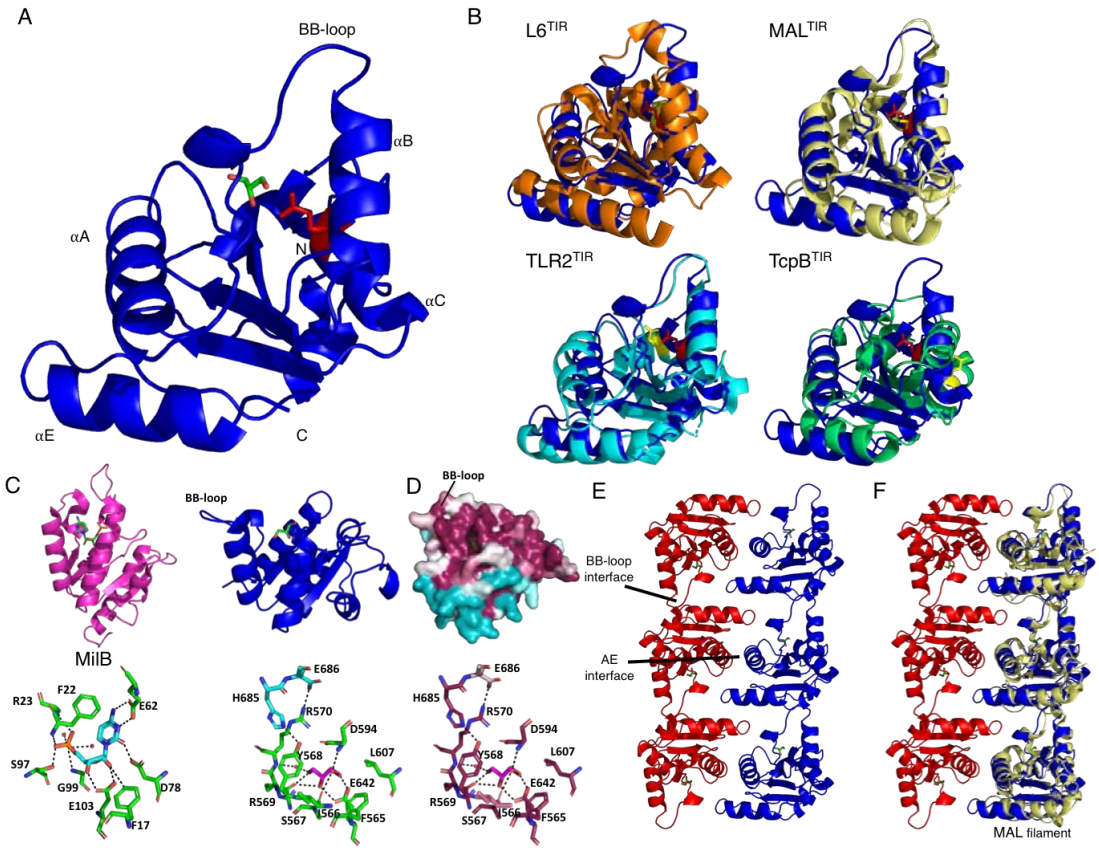

Fig. 2. hSARM1^{TIR} crystal structure. (**A**) Structure of hSARM1^{TIR} (cartoon representation; catalytic E642 (red) and glycerol (green) in stick representation). (**B**) Superposition of representative TIR domains from plant NLRs (L6; orange), TLR adaptors (MAL; yellow), TLRs (TLR2; cyan) and bacterial TIR domain-containing proteins (TcpB; green) onto hSARM1^{TIR} (blue). The glutamates equivalent to hSARM1^{TIR} E642 are shown in stick representation. (**C**) Comparison of the catalytic pockets of hSARM1^{TIR} and MilB. Cartoon representation of the crystal structure of MilB (purple) bound to CMP (green) (Protein Data Bank [PDB] ID 4jem); below, rotated 180°, stick representation of residues in the catalytic pocket (green) coordinating with the ligand (cyan), and hSARM1^{TIR} structure (blue) bound to glycerol (green) with stick representation of residues in the catalytic pocket. (**D**) Surface representation of hSARM1^{TIR} of the catalytic pocket with glycerol bound (in stick representation), as shown in (C). The surface residues are colored by sequence

conservation calculated using ConSurf (*48*), based on multiple sequence alignment of 150 unique TIR domain sequences of predicted orthologs with sequence identities to hSARM1 ranging from 35-95%. Cyan and purple correspond to variable and conserved regions, respectively. (**E**) hSARM1^{TIR} crystal packing. Three hSARM1^{TIR} molecules are shown in each of the antiparallel strands (colored red and blue); each strand features a head-to-tail arrangement via the BB-loop (interacting with DE, βE and αE regions) interface. The association between strands is via the AE interface. (**F**) Superposition of one strand of the MAL proto-filament (*3*) (yellow) onto the crystal packing arrangement of hSARM1^{TIR} (red and blue).

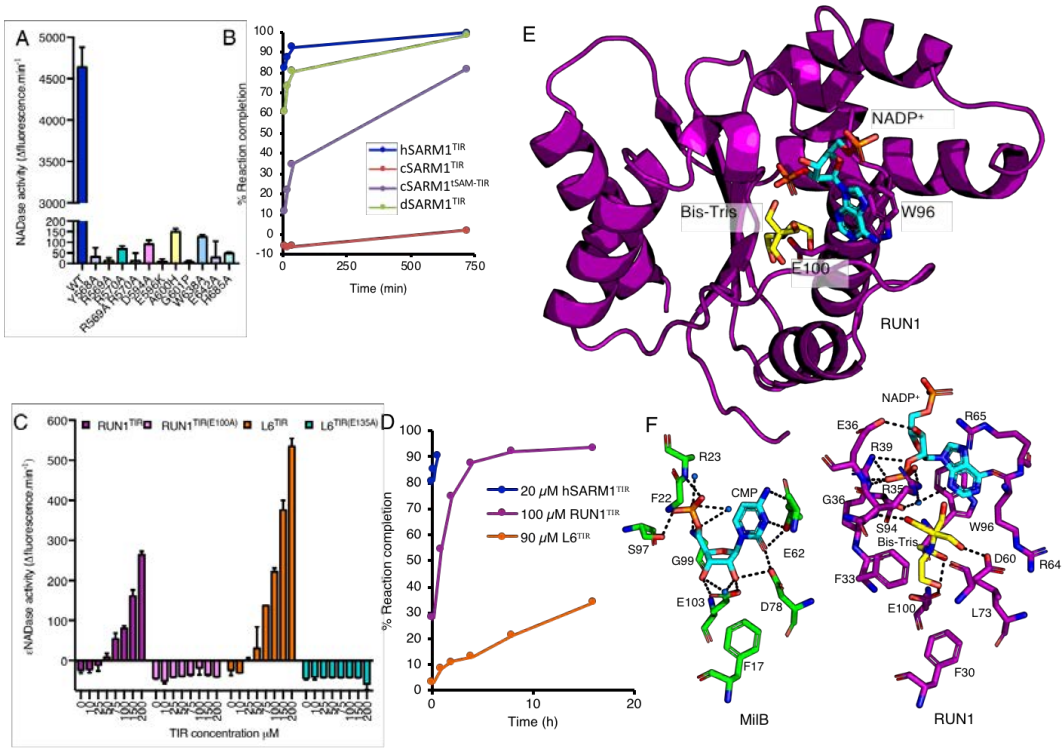

Fig. 3. **NADase activity of TIR domains.** (**A**) NADase activity of hSARM1^{TIR} and its mutants, measured by the fluorescence assay using εNAD. (**B**) NAD^+ cleavage-reaction time-courses of human, *Drosophila* and *C. elegans* SARM1^{TIR}, monitored by ^{1}H NMR (298 K), using a protein concentration of 20 µM and 1 mM NAD^+. (**C**) NADase activity of RUN1^{TIR}, RUN1$^{TIR(E100A)}$, L6^{TIR} and L6$^{TIR(E135A)}$, measured by the fluorescence assay using εNAD. (**D**) NAD^+ cleavage-reaction time-courses of RUN1^{TIR} and L6^{TIR}, monitored by ^{1}H NMR (20°C), using a protein concentration of 100 µM and 1 mM NAD^+. (**E**) Structure of RUN1^{TIR} in complex with $NADP^+$ and Bis-Tris (cartoon representation, ligands and selected residues in stick representation). (**F**) Comparison of the binding sites for CMP in MilB (PDB ID 4jem) and $NADP^+$/Bis-Tris in RUN1^{TIR} (stick representation).

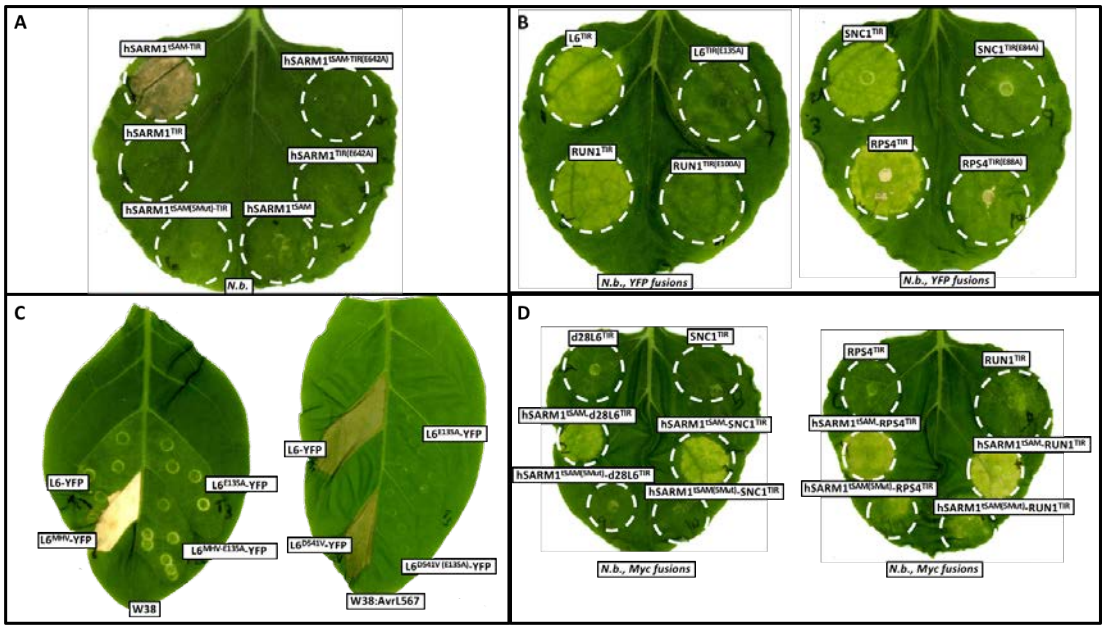

Fig. 4. **TIR domain functions in plants.** (**A**) Expression in *N. benthamiana* of hSARM1$^{tSAM\text{-}TIR}$, hSARM1^{TIR}, hSARM1$^{tSAM(5Mut)\text{-}TIR}$, hSARM1$^{tSAM\text{-}TIR(E642A)}$, hSARM1$^{TIR(E642A)}$ and hSARM1^{tSAM}. (**B**) Expression in *N. benthamiana* of catalytic glutamate mutants of L6^{TIR}, RUN1^{TIR}, SNC1^{TIR} and RPS4^{TIR}. (**C**) Expression of L6-YFP, L6^{MHV}-YFP, L6^{E135A}-YFP, L6$^{MHV\text{-}E135A}$-YFP in *N. tabacum* W38 (left) or transgenic W38 expressing AvrL567 (right). (**D**) Expression of fusion proteins of TIR domains from L6, SNC1, RPS4 and RUN1 to hSARM1^{tSAM} and hSARM1$^{tSAM(5Mut)}$.

Supplemental information

Materials and Methods

Fig. S1 – S31

Table S1 – S8

References (49 – 96)

Supplementary Materials for

Structural basis of NAD$^+$-cleavage activity by animal and plant TIR domains with functions in cell-death pathways

Shane Horsefield[1§], Hayden Burdett[1§], Xiaoxiao Zhang[2,3§], Mohammad K. Manik[1§], Yun Shi[4§], Jian Chen[2,3], Tiancong Qi[5], Jonathan Gilley[6,7], Jhih-Siang Lai[1], Maxwell X. Rank[1], Lachlan W. Casey[1], Weixi Gu[1], Daniel J. Ericsson[8], Gabriel Foley[1], Robert O. Hughes[9], Todd Bosanac[9], Mark von Itzstein[4], John P. Rathjen[3], Jeffrey D. Nanson[1], Mikael Boden[1], Ian B. Dry[10], Simon J. Williams[3], Brian J. Staskawicz[5], Michael P. Coleman[6,7],Thomas Ve[1,4*], Peter N. Dodds[2*] and Bostjan Kobe[1*]

Correspondence to: Bostjan Kobe (b.kobe@uq.edu.au), Thomas Ve (t.ve@griffith.edu.au), Peter Dodds (Peter.Dodds@csiro.au)

This PDF file includes:

Materials and methods

Recombinant protein cloning, expression and purification

The tandem SAM domains of human SARM1 (residues 409-561 with a L473F mutation inadvertently introduced by cloning), hSARM1^{tSAM}) was cloned using ligation-independent cloning (LIC) into the pMCSG7 vector (*49*). The resulting construct, which has an N-terminal 6xHis-tag, was produced in *E. coli* BL21 (DE3) cells using the autoinduction method (*50*), and purified to homogeneity using a combination of immobilised metal-ion affinity chromatography (IMAC) and size-exclusion chromatography (SEC): The cells were grown at 37°C, until an OD_{600} of 0.6-0.8 was reached. The temperature was then reduced to 20°C, and the cells were grown overnight for approximately 16 h. The cells were harvested by centrifugation at 6000 x *g* at 4°C for 10 minutes (Beckman Coulter J-26 XPI), the cell pellets were resuspended in 2-3 mL in the lysis buffer (50 mM HEPES pH 8.0, 500 mM NaCl) per g of cells and phenylmethanesulfonylfluoride (PMSF) was added to a final concentration of 1 mM. The resuspended cells were lysed using a digital sonicator (Branson, 6 x 10 seconds at 40% amplitude) and then clarified by centrifugation at 39, 191 x *g* for 30 minutes. The clarified lysate was supplemented with imidazole (final concentration of 30 mM) and then applied to a nickel HisTrap column (GE Healthcare) pre-equilibrated with 10 column volumes (CVs) of the wash buffer (50 mM HEPES pH 8.0, 500 mM NaCl, 30 mM imidazole) at a rate of 4 mL/min. The column was then washed with 10 CVs of the wash buffer and the bound protein eluted using the elution buffer (50 mM HEPES pH 7.5, 500 mM NaCl, 250 mM imidazole). The elution fractions were analysed by SDS-PAGE and the fractions containing hSARM1^{tSAM} were pooled and dialysed into the gel-filtration buffer (10 mM HEPES pH 7.5, 150 mM NaCl) for 4 hours. After dialysis, hSARM1^{tSAM} was further purified on a S200 HiLoad 26/600 column pre-equilibrated with the gel-filtration buffer. The peak fractions were analysed by SDS-PAGE, and the fractions containing hSARM1^{tSAM} were pooled and concentrated to final concentrations of approximately 10 mg/mL, flash-frozen as 25 μL aliquots in liquid nitrogen, and stored at -80°C.

A construct of codon-optimised hSARM1^{tSAM} containing three lysine-to-methionine mutations (L446, L505 and L523), but without the L479F mutation (hSARM1$^{tSAM(3M)}$), was cloned into pMCSG7 using LIC and transformed into B834 (DE3) competent *E. coli* cells. The cells were grown at 37°C in M9 minimal media supplemented with 0.2 mM selenomethionine (SeMet), until an OD_{600} of 0.6-0.8 was reached. The temperature was then reduced to 20°C and protein expression was induced by adding isopropyl β-D-1-thiogalactopyranoside (IPTG) to a final concentration of 0.5 mM. Growth was continued overnight at 20°C. Purification was carried out as described for hSARM1^{tSAM}, but 1 mM DTT (1,4-dithiothreitol) was included in all buffers.

Codon-optimised hSARM1^{tSAM} with five mutations (L442R, I461D, L514D, L531D, V533D), designated hSARM1$^{tSAM(5Mut)}$, was cloned, expressed and purified as described for hSARM1^{tSAM}.

The complete coding region of wild-type mouse SARM1 (724 amino-acid variant; mSARM1^{wt}) or mSARM1^{5Mut} was PCR-amplified using Herculase II fusion polymerase (Agilent Technologies) and cloned between the EcoRI and XhoI restriction sites in the pCMV-Tag2B mammalian expression vector (Agilent Technologies), in frame with an N-terminal Flag tag. Constructs without any PCR-generated errors were chosen after sequencing

The TIR domain of human SARM1 (residues 560-700, hSARM1^{TIR}) and its mutants were cloned and expressed as described for the hSARM1^{tSAM} constructs. hSARM1^{TIR} was purified as described for hSARM1^{tSAM}; however, after overnight dialysis with the TEV (tobacco etch virus) protease, hSARM1^{TIR} was further purified on a S75 HiLoad 26/600 column, pre-equilibrated with the gel-filtration buffer. The peak fractions were analysed by SDS-PAGE, and the fractions containing hSARM1^{TIR} were pooled and concentrated to a final concentrations of approximately 6 mg/mL, flash-frozen as 25 μL aliquots in liquid nitrogen, and stored at -80°C.

For hSARM1^{TIR} mutants, cells were resuspended after expression in a lysis buffer containing 2x PBS pH 7.4, 300 mM NaCl, 30 mM imidazole and 1 mM PMSF. The cells were lysed by sonication, and the lysate was clarified by centrifugation at 39,191 x *g* for 40 min at 4°C. The clarified lysate was applied to a HisTrap 5 mL FF column pre-equilibrated with the lysis buffer, then washed with 100 mL of the same lysis buffer to remove *E. coli* proteins. hSARM1^{TIR} mutants were eluted using the elution buffer (containing 100 mM HEPES pH 8.0, 500 mM NaCl, 500 mM imidazole), and the fractions containing hSARM1^{TIR} mutants were pooled. The eluted protein fractions were dialysed against 20 mM HEPES pH 8.0, 150 mM NaCl using 10,000 MWCO SnakeSkin™ dialysis tubing, before the 6xHis-tag was removed by incubation with 6xHis-tagged TEV protease overnight at 4°C. Cleaved hSARM1^{TIR} mutants were reapplied to the HisTrap column to remove the TEV protease and contaminants. The proteins were then applied to a Superdex S75 26/600 pre-equilibrated with 20 mM HEPES pH 8.0 and 150 mM NaCl. The peak fractions were pooled and concentrated to 20 mg/mL using a 10,000 MWCO centrifugal concentrator. Proteins were flash-frozen in liquid nitrogen and kept at -80°C until required.

cSARM1$^{tSAM-TIR}$ (residues 581-902) and cSARM1^{TIR} (residues 760-902) were amplified by PCR from codon-optimized DNA of *C. elegans* ortholog of SARM1, TIR-1. The fragments were then sub-cloned into the pET 6xHis-tag MBP TEV LIC (1M) vector and the pMCSG7 vector, respectively. The cSARM1$^{tSAM-TIR(E842A)}$ mutant was generated using PCR- mutagenesis and then sub-cloned into the pET 6xHis-tag MBP TEV LIC (1M) vector. Protein expression and purification were carried out using the method described for the hSARM1^{TIR} mutants.

L6^{TIR}, RPV1^{TIR}, RPP1^{TIR}, SNC1^{TIR} and RPS4^{TIR} were purified as described in (*51-54*). The cDNA of RUN1^{TIR} (residues 23-198) was cloned in the expression vector pMCSG7 and expressed in *E. coli* BL21 (DE3) cells, using the autoinduction method. Overnight cultures were used to seed 1 L autoinduction media cultures containing 100 μg.mL^{-1} ampicillin in 2.5 L baffled flasks. Cultures were grown at 37°C to OD_{600} 0.6-0.8, before the temperature was lowered to 15°C. Cells were grown for an additional 12-18 h before being harvested by centrifugation. Cells containing RUN1^{TIR} were resuspended in a lysis buffer containing 50 mM HEPES pH 8.0, 500 mM NaCl, 30 mM imidazole, 1 mM DTT and 1 mM PMSF. Cells were lysed by sonication, and the lysate was clarified by centrifugation at 39,191 x *g* for 45 min at 4°C. Clarified lysate was applied to a 5 mL HisTrap FF column pre-equilibrated with 50 mM HEPES pH 8.0, 500 mM NaCl, 30 mM imidazole. The column was washed with the lysis buffer to remove *E. coli* proteins. RUN1^{TIR} was eluted using a block elution of lysis buffer containing 250 mM imidazole and fractions containing RUN1^{TIR} were pooled. To remove the 6xHis-tag, imidazole was diluted by dialysis, using 10,000 MWCO SnakeSkin™ dialysis tubing in a buffer containing 10 mM HEPES pH 7.5, 150 mM NaCl, 0.5 mM EDTA and 1 mM DTT. The 6xHis-tag of RUN1^{TIR} was then removed by incubation with 6xHis-tagged TEV protease overnight at 4°C. Cleaved RUN1^{TIR} was reapplied to the HisTrap column to

remove the TEV protease and contaminants. RUN1^{TIR} was applied to a Superdex S75 26/600 pre-equilibrated with 10 mM HEPES pH 7.5, 150 mM NaCl and 1 mM DTT. Peak fractions were pooled and concentrated to 10 mg.mL^{-1} using a 10,000 MWCO centrifugal concentrator. Protein was flash-frozen in liquid nitrogen, and kept at -80°C until required. ROQ1^{TIR} (residues 10-181) was cloned in pLIC171, and expressed and purified using the same protocol as RUN1^{TIR}, with the exception that kanamycin was used for selection instead of ampicillin.

Crystallization and crystal structure determination

The structure of hSARM1^{tSAM} was solved by the single-wavelength anomalous dispersion (SAD) phasing method using crystals of selenomethionine (SeMet)-labelled protein with three leusine-to-methionine mutations (L446M, L505M and L523M; designated hSARM1$^{tSAM(3M)}$). These residues were selected because they are predicted to be in ordered regions of the protein, because they correspond to leucine, isoleucine or methionine in SARM1 orthologues, and because leucine-to-methionine substitutions are usually not disruptive to protein structure (*55*).

Native hSARM1^{tSAM} crystals were produced using the hanging drop method with drops containing 1 µL of protein (5 mg/mL) and 1 µL of well solution (10.7% w/v PEG 4000, 21.4% v/v glycerol, 30 mM $MgCl_2$ and 0.1 M bicine/Trizma base pH 8.0) and appeared within 1-2 days. Crystals of SeMet-labelled hSARM1$^{tSAM(3M)}$ were produced using the same technique, with drops containing 1 µL of protein (5 mg/mL) and 1 µL of well solution (17% PEG 8000, 20% ethylene glycol, 0.2 M sodium formate, 0.2 M ammonium acetate, 0.2 M trisodium citrate, 0.2 M sodium potassium L-tartrate, 10 mM DTT and 0.1 M Tris pH 7.9). These crystals also appeared within 1-2 days. Crystals of native hSARM1^{tSAM} were flash-cooled in liquid nitrogen without using additional cryo-protectant. Prior to flash-cooling, the SeMet-labelled hSARM1$^{tSAM(3M)}$ crystals were dehydrated by the addition of 1-2 µL of 50% w/v PEG8000 to the drop containing crystals with 2-5 min equilibration between addition of PEG8000, until an approximate final concentration of 30% was reached.

X-ray diffraction data for the native hSARM1^{tSAM} crystals were collected from a single crystal at the Australian Synchrotron MX2 beamline, using a wavelength of 0.9537 Å. Data collection was performed using Blu-Ice software (*56*), indexed and integrated using MOSFLM (*57*) and scaled with AIMLESS (*58*) within the CCP4 suite (*59*). With the native data-set, molecular replacement was attempted using several published SAM domain structures as templates, but a solution could not be obtained.

X-ray diffraction data for the SeMet-labeled crystals of hSARM1$^{tSAM(3M)}$ were collected from a single crystal at the Australian Synchrotron MX2 beamline, using a wavelength of 0.9793 Å. The structure was solved using the single-wavelength anomalous diffraction (SAD) method through the *Autosol* pipeline within the *PHENIX* suite (*60*) and an initial model was built automatically through the *Autobuild* pipeline within the *PHENIX* suite. The native hSARM1^{tSAM} structure was subsequently solved by molecular replacement using PHASER (*61*), with the hSARM1$^{tSAM(3M)}$ model as the template. Models of both hSARM1^{tSAM} and hSARM1$^{tSAM(3M)}$ were refined using Phenix.refine and iterative model building between refinements was carried out in Coot (*62*). Structure validation was performed using MolProbity (*63*). Coordinates and structure factors of hSARM1^{tSAM} and hSARM1$^{tSAM(3M)}$ have been deposited in the PDB with IDs 6o0s and 6o0t, respectively.

The hSARM1^{TIR} crystals were produced using the hanging drop vapour diffusion method, as described for the hSARM1^{tSAM} crystals. The optimal crystals were obtained using 1 µL protein and 1 µL well solution (0.1 M Bis-Tris propane pH 6.5, 0.2 M potassium thiocyanate, 11% PEG3350). The crystals were cryoprotected in 25-30% glycerol before flash-cooling in liquid nitrogen. X-ray diffraction data were collected from a single crystal at the Australian Synchrotron MX2 beamline, using a wavelength of 0.9537 Å. Data collection was performed using Blu-Ice software (*56*), indexed and integrated using XDS (*64*) and scaled with AIMLESS (*58*) within the CCP4 suite (*59*). Molecular replacement using individual published TIR domains was unsuccessful; therefore, CHAINSAW (*65*) was used. Poly-alanine backbones of several TIR domain structures (PDB IDs 1t3g, 2j67, 3h16, 3ub2, 4eo7, 4lqc, 4om7 and 4w8h) were merged using ENSEMBLER (*60*) and used as a search model for molecular replacement. The model was refined using Phenix (*60*), and structure validation was performed using MolProbity (*63*). Coordinates and structure factors have been deposited in the PDB with ID 6o0r.

The structure of hSARM1^{TIR} bound to D-ribose was obtained by soaking a hSARM1^{TIR} crystal in the crystallisation solution (0.1 M Bis Tris propane pH 6.5, 0.2 M potassium thiocyanate, 11% PEG3350) containing 500 mM D-ribose for 48 h. The crystal was cryoprotected in Paratone-N and flash-cooled at 100 K. X-ray diffraction data were collected from a single crystal on the MX2 beamline at the Australian Synchrotron, using a wavelength of 0.9537 Å. The data-set was processed using XDS (*64*) and scaled using AIMLESS (*58*) in the CCP4 suite (*59*). The structure was solved by molecular replacement using Phaser (*61*) and glycerol-bound hSARM1^{TIR} as the template. The model was refined using Phenix (*60*), and structure validation was performed using MolProbity (*63*). Electron density was observed in the active site regions of both chains in the asymmetric unit. In both chains, D-ribose is best accommodated in a β-anomer configuration and only this one has been included in the refined structure. Although the electron density is well defined for the C2-C3 atoms and the C2 and C3 hydroxyl groups, it is more diffuse around the C4 and C5 atoms and the C5 hydroxyl, and less defined around the C1 and O4 atoms and C1 hydroxyl. As the binding of D-ribose to hSARM1^{TIR} is inherently weak, it is likely we only have partial occupancy in the binding site and the presence of solvent may obscure the density. It is also possible that additional conformations of D-ribose may be present in the crystal structure. Near the ribose C5 atom and wedged between the R569 NH1 group and the R570 main-chain amide group, we observed a spherical electron density peak too strong to be explained as a water; we assigned it as a chloride (Cl^-) ion, as it was the only anion present in appreciable amounts (150 mM) in the crystallisation solution. Based on docking analysis, this ion likely occupies the position of the phosphate group attached to the C5 atom of the ribose in the NMN moiety of NAD^+. Coordinates and structure factors have been deposited in the PDB with ID 6o0q.

The hSARM1^{TIR} mutant crystals were produced using the hanging drop vapour diffusion method, as described for the hSARM1^{tSAM} crystals. The hSARM1$^{TIR(H685A)}$ crystals (0.1 M HEPES pH 7.5, 0.2 M $MgCl_2$, 25% PEG3350) were cryoprotected using 40% glycerol, whereas the hSARM1$^{TIR(G601P)}$ crystals ("MES-bound": 0.1 MES pH 6.0, 1 M LiCl, 20% PEG6000; "ligand-free": 0.1 MES pH 6.0, 0.2 M $MgCl_2$, 20% PEG3350) were cryoproteced using Paratone-N before flash-cooling in liquid nitrogen. X-ray diffraction data for the hSARM1$^{TIR(H685A)}$ and the hSARM1$^{TIR(G601P)}$ crystals were collected from a single crystal at the Australian Synchrotron MX2 beamline, using a wavelength of 0.954 Å. Data were indexed and integrated using XDS (*64*) and scaled

using AIMLESS (*58*). The hSARM1$^{TIR(H685A)}$ and hSARM1$^{TIR(G601P)}$ structures were determined by molecular replacement using Phaser (*61*), with the structure of glycerol-bound hSARM1^{TIR} as the template. Iterations of Phenix (*60*) and Coot (*62*) were used to refine the models. Note that the "ligand-free" structure contains 4 protein molecules in the asymmetric unit, of which 3 are ligand-free, while the fourth is bound to MES; for clarity, we refer to the structure as "ligand-free" and only refer to the ligand-free protein molecules, unless state otherwise. Weak electron density for an alternative conformation of the BB loop region (592-596) was present in the chain C of the "ligand-free" structure. As the density is poor for this conformation, we have only included one conformation in the final model. Coordinates and structure factors have been deposited in the PDB with IDs 6o0u (hSARM1$^{TIR(H685A)}$), 6o1b ("MES-bound" hSARM1$^{TIR(G601P)}$), and 6o0v ("ligand-free" hSARM1$^{TIR(G601P)}$), respectively.

RUN1^{TIR}:NADP^{+} crystals were produced using the hanging drop method, with drops containing 1 µL of protein (10 mg/mL), 1 µL of well solution (0.2 M NaCl, 0.1 M Bis-Tris pH 6.5, 25% w/v PEG 3350) and 1 µL of 10 mM NADP^{+} and appeared within 2-4 days. Crystals were added to the cryoprotecting solution (0.2 M NaCl, 0.1 M Bis-Tris pH 6.5, 25% w/v PEG3350, 10% v/v glycerol, 10% v/v ethylene glycol) and soaked for 2-5 min, before being flash-cooled in liquid nitrogen. X-ray diffraction data for the RUN1^{TIR}:NADP^{+} crystal were collected from a single crystal at the Australian Synchrotron MX2 beamline, using a wavelength of 0.95374 Å. Data collection was performed using Blu-Ice software (*56*), indexed and integrated using XDS (*64*) and scaled using AIMLESS (*58*). The RUN1^{TIR}:NADP^{+} structure was determined by molecular replacement using Phaser (*61*), with the structure of RPV1^{TIR} (PDB ID 5ku7) (*52*) as the template. Iterations of Phenix (*60*) and Coot (*62*) were used to refine the models. The RUN1^{TIR} structure very closely resembles RPV1^{TIR} (Cα RMSD of ~0.8 Å over 160 residues), consistent with 86% sequence identity (*66*). Coordinates and structure factors for RUN1^{TIR}:NADP^{+} structure have been deposited in the PDB with IDs 6o0w.

Structural analyses

Structural analyses were carried out using DALI (*22*), Consurf (*48*), PISA (*67*) and PyMOL (http://www.pymol.org). Figures were generated using PyMOL.

Size-exclusion chromatography (SEC)-coupled multi-angle light scattering (MALS)

MALS was performed using a DAWN HELEOS II 10-angle light-scattering detector coupled with an Optilab rEX refractive index detector (Wyatt Technology), combined with Superdex 200 5/150 Increase size exclusion column (GE Healthcare) connected to a Prominence HPLC (Shimadzu). Purified proteins were separated at 0.25 mL/min in 10 mM HEPES pH 7.5 and 150 mM NaCl for hSARM1^{TIR}, and 10 mM HEPES pH 7.5, 150 mM NaCl and 1 mM DTT for RUN1^{TIR}. Molecular-mass calculations were performed using the Astra6.1 software (Wyatt Technology). Input of the refractive increment (dn/dc values) was set at 0.186 in the molecular-mass calculations, based on the premise that dn/dc is constant for unmodified proteins (*68*). The molecular mass was calculated across the protein elution peak.

Size-exclusion chromatography (SEC)-coupled small-angle X-ray scattering (SAXS)

SEC-SAXS was performed at the SAXS/WAXS beamline of the Australian Synchrotron on a Pilatus 1M detector, using an in-line WTC-030S5 SEC column and a 2 mL WTC-030S5G pre-column (Wyatt Technology), together with a Prominence modular HPLC system (Shimadzu). All experiments were conducted at 16°C using 10 mM HEPES (pH 7.5), 150 mM NaCl buffer with 1 mM DTT. Eluate from the column was directed through a quartz capillary mounted in the beam, with a path-length of 1 mm. For all samples, the injected volume was 50 µL at 7 mg/mL protein concentration, as determined by UV absorbance at 280 nm.

Data-sets were collected in 2 s exposures at 0.05 s intervals with a flow rate of 0.5 mL/min. A Wyatt WTC-030S5G pre-column was used upstream of the WTC-030S5. The sample-to-detector distance was 1.4 m, and a wavelength of 1.12713 Å yielded a range of momentum transfer ($0.009 < q < 0.614$ Å-1, where $q = 4\pi.\sin(\theta)/\lambda$).

Data reduction, normalisation and subtraction were performed using scatterBrain (http://www.synchrotron.org.au/index.php/aussyncbeamlines/saxswaxs/software-saxswaxs). Buffer blanks were obtained from 100 frames immediately preceding each peak, and were subtracted from each individual frame to generate a series of subtracted profiles across the elution peak, from which $I(0)$ and Rg were calculated using AUTORG as implemented in version 2.6 of the ATSAS program suite (*69*). Molecular masses were calculated using a local implementation of the volume of correlation (Vc) method developed by Rambo and Tainer (*70*), for points up to $q = 0.3$.

Data-sets for subsequent analysis were obtained from contiguous regions of the elution for which the calculated parameters were stable. Un-subtracted frames from these regions were summed and normalised, and then subtracted from the previously averaged buffer blanks. Parameters were calculated from these averaged data-sets using AUTORG, AUTOGNOM and DATMW via Primus in version 2.8.4 of the ATSAS package (*71, 72*).

Axon degeneration assays

Dissociated *Sarm1*$^{-/-}$ SCG neuron cultures were prepared, injected with expression constructs and immunostained essentially as described previously for wild-type SCG neurons (*73*). A mouse monoclonal SARM1 antibody (*74*) was used at 1:500 for immunostaining. The type and concentration of constructs injected are listed in the legend to Fig. 1. mSARM1 variant constructs were also transfected into HEK cells for immunoblot analysis of expressed proteins. Transfection was essentially performed as described previously (*73*) with the types of constructs transfected being listed in the legend to Fig. 1. Flag-WLD^{S} was co-transfected as a control for transfection efficiency. Mouse monoclonal SARM1 (1:5000) and M2 anti-Flag (Sigma, 1:2000) antibodies were used for immunoblotting.

NADase assays

Several assays were used to measure NADase activity. In the fluorescence assay, a fluorescent analog of NAD^{+}, 1,N^{6}-ethenoNAD (εNAD), was used as the substrate (*24*). The assay relies on an increase in fluorescence from the 1,N^{6}-ethenoadenine diphosphate ribose after cleavage of the quenching nicotinamide group. εNAD stocks were made using the RUN1^{TIR} gel-filtration buffer (10 mM HEPES pH 7.5, 150 mM NaCl). Varying concentrations of the TIR domain and εNAD were used depending on

the experiment, and 10 μL of 50% suspension of Ni-NTA beads was used where relevant. Beads were washed in the gel-filtration buffer before use and were added to bring TIR domains to close proximity in the assay. For molecular crowding experiments, PEG stocks were prepared in the gel-filtration buffer, and readjusted to pH 7.5, if required. Fluorescence intensity was measured in a CLARIOstar® microplate reader, using an excitation of wavelength of 310-330 nm and emission wavelength of 390-410 nm, with readings every 1-3 min over 1-2 h. The change in fluorescence over time was determined by calculation of slopes of the linear component of the curves. Data analysis was performed using Prism graphpad.

In the NMR assay, NMR samples were prepared in HEPES buffered saline (10 mM HEPES, 150 mM NaCl, pH 7.5) with a minimum of 10% D_2O v/v. Each sample was prepared with a total volume of 200 μL, which was subsequently transferred to a 3 mm Bruker NMR tube rated for 600 MHz data acquisition. All ^{1}H NMR spectra were acquired with a Bruker Avance 600 MHz NMR spectrometer equipped with $^{1}H/^{13}C/^{15}N$ triple resonance cryoprobe at 298 K. To suppress resonance from H_2O, watergate 3-9-19 suppression pulse (PULPROG:p3919gp) was implemented to acquire spectra with an acquisition delay of 2 s and 32 scans per sample. All spectra were processed by Bruker's TopSpin™ software, and selected resonances (NAD^+ Hd, $NADP^+$ Hd, NMN Ha, NAAD Hd and FAD) were integrated by Mnova 11 (Mestrelab Research). The assignment spectra are shown in Fig. S12.

The cycling assay was used with *E. coli* lysates. The lysates were produced as described in (*38*), with changes noted below. Briefly, pMCSG7 vectors containing TIR constructs were transformed into Shuffle T7 Express *E. coli* cells by the heat-shock method (*75*). Cells were grown overnight in 10 mL of SOB media (2 % (w/v) tryptone, 0.5 % (w/v) yeast extract, 10 mM NaCl, 2.5 mM KCl, 10 mM $MgCl_2$ and 10 mM $MgSO_4$) containing appropriate antibiotics and 0.4 % (w/v) glucose, to prevent leaky expression of TIR domains. Overnight cultures were split and used to inoculate two 5 mL cultures at a starting OD_{600} 0.6. To one culture, 0.5 mM IPTG was added, and both were grown for 2-6 hours at 30°C. Cells were harvested by centrifugation at 3,750 x *g* for 10 min at ambient temperature. NAD^+ was extracted using a method modified from (*76*). Briefly, cellular metabolism was quenched by resuspension of cells in 300 μL of quenching solution (60 % (v/v) methanol, 70 mM HEPES pH 5.5), followed by an incubation at -40°C for 15 min. Cells were pelleted by centrifugation at 12,390 x *g* for 5 min at 4°C, and the resultant pellet was resuspended in 200 μL of 100% methanol. Cells were lysed by two freeze-thaw cycles, from liquid nitrogen to 4°C. The resultant supernatant was then used in the NAD^+ cycling assay (in a total volume 700 μL). The cycling assay was adapted from (*31*), with changes noted below. Briefly, 20 μL of diluted *E. coli* lysate samples and NAD^+ standards were added to 100 μL of assay mix (200 mM HEPES pH 8.0, 8 mM EDTA, 3.32 mM PES (polyether sulfone), 0.84 mM MTT (3-(4,5-dimethylthiazol-2-yl)-2,5-diphenyltetrazolium bromide) and 1 M ethanol). The final volume reaction volume was brought to 180 μL by addition of 0.1 M NaCl. Reactions were incubated at 37°C for 5 min, before addition of 20 μL of 100 $U.mL^{-1}$ of alcohol dehydrogenase, using the injection system on a CLARIOstar® microplate reader. Absorbance at 570 nm was measured over 40 min, with a reading every minute. NAD^+ concentration was determined by calculating the slopes of the linear component of the curves for both *E. coli* lysate samples and NAD^+ standards. All measurements were performed at least in duplicate.

The mass spectrometry-based enzymatic assay was performed in a 384-well polypropylene plate in Dulbecco's PBS buffer in a final assay volume of 20 μL. NRK1-

HEK293T cells were seeded onto 150 cm^2 plates at 20 x 106 cells per plate. The next day, the cells were transfected with 15 µg FCIV-SST ($SARM1^{SAM\text{-}TIR}$ (residues 558-724) expression plasmid) using X-TREMEGENE™ 9 DNA Transfection Reagent (Roche). The cultures were supplemented with 1 mM NR at time of transfection, to minimize toxicity from SAM-TIR overexpression. Forty-eight hours after transfection, cells were harvested, pelleted by centrifugation at 1,000 rpm (Sorvall ST 16R centrifuge, Thermo Fisher), and washed once with cold PBS (0.01 M phosphate buffered saline NaCl 0.138 M; KCl 0.0027 M; pH 7.4). The cells were resuspended in PBS with protease inhibitors (cOmplete™ protease inhibitor cocktail, Roche) and cell lysates were prepared by sonication (Branson Sonifer 450, output = 3, 20 episodes of stroke). The lysates were centrifuged (12,000 × *g* for 10 min at 4°C) to remove cell debris and the supernatants (containing the $SARM1^{SAM\text{-}TIR}$ protein) were stored at -80°C for later use in the *in vitro* mass spectrometry-based NADase assay. Protein concentration was determined by the bicinchoninic (BCA) method and used to normalize lysate concentrations. The enzymatic assay was performed in a 384-well polypropylene plate in Dulbecco's PBS buffer in a final assay volume of 20 µL. $SARM1^{SAM\text{-}TIR}$ lysate with a final concentration of 5 µg/mL was pre-incubated with the respective compound at 1% DMSO final assay concentration over 2 h at room temperature. The reaction was initiated by addition of 5 µM final assay concentration of NAD^+ as substrate. After a 2 h room temperature incubation, the reaction was terminated with 40 µL of stop solution of 7.5% trichloroactetic acid in acetonitrile. The NAD^+ and ADPR concentrations were analyzed by a RapidFire High Throughput Mass Spectrometry System (Agilent Technologies, Santa Clara, CA) using an API4000 triple quadrupole mass spectrometer (AB Sciex Framingham, MA).

Plant experiments

For transient expression *in planta*, hSARM1 or plant TIR domain-derived constructs were cloned in the Gateway binary vectors pAM-PAT-35S-GWY-Myc or -YFPv, as previously described (*77*). To generate fusions with plant TIR proteins, $hSARM1^{tSAM}$ or $hSARM1^{tSAM(5Mut)}$ were cloned into the XhoI and HindIII restriction sites of the Myc-fusion binary vector. Single amino acid mutations were introduced by Dpn1-mediated site-directed mutagenesis (Stratagene), following the manufacturer's instructions.

For *in planta* cell-death assays, *Agrobacterium tumefaciens* cells harbouring the desired binary vector constructs were grown overnight at 28 °C in LB media with appropriate antibiotic selections. The cells were harvested by centrifugation and resuspended in the infiltration mix (10 mM MES pH 5.4, 10 mM $MgCl_2$ and 200 µM acetosyringone) to an optical density of 0.5, followed by incubation at room temperature for 2 h. Resuspended cells were infiltrated with a 1 mL needle-less syringe into leaves of 3-week-old wild-type or *eds1-1* knock-out (*34*) *N. benthamiana* plants, and wild-type *N. tabacum* plants (W38) or transgenic *N. tabacum* plants expressing the flax rust effector AvrL567 (*78*).

For immunoblot analysis, proteins were extracted from the leaf tissue in the Laemmli buffer, separated by SDS-PAGE and transferred to nitrocellulose membranes (Pall). Membranes were blocked in 5% skim milk and probed with anti-Myc mouse antibodies (Roche) or anti-GFP mouse monoclonal antibodies (Roche), followed by goat anti-mouse HRP conjugate (BioRad). Protein labelling was detected with the SuperSignal West Femto chemiluminescence kit (Pierce). Membranes were stained with Red Ponceau to visualize protein loading.

Molecular docking

Three-dimensional structures of NAD^+ and NMN were downloaded from https://pubchem.ncbi.nlm.nih.gov/ (PubChem CIDs 5892 and 14180, respectively). They were subsequently processed using the LigPrep panel within Maestro 11 (Schrödinger, LLC) with default parameters, and the resulting structures were used as ligands for molecular docking. Crystal structures of $hSARM1^{TIR}$ and $RUN1^{TIR}$ were processed by the Protein Preparation Wizard within Maestro 11 (Schrödinger, LLC), using default settings. All water molecules in the crystal structures were removed, except for one that is believed to play a critical role in forming hydrogen bonding networks between the bound ligand and protein residues (for $RUN1^{TIR}$, this water molecule accepts a hydrogen bond from Asp57 N and donates a hydrogen bond to Leu28 O; for $hSARM1^{TIR}$, this water molecule accepts a hydrogen bond from Asp517 N and donates a hydrogen bond to Ile566 O). The processed protein structures were used as receptors in molecular docking. Induced-fit docking (*79*) that utilizes both Glide (*80, 81*) and Prime refinement (*82*) functions was performed for both $hSARM1^{TIR}$ and $RUN1^{TIR}$. The grid box was centered on the glycerol ligand within the active site of $hSARM1^{TIR}$ (chain A) and the Bis-Tris ligand within the active site of $RUN1^{TIR}$ (chain A), with a size of 30 × 30 × 30 Å. For $RUN1^{TIR}$, hydrogen-bond constraints were applied on Glu97 OE1 and OE2, and the H of the bound water molecule, so that only conformations satisfying all 3 hydrogen-bonding requirements (2 donors and 1 acceptor from the ligand) would be considered. Other settings were kept as default. The top-ranking docked poses that have all three aforementioned hydrogen bonds present were selected.

Molecular dynamics simulations

MD simulations were performed by GROMACS 5 (*83*) with the monomeric and oligomeric forms of $hSARM1^{TIR}$. Initial coordinates were taken from or derived from crystal structures after removal of solvent residues and processing by the MolProbity server (*63*). AMBER99SB force field (*84*) was used to parameterize all residues. Each structure was placed in a dodecahedral box with a minimal distance of 1.4 nm between the solute and box edge, followed by solvation with TIP3P water molecules. Salt ions were then added to a concentration of 0.15 M to balance ionic charge in the system. Energy minimizations were carried out with steepest descent integrator and conjugate gradient algorithm sequentially, to achieve a maximum force of less than 500 kJ mol^{-1} nm^{-1} on any atom. The Verlet cutoff scheme (*85*) was used to evaluate short-range, non-bonded interactions, with both van-der-Waals and electrostatic interactions truncated at 0.8 nm. Long-range electrostatic interactions were treated by the particle mesh Ewald (PME) method (*86, 87*). The temperature was maintained at 298 K using a velocity-rescaling thermostat with a coupling constant of 0.1 ps, while the pressure was maintained at 1.0 atm using a Berendsen barostat (*88*) with a coupling constant of 1 ps. Simulations were performed with a time step of 2 fs, and all bonds involving hydrogen atoms were constrained by a parallel linear constraint solver (P-LINCS) (*89*). Each system was equilibrated under a constant volume (NVT) ensemble for 100 ps and a constant pressure (NPT) ensemble for 100 ps. A harmonic position restraint with a force constant of 1000 kJ mol^{-1} nm^{-2} was applied to all the heavy atoms of non-solvent molecules. After equilibration, production MD simulations were conducted for 50 ns for each system without any constraints. Three replicate MD runs were

performed for each system by varying the random seed for initial velocity generation. Analyses of MD trajectories were performed by the in-built programs of GROMACS 5 on the final 20 ns of each 50-ns run.

Supplementary Figure legends

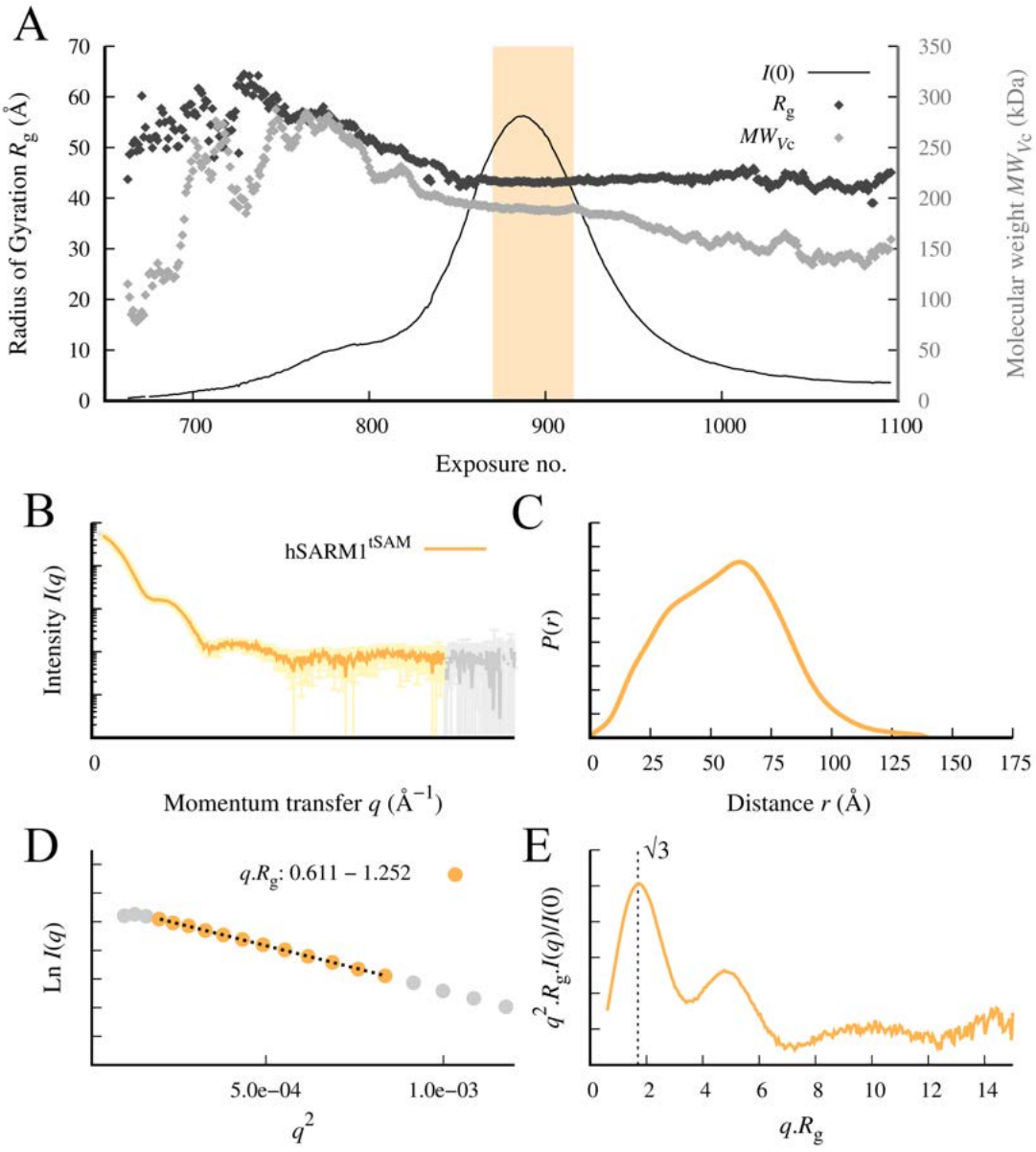

Fig. S1. SAXS characterisation of hSARM1^{tSAM}. (**A**) SEC-SAXS profile of hSARM1^{tSAM}, with Guinier R_g and MM_{Vc} plotted across the elution. The region used in subsequent analysis is highlighted in yellow. (**B**) Averaged and subtracted SAXS curve shown with colored lines, with error bars at 1 σ in lighter color. *y*-axis units are arbitrary. Data is plotted in grey outside the region used for analysis. The properties calculated from this averaged data-set are as follows: $I(0)_{Guin}$ = 5 .769 x 10^{-2} cm^{-1}; $I(0)_{P(r)}$ = 5.753 10^{-2} cm^{-1}; $R_{g\ Guin}$ = 43.4 Å; $R_{g\ P(r)}$ = 43.1 Å; d_{max} = 136 Å; MM_{Vc} = 190.22 kDa; MM_{Qp} = 217.03 kDa; $MM_{Bayesian}$ = 185.78 kDa. (**C**) Distance distributions calculated using GNOM. (**D**) Guinier region plotted as colored circles for the region used in Guinier analysis, and as grey circles outside this region. Linear regression fits against this region are shown as dotted lines. (**E**) Normalised Kratky analysis; the transformed data-set is plotted as colored lines. The first maximum is expected at $q.R_g$ = √3 for stable, globular particles.

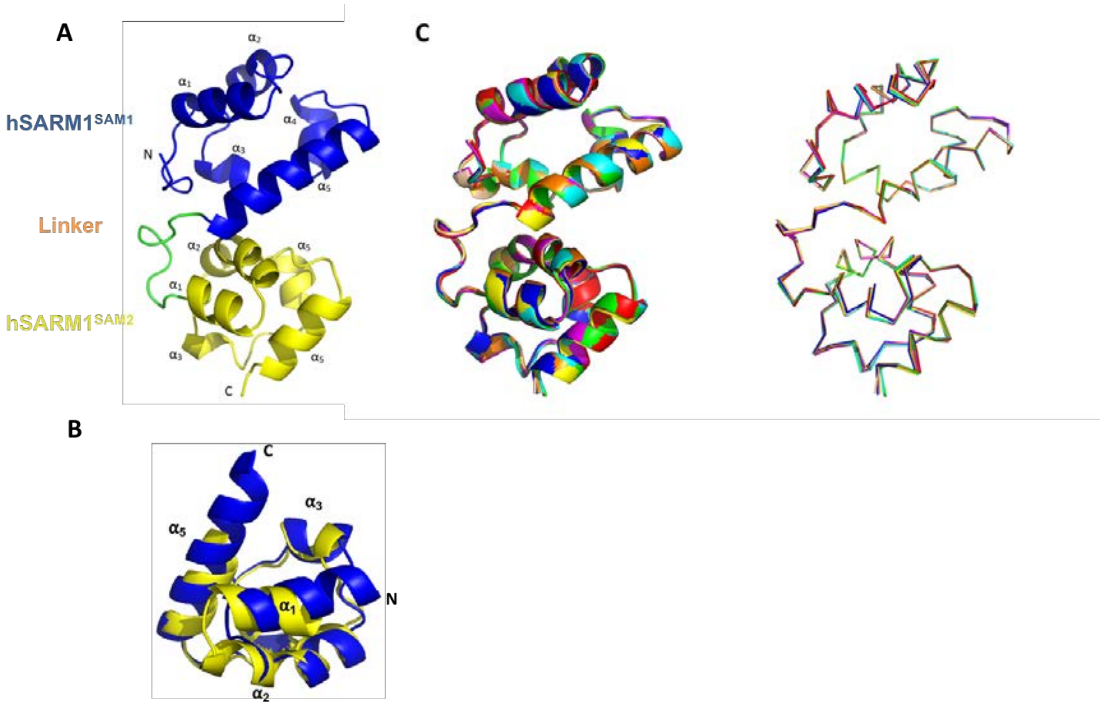

Fig. S2. Structure of a hSARM1^{tSAM}. (**A**) Ribbon diagram showing the overall structure of a hSARM1^{tSAM} monomer. The two SAM domains (hSARM1^{SAM1}: blue, hSARM1^{SAM2}: yellow) in hSARM1^{tSAM} are connected by a linker region (green). (**B**) Superposition of the hSARM1^{SAM1} (blue) and hSARM1^{SAM2} (yellow) domains of hSARM1^{tSAM}. The two SAM domains have a root-mean-square-distance (RMSD) of 1.25 Å for 54 structurally equivalent Cα atoms, with the main difference being a longer α5 helix in hSARM1^{SAM1} compared to hSARM1^{SAM2}. **(C)** Structural comparison of the eight individual hSARM1^{tSAM} chains in the crystal structure. Chains B-H are superimposed onto chain A and shown in cartoon (left) and ribbon (right) representation; RMSDs are <0.34 Å for Cα atoms.

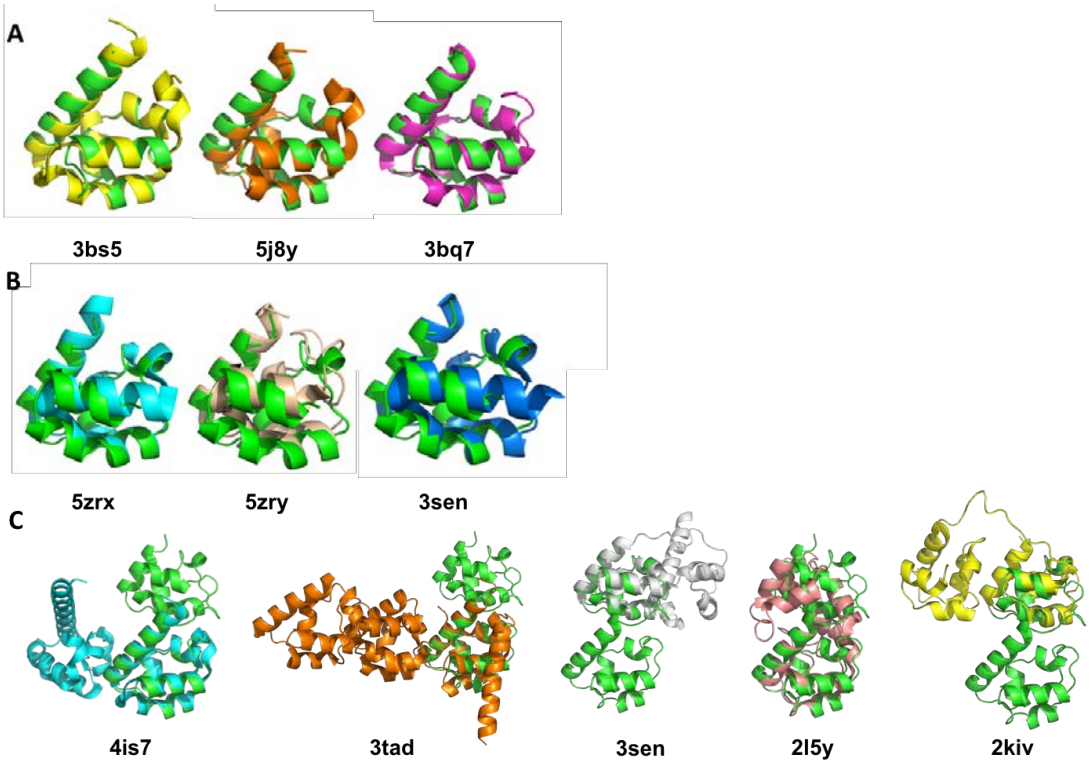

Fig. S3. SARM1 SAM domains display high structural similarity to previously reported SAM domain structures. Superposition of hSARM1^{SAM1} and hSARM1^{SAM2} with the top hits from a DALI search (Table S2). (**A**) Superposition of hSARM1^{SAM1} (green) with the SAM domain from CNK2 (connector enhancer of kinase suppressor of Ras 2) (yellow; PDB ID 3bs5), polycomb protein Sfmb (orange; PDB ID 5j8y) and diacylglycerol kinase delta 1 (purple; PDB ID 3bq7). (**B**) Superposition of hSARM1^{SAM2} (green) with EphA2/SHIP2 complex (cyan; PDB ID 5zrx), EphA6/din complex (wheat; PDB ID ID5zry) and caskin-1 (blue; PDB ID 3sen). **(C)** Superposition of hSARM1^{tSAM} (green) with tandem SAM domains. Superposition of hSARM1^{tSAM} with caskin-2 tandem SAM domains (cyan, PDB ID 4is7), the liprin-alpha/liprin-beta complex (orange, PDB ID 3tad), caskin-1 tandem SAM domains (grey, PDB ID 3sen), STIM EF-SAM (pink, PDB ID 2l5y) and the AIDA-1 tandem SAM domain (yellow, PDB ID 2kiv).

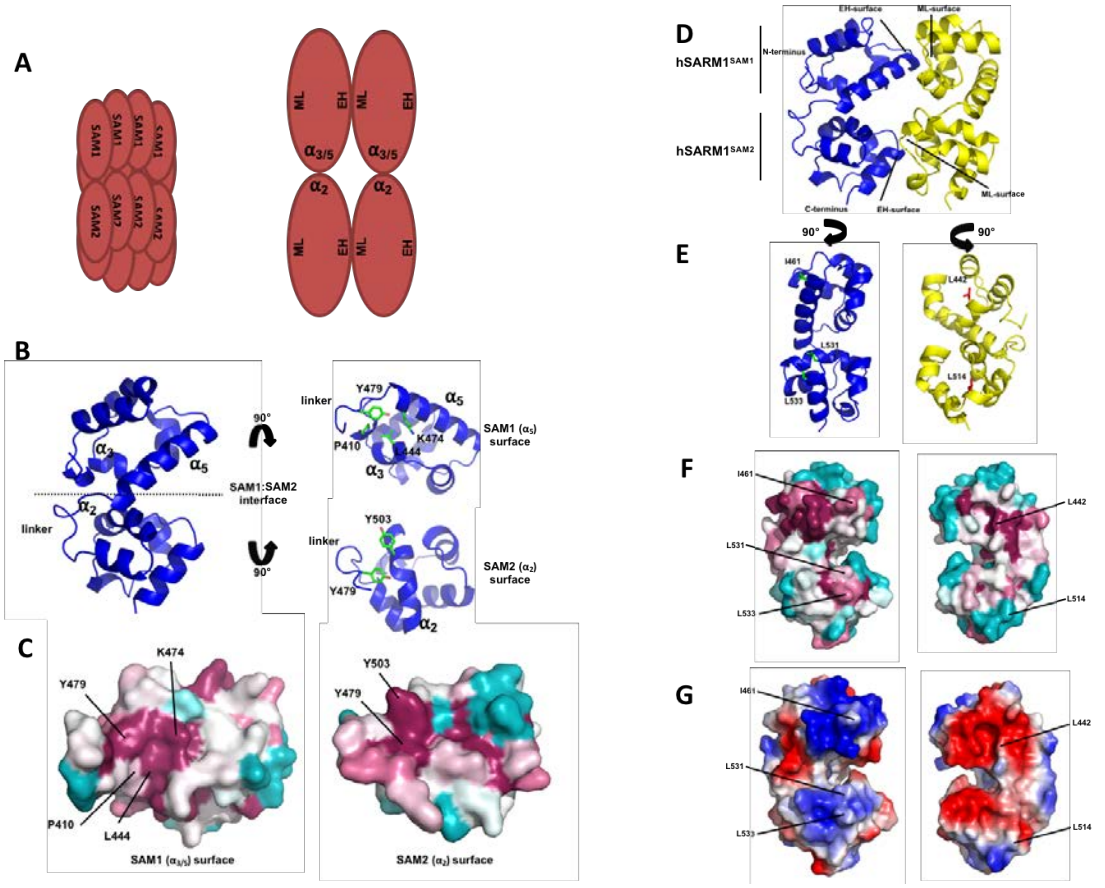

Fig. S4. Interactions in the hSARM1^{tSAM} octamer. (**A**) Schematic diagram of the hSARM1^{tSAM} octamer and the three types of interactions. (**B**) Left, cartoon representation of the hSARM1^{SAM1}:hSARM1^{SAM2} interface of hSARM1^{tSAM}. The two SAM domains form an asymmetric dimer with major interactions involving the α3 and α5 helix of hSARM1^{SAM1}, the α2 helix of hSARM1^{SAM2} and the linker region between the two domains. Right, the hSARM1^{SAM1}:hSARM1^{SAM2} interface facing the plane of the page. hSARM1^{SAM1} and hSARM1^{SAM2} are rotated –90° and 90°, respectively, around the horizontal axis compared to the view on the left, and residues buried at the interface are displayed in stick representation. (**C**) Surface representation of the hSARM1^{SAM1} and hSARM1^{SAM2} regions involved in the intramolecular interaction between SAM domains in hSARM1^{tSAM}. The surface is colored by sequence conservation calculated using ConSurf. The multiple sequence alignment used by ConSurf consisted of 104 unique tandem SAM domain sequences of predicted hSARM1 orthologs with sequence identities to hSARM1 ranging from 30-95%. Cyan corresponds to variable regions, while purple corresponds to conserved regions. (**D**) Cartoon representation of the hSARM1^{SAM1}:hSARM1^{SAM1} and hSARM1^{SAM2}:hSARM1^{SAM2} interface between hSARM1^{tSAM} molecules in the octameric assembly. The two hSARM1^{tSAM} molecules are colored blue and yellow and interact in head-to-tail fashion. The "head" contacts on both the hSARM1^{SAM1} and the hSARM1^{SAM2} surface are located at the start of the α5 helix and are centered on I461 in hSARM1^{SAM1} and V533 in hSARM1^{SAM2}. This interaction surface is commonly referred to as the EH surface. The "tail" contacts on the opposing hSARM1^{SAM1} and hSARM1^{SAM2} surfaces center on a shallow hydrophobic pocket formed primarily by residues V438, L442, L446 and L455 in hSARM1^{SAM1} and L510, L514, V518 and C527 in hSARM1^{SAM2}. This interaction surface involves the loop regions connecting

the helices of the SAM domains and is referred to as the ML surface. (**E**) The hSARM1^{SAM1}:hSARM1^{SAM1} and hSARM1^{SAM2}:hSARM1^{SAM2} interfaces facing the plane of the page. The two hSARM1^{tSAM} molecules are rotated –90° and 90°, respectively, around the vertical axis compared to (D), and residues buried at the interface are displayed in stick representation. (**F**) Surface representation as in (E), with the surface colored by sequence conservation calculated using ConSurf as described in (C). (**G**) Surface representation as in (E), with the surface colored by electrostatic potential calculated using PyMOL and APBS (*90*). Positive and negative potentials are indicated in blue and red, respectively, colored continuously between -5 and 5 kT/e.. Both interfaces are stabilised by polar interactions and have complementary electrostatic properties; the EH surface is electropositive, while the ML surface is electronegative.

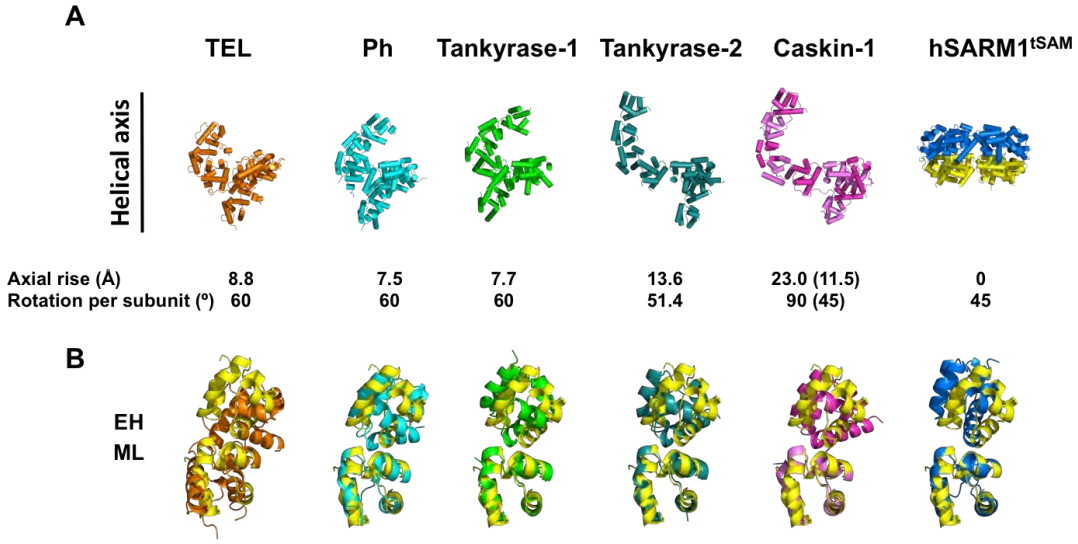

Fig. S5. Structural comparison of SAM domain assemblies. (**A**) Cartoon representation of the TEL, polyhomeotic, tankyrase-1, tankyrase-2, and caskin-1 polymers and the hSARM1^{tSAM} ring. (**B**) Superposition of the ML:EH interactions in TEL, polyhomeotic, tankyrase-1, tankyrase-2, caskin-1 polymers with the ML:EH interaction between hSARM1^{SAM2} domains in hSARM1^{tSAM} reveals that the ML:EH interface is similar, but the novel rigid association of the two SAM domains in SARM1 imposes constraints on the geometry of the hSARM1^{SAM1}:hSARM1^{SAM1} and hSARM1^{SAM2}:hSARM1^{SAM2} subunit interactions, resulting in a zero axial rise per hSARM1^{tSAM} subunit. The rotation per hSARM1^{tSAM} subunit is 45°, resulting in ring formation after association of eight hSARM1^{tSAM} molecules.

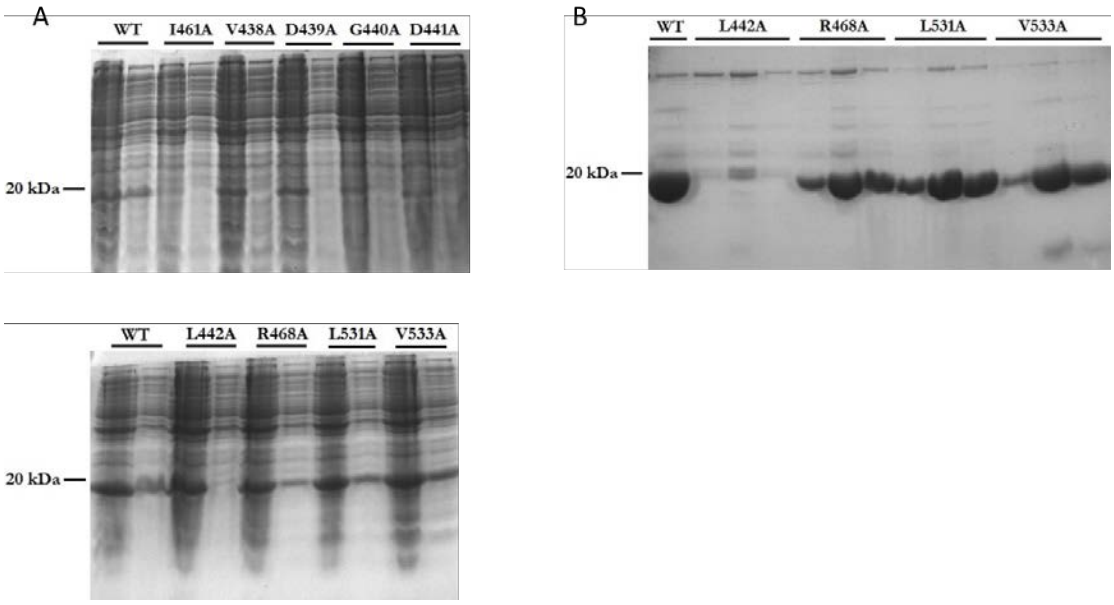

Fig. S6. Effects of hSARM1^{tSAM} interface mutations. We first tested single alanine mutations of the hSARM1^{SAM1} EH surface residues I461 and R468, the hSARM1^{SAM2} EH surface residues L531 and V533, and the hSARM1^{SAM1} ML surface residues V438, D439, G440, D441 and L442. G440 is not directly involved in hSARM1^{SAM1}:hSARM1^{SAM1} interactions, but the residue is likely to stabilise the ML surface region. All of the mutant proteins expressed well, but only three of them, R468A, L531A and V533A produced soluble protein, and L531A and V533A precipitated after elution from the IMAC column and could not be analysed by SEC. The R468A mutant eluted at a similar elution volume as wild-type hSARM1^{tSAM}, demonstrating no disruption of the oligomer. (**A**) SDS-PAGE analysis of the insoluble and soluble fractions of the hSARM1^{tSAM} single-residue mutants after expression in *E. coli* (left and right lanes, respectively, per mutant)**.** The cells were lysed by sonication and the insoluble and soluble fractions were separated by centrifugation (39,191 x *g* for 30 min). (**B**) SDS-PAGE analysis of the IMAC elution fractions for wild-type hSARM1^{tSAM} and the L442A, R468A, L531A and V553A mutants.

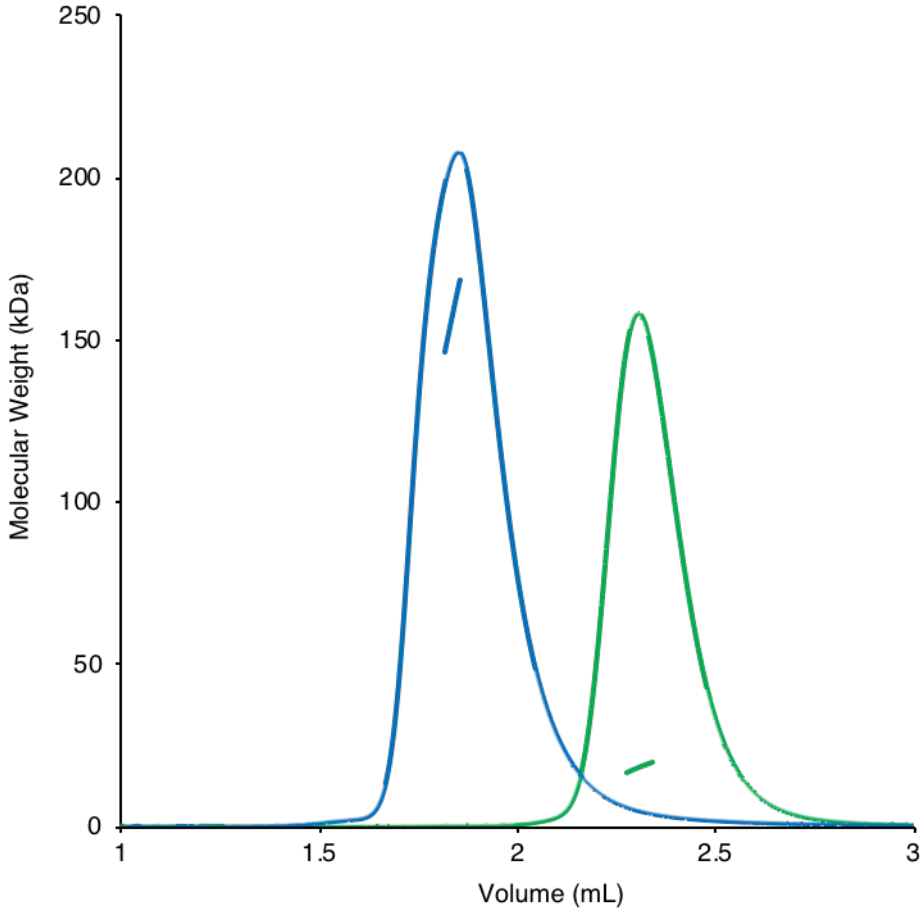

Fig. S7. SEC-MALS analysis of mSARM1^{tSAM} and mSARM1$^{tSAM(5Mut)}$. Solution properties of mSARM1^{tSAM} (wild-type) and mSARM1$^{tSAM(5Mut)}$ (L442R, I461D, L514D, L531D, and V533D), analyzed by SEC-MALS. Blue and green peaks indicate the traces from the refractive index (RI) detector during SEC of mSARM1^{tSAM} or mSARM1$^{tSAM(5Mut)}$, respectively. The lines under the peaks correspond to the average molecular-mass distributions across the peak.

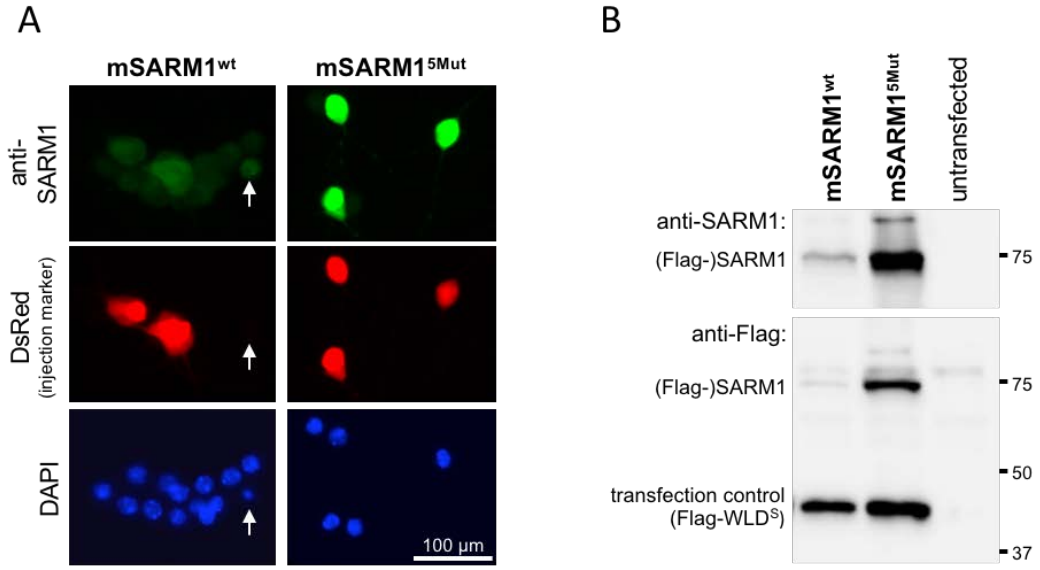

Fig. S8. Expression of mSARM1^{wt} and mSARM1$^{(5Mut)}$. (**A**) Exogenous expression of Flag-tagged mSARM1^{wt} and mSARM1$^{tSAM(5Mut)}$ in *Sarm1*$^{-/-}$ SCG neurons. Neurons were injected with constructs for Flag-tagged mSARM1^{wt} or mSARM1$^{tSAM(5Mut)}$ at 10 ng/µL together with 40 ng/µL DsRed expression construct as an injection marker. Cells were fixed and immuno-stained using a mSARM1 antibody. Nuclei were counter-stained with DAPI. While both mSARM1^{wt} and mSARM1$^{tSAM(5Mut)}$ are detectable above (non-specific) background staining, mSARM1$^{tSAM(5Mut)}$ is clearly and reproducibly expressed at a higher level. mSARM1^{wt}, but not mSARM1$^{tSAM(5Mut)}$, also causes ~50% of injected neurons to undergo cell death (data not shown). An example of this is indicated by an arrow showing a mSARM1-positive cell with a pyknotic nucleus in which DsRed signal is no longer seen. (**B**) Exogenous expression of Flag-tagged mSARM1^{wt} and mSARM1^{5Mut} in HEK cells. Representative immunoblot of extracts from HEK cells transfected with constructs for Flag-tagged mSARM1^{wt} or mSARM1^{5Mut}, together with a construct for a reference Flag-tagged protein (Flag-WLD^{S}) to control for transfection efficiency. mSARM1 variants are detected by both SARM1 and Flag antibodies at the expected size (labelled in kDa) in the transfected cells only. As in SCGs, mSARM1^{5Mut} is reproducibly expressed at a higher level than wild-type mSARM1.

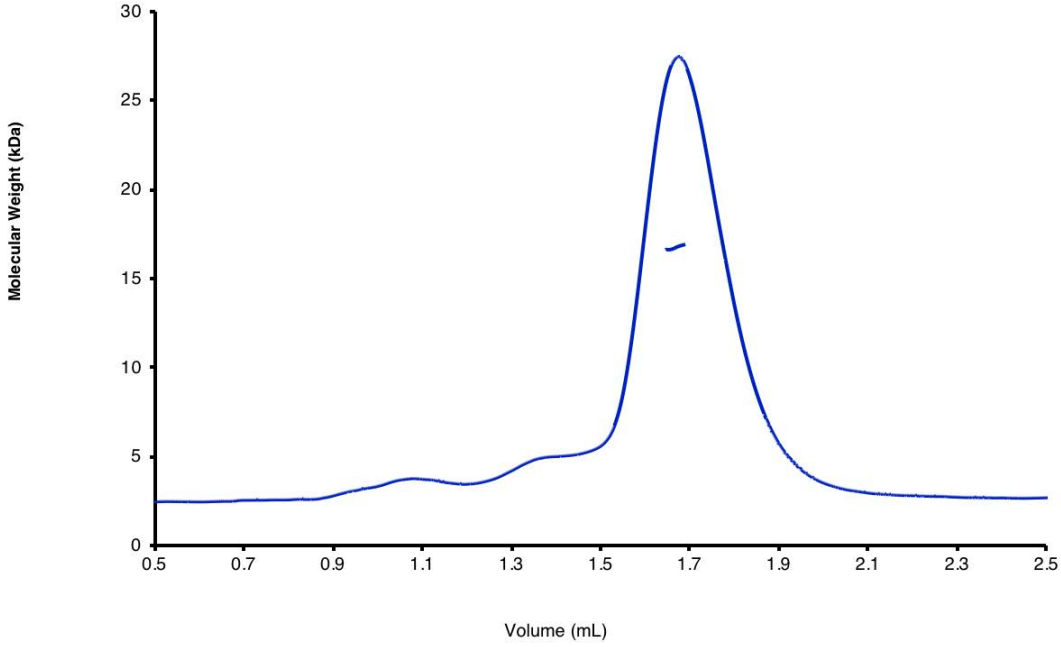

Fig. S9. SEC-MALS analysis hSARM1^{TIR}. Shown is the trace from the refractive index (RI) detector during SEC; the lines under the peak correspond to the average molecular mass distributions across the peak. Theoretical molecular weight of hSARM1^{TIR} is 15.93 kDa.

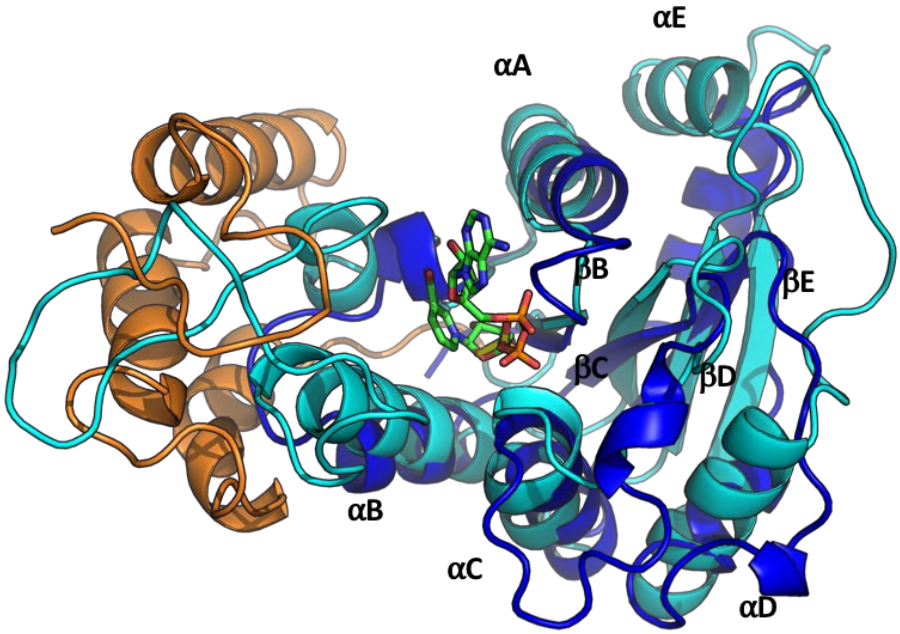

Fig. S10. Comparison of hSARM1^{TIR} and CD38 structures. Superposition (RMSD of 3.3 Å for 112 equivalent Cα atoms) of hSARM1^{TIR} (blue) bound to glycerol (yellow) and the C-terminal region of the human CD38 ecto-domain (cyan, PDB ID 2i65) bound to NAD^+ (green). The N-terminal region of CD38 is highlighted in orange. The elements of secondary structure in hSARM1^{TIR} are labelled.

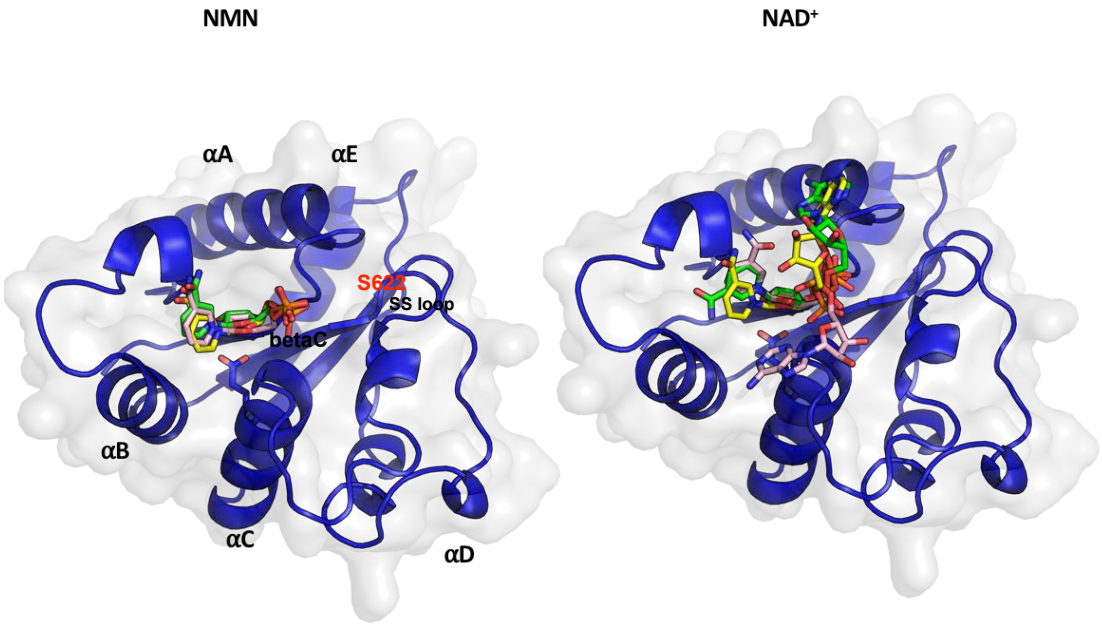

Fig. S11. Molecular docking of NMN and NAD$^+$ to hSARM1^{TIR}. Molecular docking of NMN (left panel) and NAD$^+$ (right panel) to hSARM1^{TIR} was carried out using Glide (Schrodinger) and the crystal structure of hSARM1^{TIR}. The top-three docking poses are shown (yellow, pink and green) in stick representation.

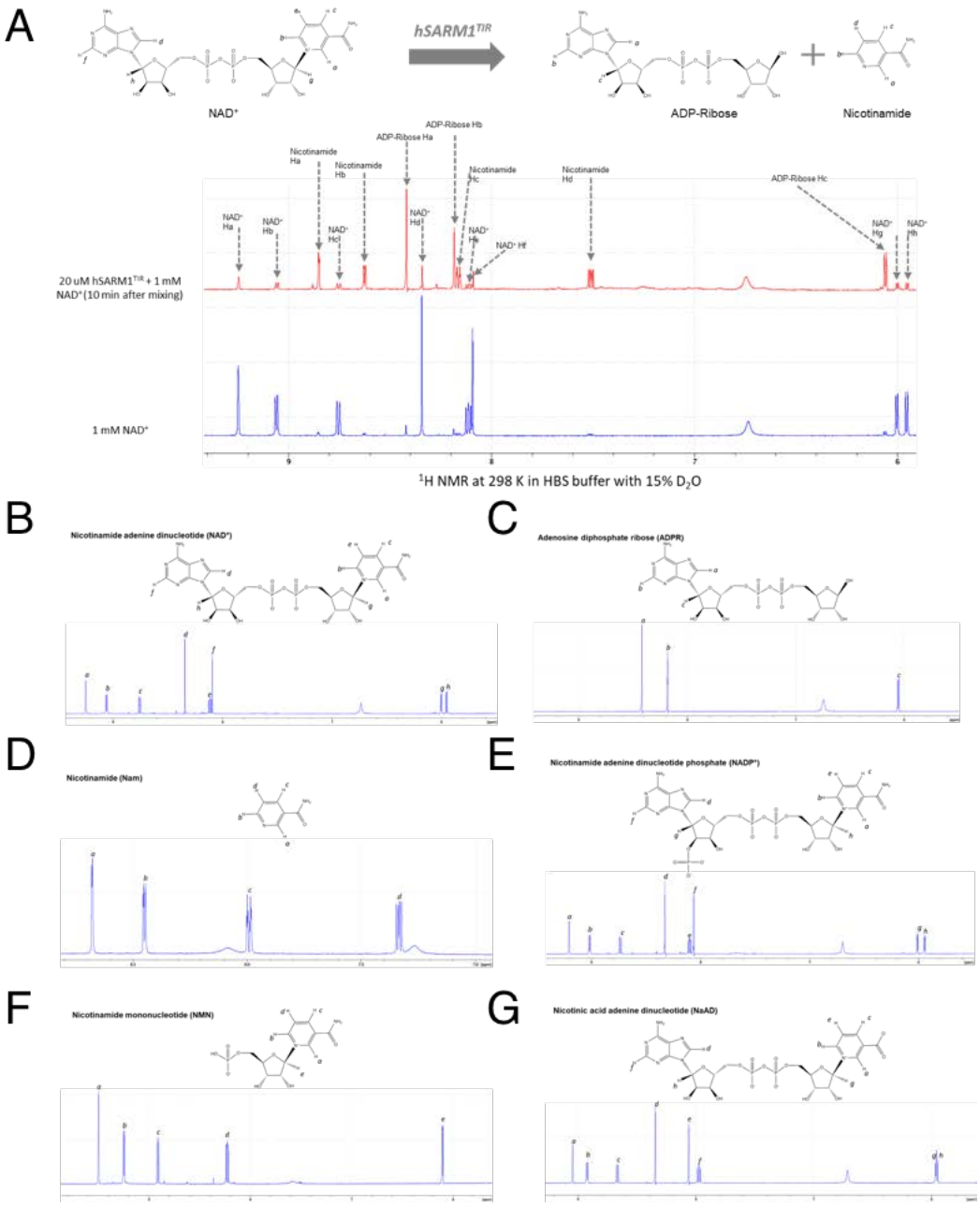

Fig. S12. Assignments of ^{1}H NMR peaks for enzyme substrates and products in their aromatic regions. Peaks for each compound are labelled alphabetically according to their chemical shift values, and the peaks that were subjected to integration for calculation of catalytic activity are labelled with "*". (**A**) hSARM1^{TIR} NAD^{+} cleavage reaction. **(B)** L6^{TIR} NAD^{+} cleavage reaction. **(C)** Run1^{TIR} NAD^{+} cleavage reaction. (**D**) NAD^{+}. (**E**) ADPR. (**F**) Nam. (**G**) NADP^{+}. (**H**) NMN. (**I**) NaAD. (**J**) FAD.

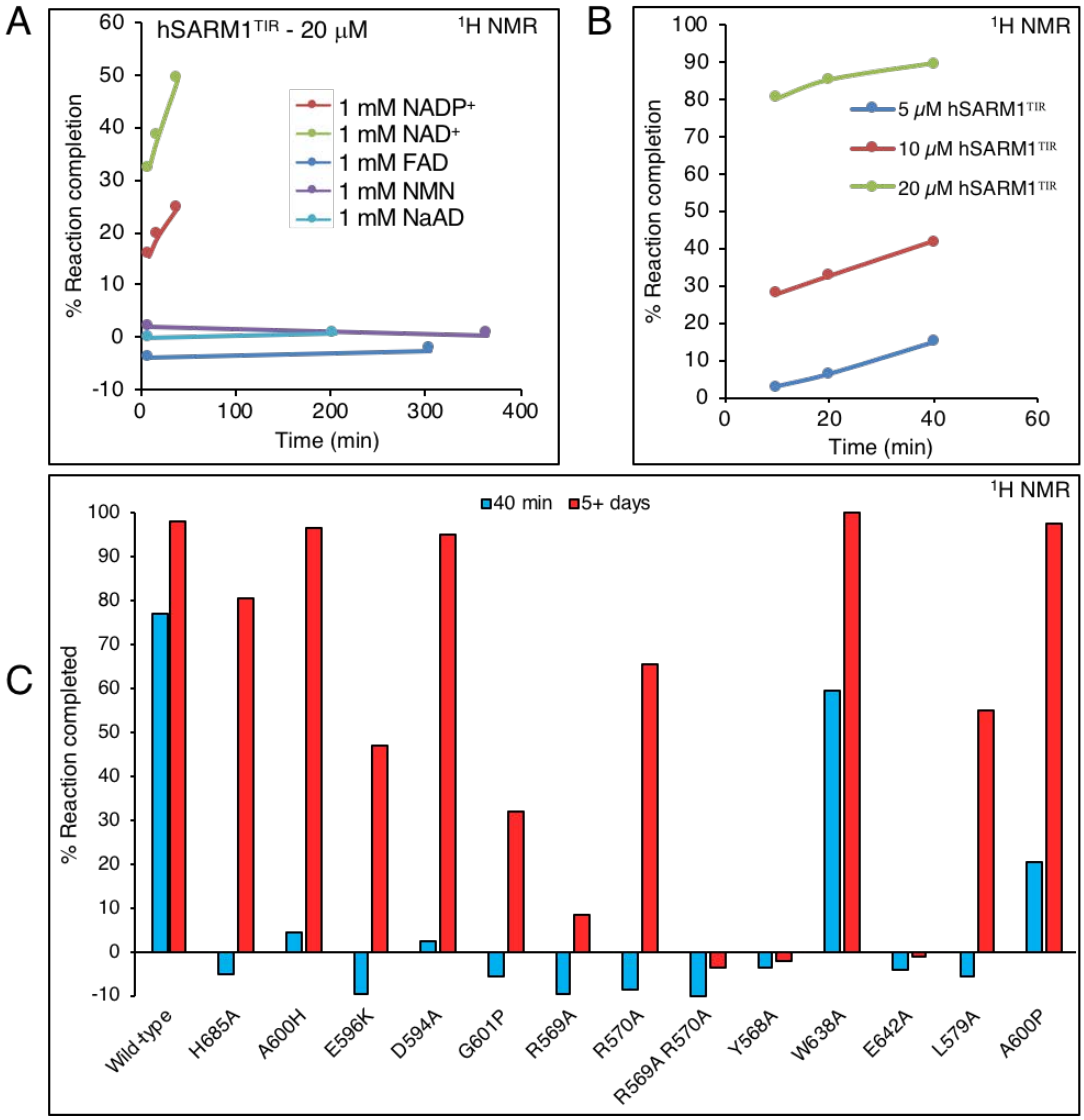

Fig. S13. Cleavage, by hSARM1^{TIR} and its mutants, of potential substrates and its concentration dependence. (**A**) NAD$^+$, NADP$^+$, NMN, NaAD and FAD cleavage-reaction time-courses of hSARM1^{TIR}, monitored by ^{1}H NMR (298 K), using a protein concentration of 20 µM and 1 mM substrate. (**B**) NAD$^+$ cleavage-reaction time-courses of hSARM1^{TIR} monitored by ^{1}H NMR (20°C), using different protein concentrations and 1 mM NAD$^+$. (**C**) Bar chart of NAD$^+$ cleavage reaction of wild-type human SARM1^{TIR} and its mutants, monitored by ^{1}H NMR (298 K), using 1 mM NAD$^+$. [NAD$^+$] remaining was determined at two time-points: 40 min and 5 days.

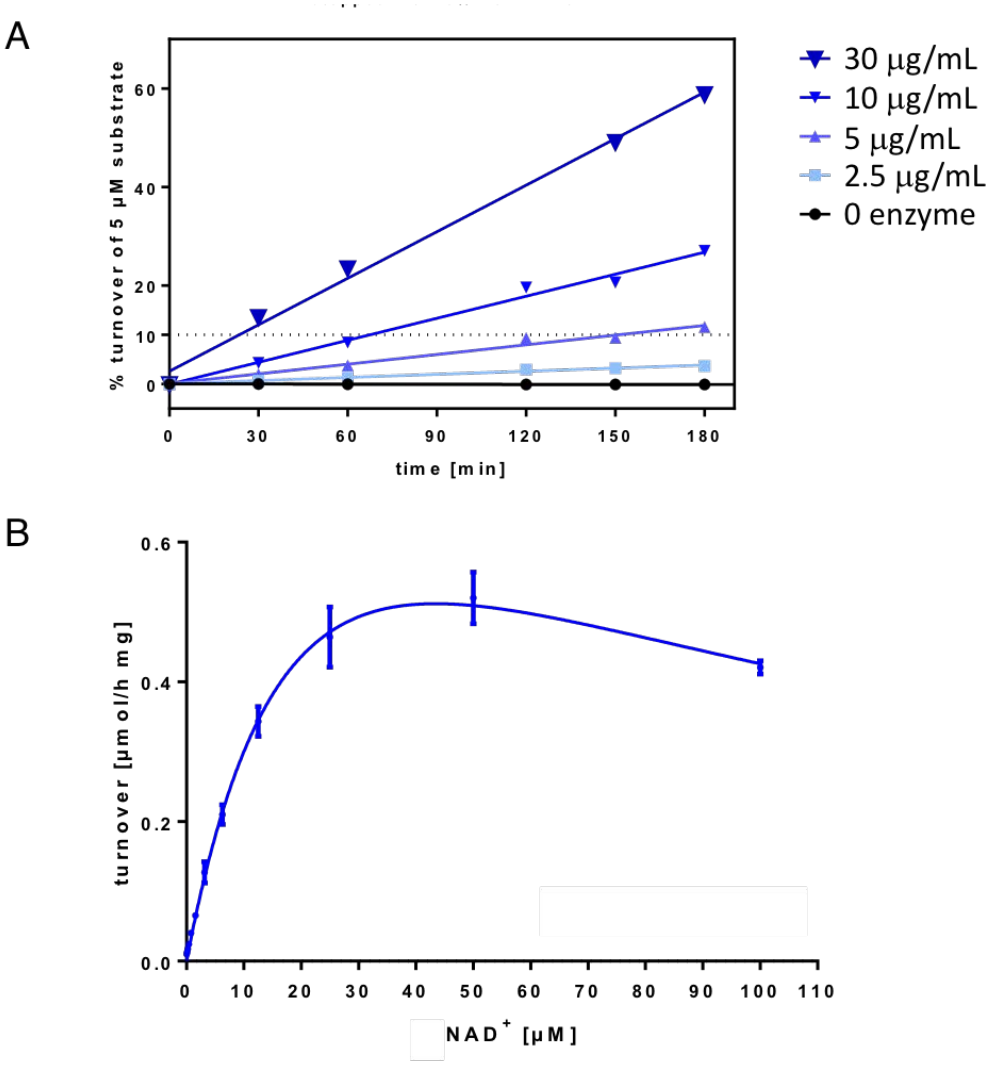

Fig. S14. Enzyme kinetics of NADase activity by hSARM1$^{tSAM\text{-}TIR}$. (**A**) Percent turnover of 5 µM NAD^+ as a function of time, at different concentrations of hSARM1$^{tSAM\text{-}TIR}$, measured using the mass spectrometry-based assay. (**B**) Turnover as a function of NAD^+ concentration, based on data present in (A); the derived kinetic parameters: K_m = 26 mM; V_{max} = 2.3 mmol/h.mg; K_I = 71 mM.

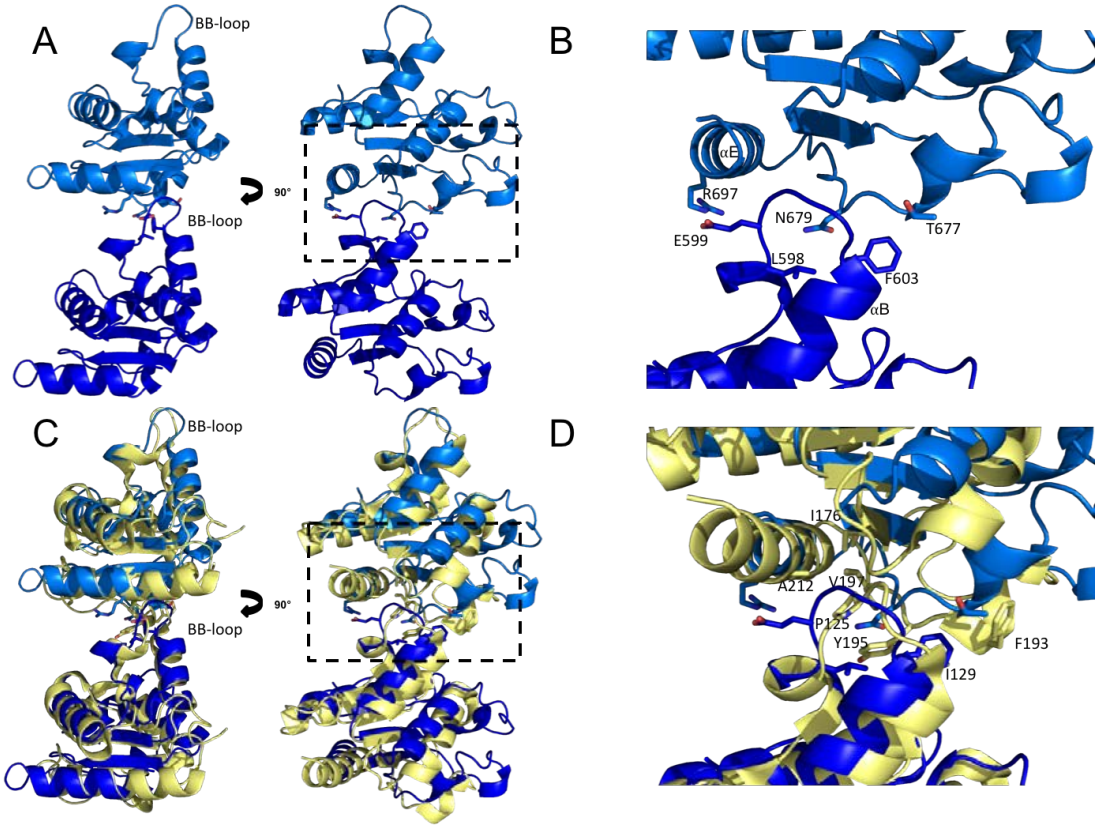

Fig. S15. BB-loop interfaces in the crystals of hSARM1^{TIR} and MAL^{TIR} filaments. (**A**) Cartoon representation of two molecules of hSARM1^{TIR} (light and dark blue) interacting through the BB-loop interface in the crystals. Interacting residues are shown in stick representation. (**B**) Zoom-in of the interface, shown as in (A). (**C**) Superposition of two molecules of hSARM1^{TIR} (blue) and two molecules of MAL^{TIR} (PDB ID 5uzb) (*3*) (yellow), shown as in (A). (**D**) Zoom-in of the superposition, shown as in (C).

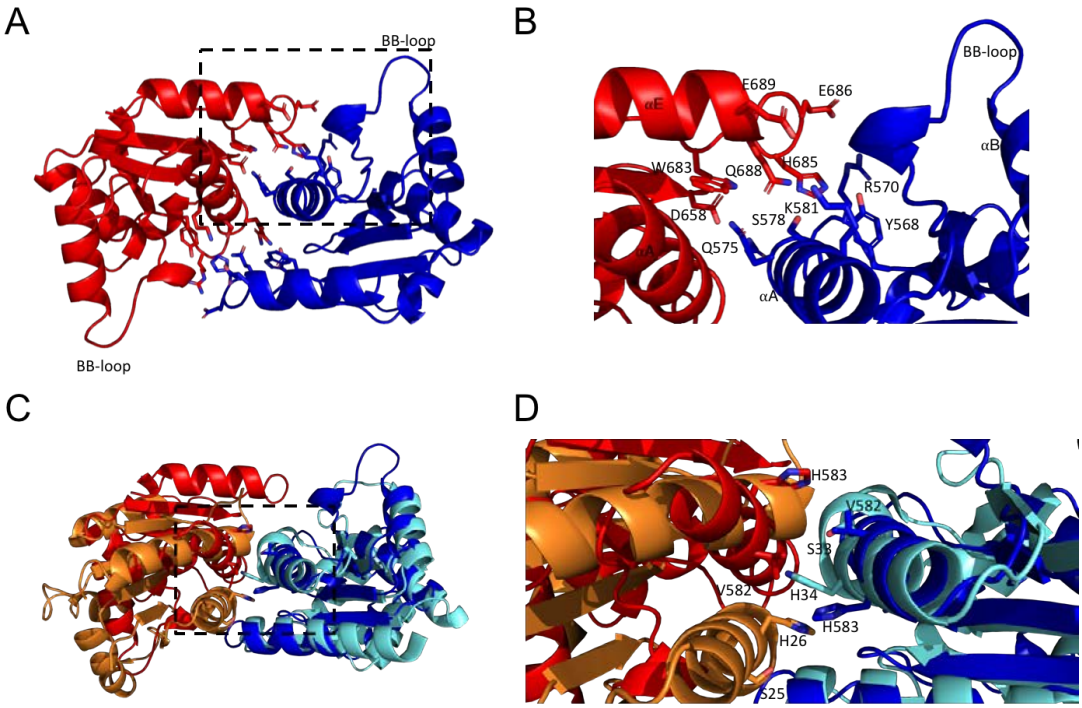

Fig. S16. AE interfaces in the crystals of hSARM1^{TIR} and RPS4^{TIR}:RRS1^{TIR} complex. (**A**) Cartoon representation of two molecules of hSARM1^{TIR} (red and blue) interacting through the AE interface in the crystals. Interacting residues are shown in stick representation. (**B**) Zoom-in of the interface, shown as in (A). (**C**) Superposition of two molecules of hSARM1^{TIR} (red and blue) and two molecules of RPS4^{TIR}:RRS1^{TIR} complex (PDB ID 4c6t) (*91*) (orange and cyan), shown as in (A). (**D**) Zoom-in of the superposition, shown as in (C).

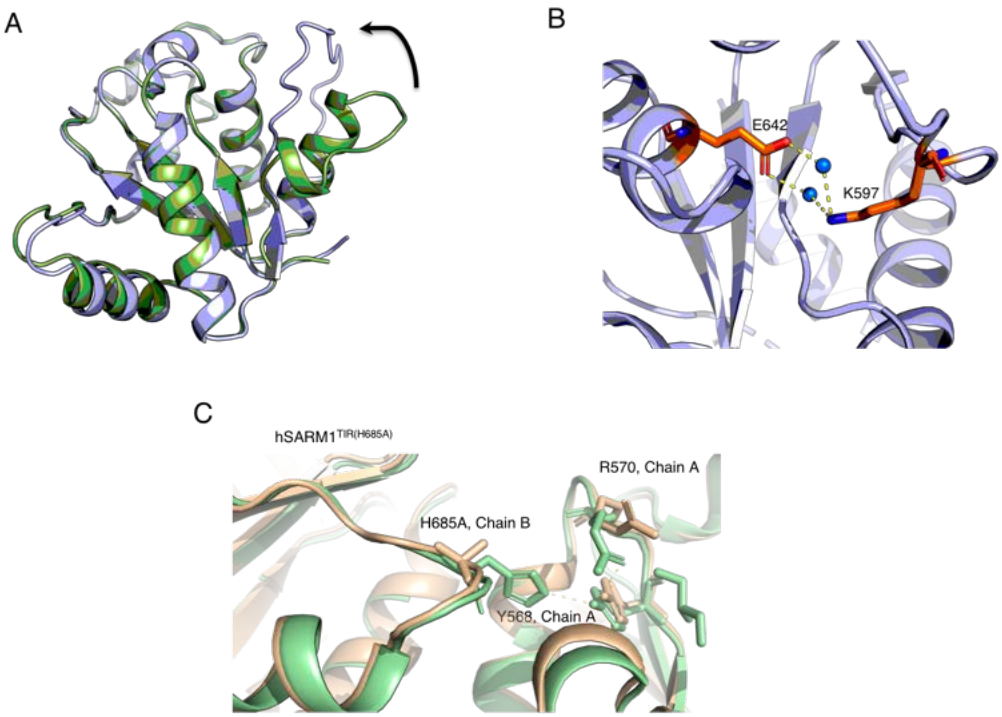

Fig. S17. Structures of hSARM1$^{TIR(G601P)}$ and hSARM1$^{TIR(H685A)}$. (**A**) Superposition of hSARM1^{TIR} (green) and "ligand-free" hSARM1$^{TIR(G601P)}$ (blue), displaying conformational changes in the BB loop (highlighted by an arrow). (**B**) Interaction of the catalytic glutamate (E642) and a lysine from the BB loop (K597) in "ligand-free" hSARM1$^{TIR(G601P)}$. (**C**) Structural alignment of wild-type (glycerol-bound; glycerol not shown) hSARM1^{TIR} (green) and unliganded hSARM1$^{TIR(H685A)}$ (wheat), displaying conformational changes in the AE interface.

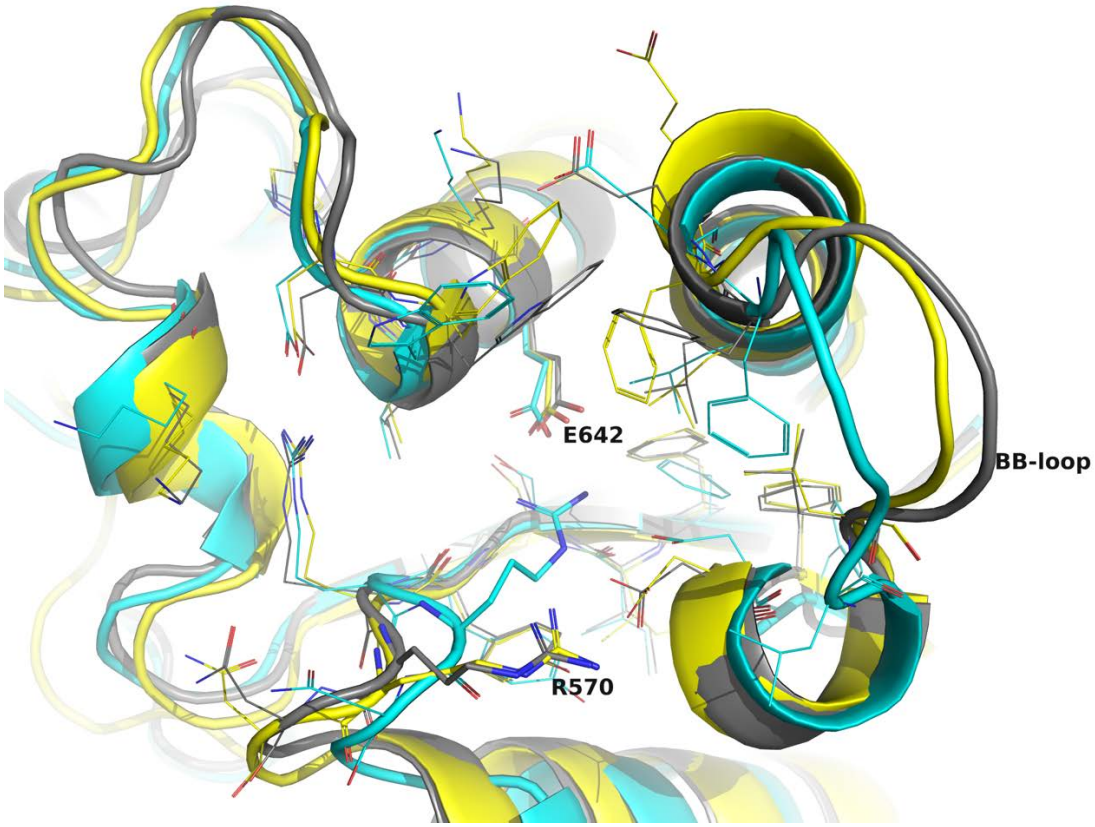

Fig. S18. Molecular dynamics simulations of monomeric and oligomeric forms of hSARM1^{TIR}. Representative structures from MD simulations of the monomer (cyan cartoon) and the hexamer (yellow cartoon) were superimposed onto the crystal structure of hSARM1^{TIR} (grey cartoon). Binding-site residues are shown in stick representation, with R570 and E642 labelled. Carbon atoms are colored according to their cartoon representation colors; nitrogens are colored blue; oxygens are colored red. Representative structures generated from the final 20 ns of triplicate 50-ns MD runs show significant differences between active-site conformations in the monomer and the hexamer. The hexamer maintained the conformations of most residues in the active site, whereas those of the monomer deviated from the crystal structure. Notably, the BB loop in the monomer shifted >6 Å away from the crystal structure, while in the hexamer it moved <2 Å. Concomitant deviation of the αB helical region in the monomer was also observed, with considerable changes in the conformation of E642. R570 moves into the active site to interact with E642, which would likely inhibit substrate binding and catalytic activity. Active-site residues of the monomer also exhibit higher fluctuations (Table S7), and thus less structural stability, than those of the hexamer, especially residues around the αB helical region. Therefore, MD simulations demonstrate the ability of the hexamer to maintain and stabilize the active-site structure of hSARM1^{TIR}, explaining the higher activity upon self-association.

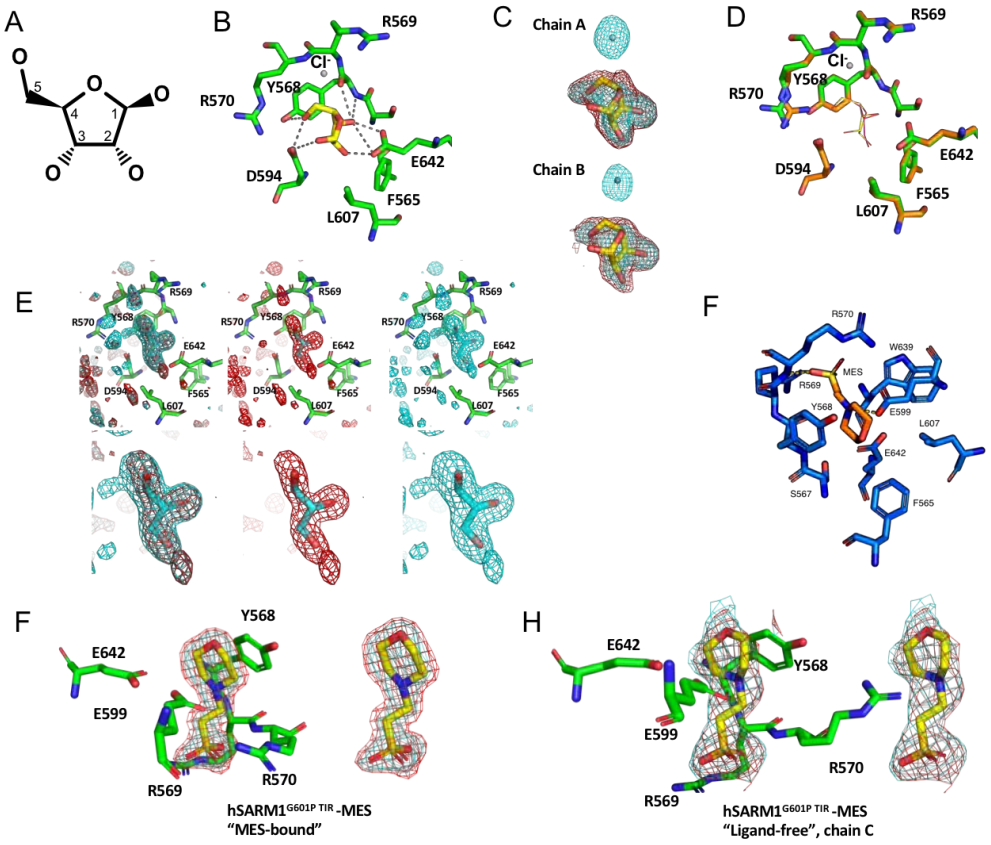

Fig. S19. Crystal structures of hSARM1^{TIR} ligand complexes. (**A**) 2D structure of β-D-ribose. (**B**) Stick representation of β-D-ribose and residues in the catalytic pocket of hSARM1^{TIR} (chain A). The active-site chloride ion is displayed as a grey sphere. Interactions between β-D-ribose and residues of the active site at ≤ 3.6 Å are shown as grey dashed lines. The C2 and C3 hydroxyl groups interact with the carboxylate group of E642. The complex is further stabilised by polar interactions between; (i) the C3 hydroxyl group and the main-chain amide and carbonyl of Y568; and (ii) the C5 hydroxyl group and side-chains of Y568, R570, and D594. There are no structural changes in the active site region between the D-ribose and glycerol-bound structures. (**C**) "Omit" electron density maps of the β-D-ribose molecule and chloride ion in chain A (top panel) and B (bottom panel). Standard omit and Polder omit *mFo-DFc* maps (β-D-ribose only), contoured at 3.0 σ, are shown in cyan and red, respectively. (**D**) Superimposition of the hSARM1^{TIR} D-ribose and glycerol complex structures, displayed in green and orange, respectively. (**E**) Standard omit (blue mesh) and Polder (red mesh) *mFo-DFc* maps for glycerol-bound wild-type hSARM1^{TIR}, contoured at 3.0 σ, shown as seen in B-D. (**F**) MES-binding site in "MES-bound" hSARM1$^{TIR(G601P)}$, shown in the same orientation as the structure diagrams in Fig. 3F. (**G**) Standard omit (magenta mesh) and Polder (red mesh) *mFo-DFc* maps for the MES molecule in the

"MES-bound" crystal of hSARM1$^{TIR(G601P)}$, contoured at 3.0 σ. (**H**) Standard omit (magenta mesh) and Polder (red mesh) *mFo-DFc* maps for the MES molecule in the MES-bound protein molecule of the "ligand-free" crystal of hSARM1$^{TIR(G601P)}$, contoured at 3.0 σ.

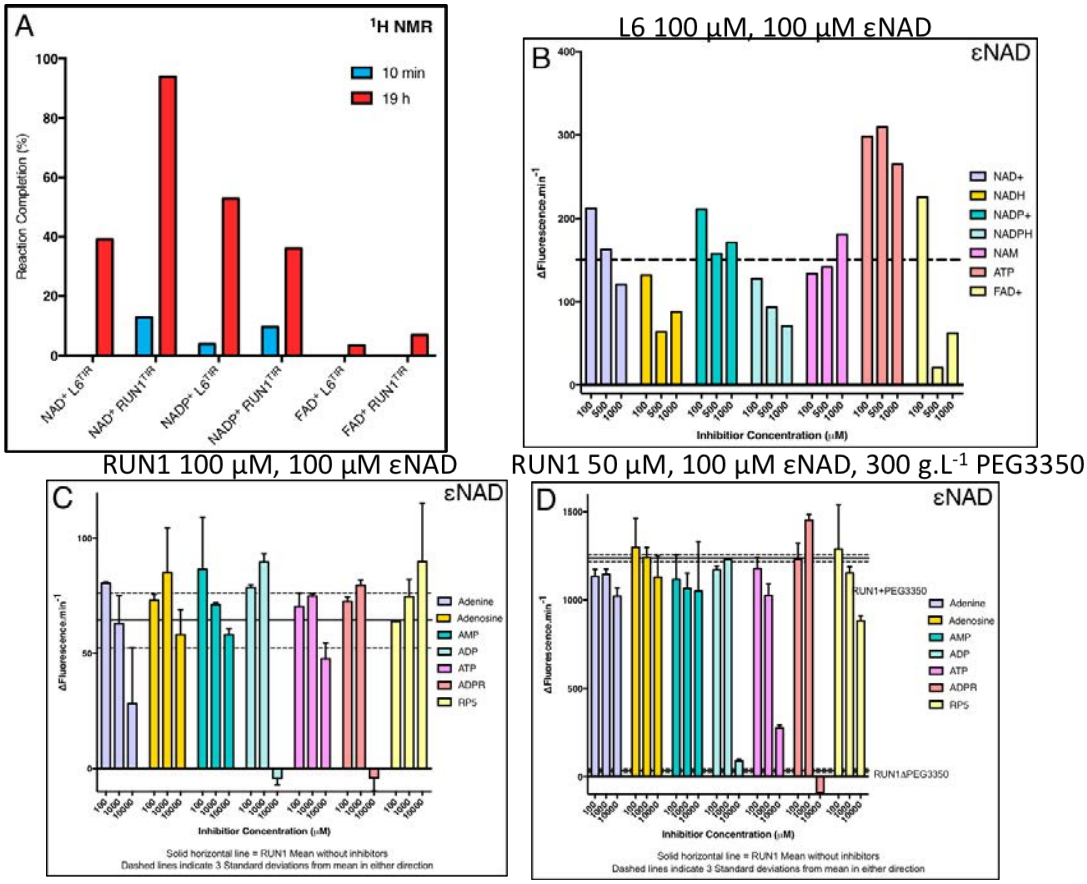

Fig. S20. NAD$^+$ cleavage by L6^{TIR} and RUN1^{TIR}. (**A**) NAD$^+$, NADP$^+$ and FAD cleavage reactions of RUN1^{TIR} and L6^{TIR} (100 µM) monitored by ^{1}H NMR using 1 mM substrate. (**B**) Effect of inhibitors on L6^{TIR} NADase activity (measured by the fluorescence assay using εNAD), using 100 µM L6^{TIR} and 100 µM εNAD. The dotted line indicates activity of L6^{TIR} without addition of inhibitors. (**C**) Effect of inhibitors on RUN^{TIR} NADase activity, using 100 µM RUN^{TIR} and 100 µM εNAD. The solid line indicates activity of RUN1^{TIR} without inhibitors, with the dotted line indicating three standard deviations from the mean. (**D**) the same as (C), but with 50 µM of RUN^{TIR} and 300 g.L^{-1} of PEG3350. AMP: adenosine monophosphate; ADP: adenosine diphosphate; ATP: adenosine triphosphate; ADPR: adenosine diphosphate ribose; RP5: ribose 5-phosphate.

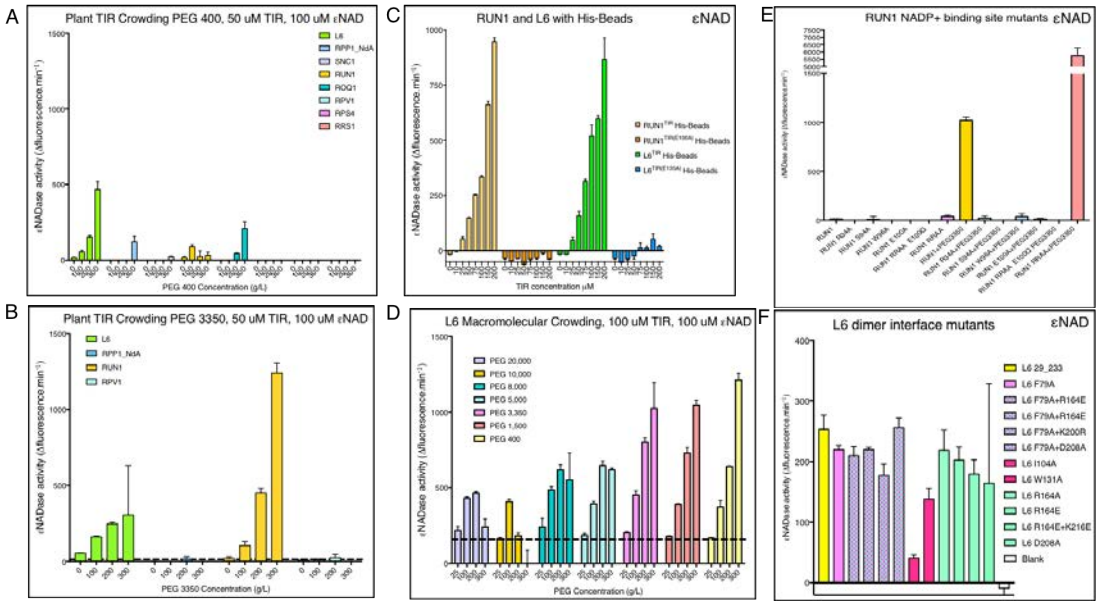

Fig. S21. Effect of macromolecular crowding and interface mutations on NAD$^+$ cleavage by plant TIR domains. (**A**) Macromolecular crowding effects of various concentrations of PEG400 and (**B**) PEG3350 on selected plant TIR domain NADase activities, measured by the fluorescence assay using εNAD. (**C**) Effects of Ni-NTA beads on RUN1^{TIR}, L6^{TIR} and their glutamate mutants, measured by the fluorescence assay using εNAD, at various protein concentrations. (**D**) Macromolecular crowding effects on L6^{TIR} NADase activity (measured by the fluorescence assay using εNAD), using PEGs of different masses and concentrations. (**E**) Effect of mutations on proposed NAD$^+$-binding site residues of RUN1^{TIR}, with and without PEG3350. (**F**) Effect of AE and DE interface mutations on L6^{TIR} and SNC1^{TIR} NADase activity.

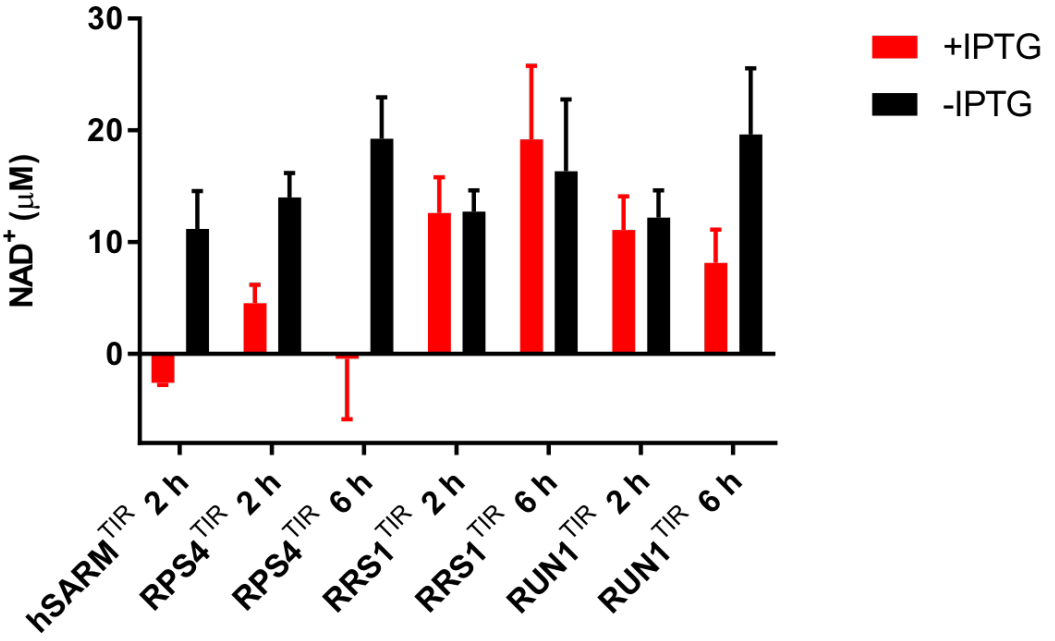

Fig. S22. NADase activities in lysates from *E. coli* expressing TIR domains. Endogenous levels of NAD^+ in Shuffle *E. coli* were measured after 2 h and 6 h induction by isopropyl β-D-1 thiogalactopyranoside (IPTG) at 30°C, using a cycling assay and NAD^+ standards. Data were generated from three biological duplicates.

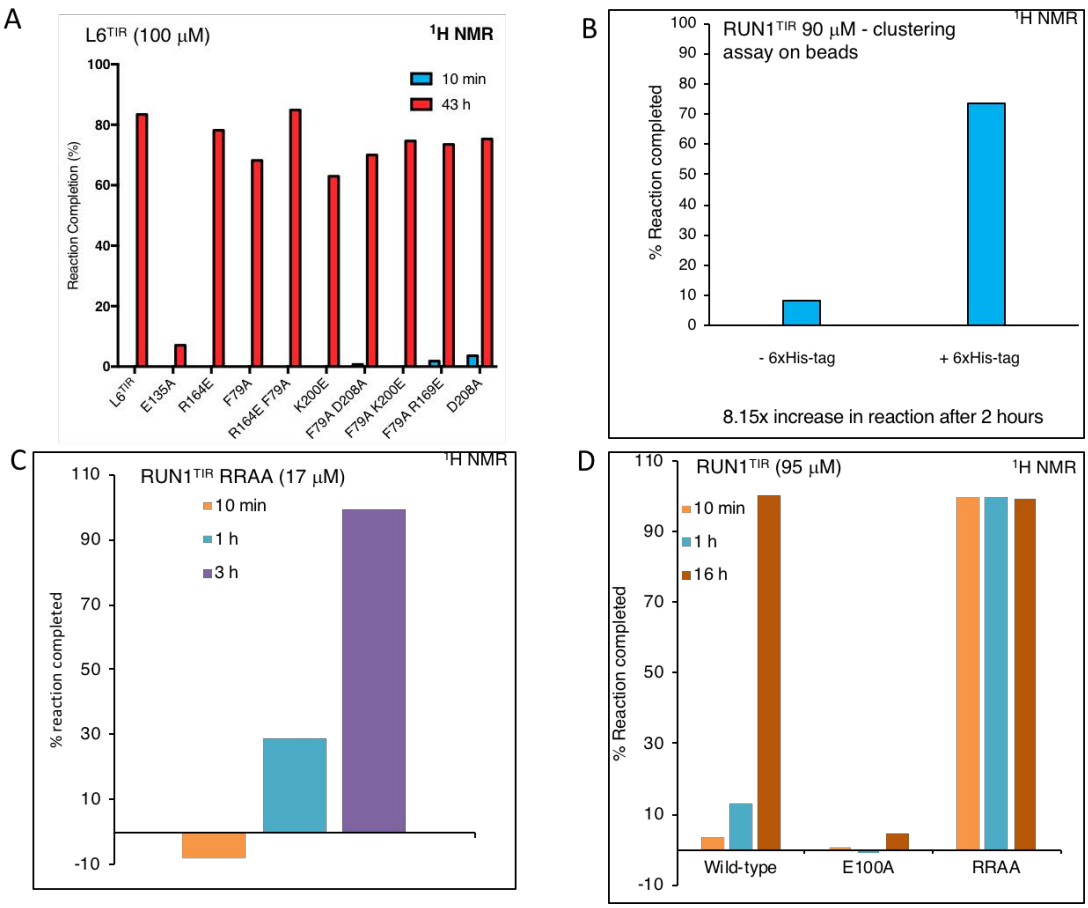

Fig. S23. NADase activities of L6^{TIR} and RUN1^{TIR} mutants monitored by ^{1}H NMR**.** (A) NAD^{+}-cleavage reaction of wild-type L6^{TIR} and its mutants (100 μM). (B) NAD^{+}-cleavage reaction by RUN1^{TIR} and 6xHis-tagged RUN1^{TIR} (90 μM) on Ni-NTA agarose beads. (C) NAD^{+}-cleavage reaction by the RUN1$^{TIR(R64A+R65A)}$ (RRAA) mutant (17 μM). (D) NAD^{+}-cleavage reaction by wild-type RUN1^{TIR} and its mutants (95 μM).

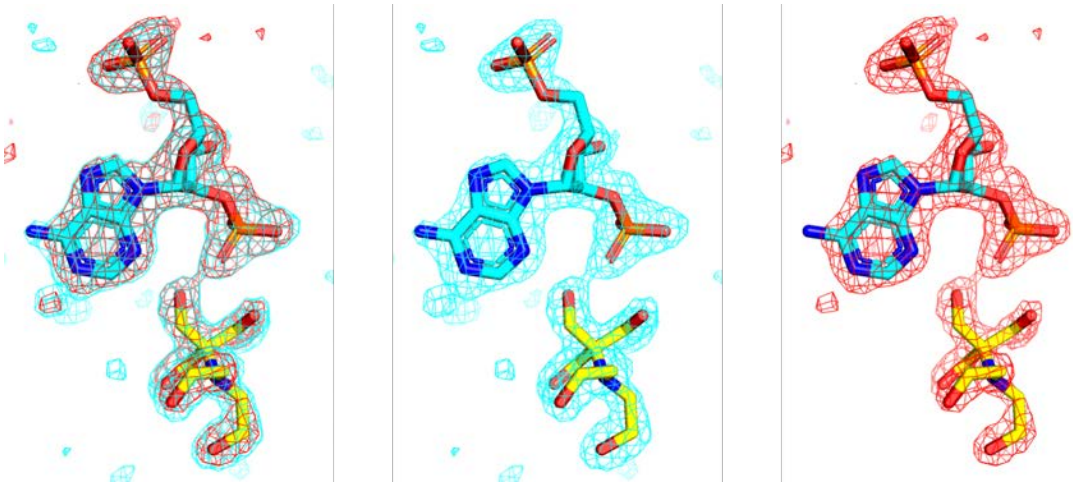

Fig. S24. Structure of NADP$^+$ bound to RUN1^{TIR}. Standard omit and Polder omit *mFo-DFc* maps, contoured at 3.0 σ, are shown in cyan and red, respectively, superimposed onto the models of NADP, cyan, and Bis-Tris, yellow, molecules from the RUN1^{TIR}:NADP$^+$ complex structure.

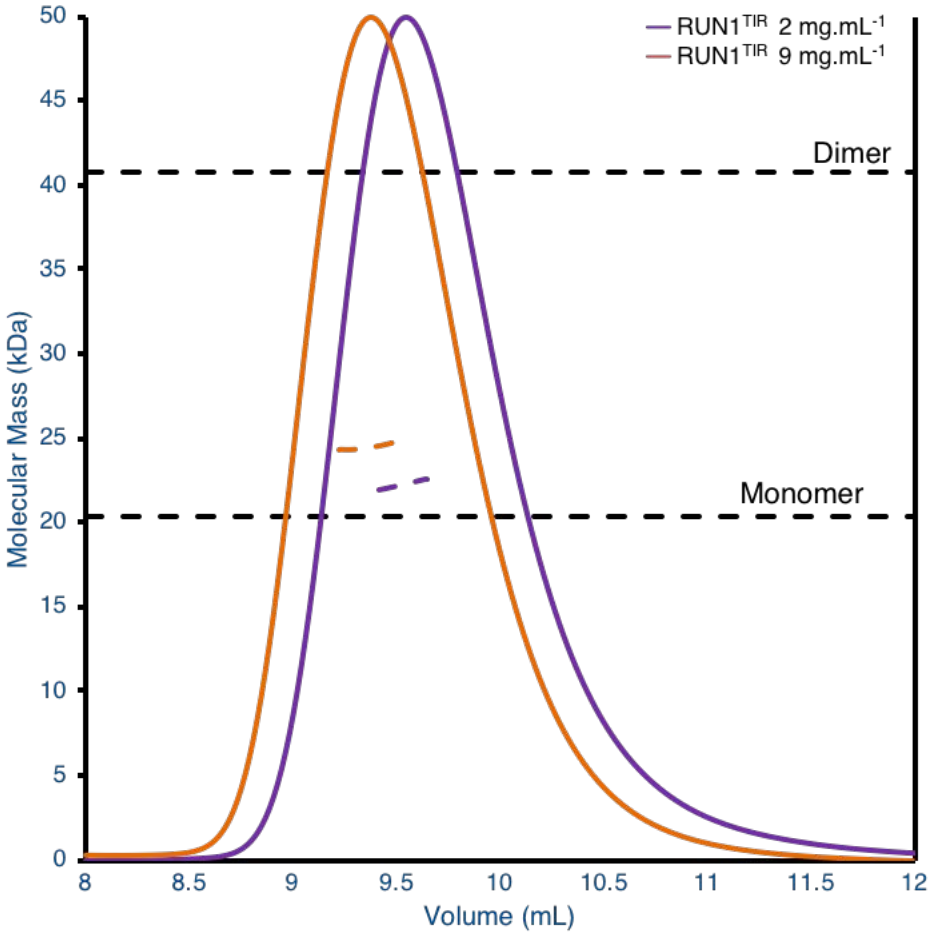

Fig. S25. Solution properties of RUN1^{TIR} as analysed by SEC-MALS. Purple and orange peaks indicate the traces from the refractive index (RI) detector during SEC of RUN1^{TIR} at 2 mg/mL and 9 mg/mL, respectively. The lines under the peaks correspond to the average molecular mass distributions across the peak. Theoretical dimer and monomer masses are shown by dotted lines.

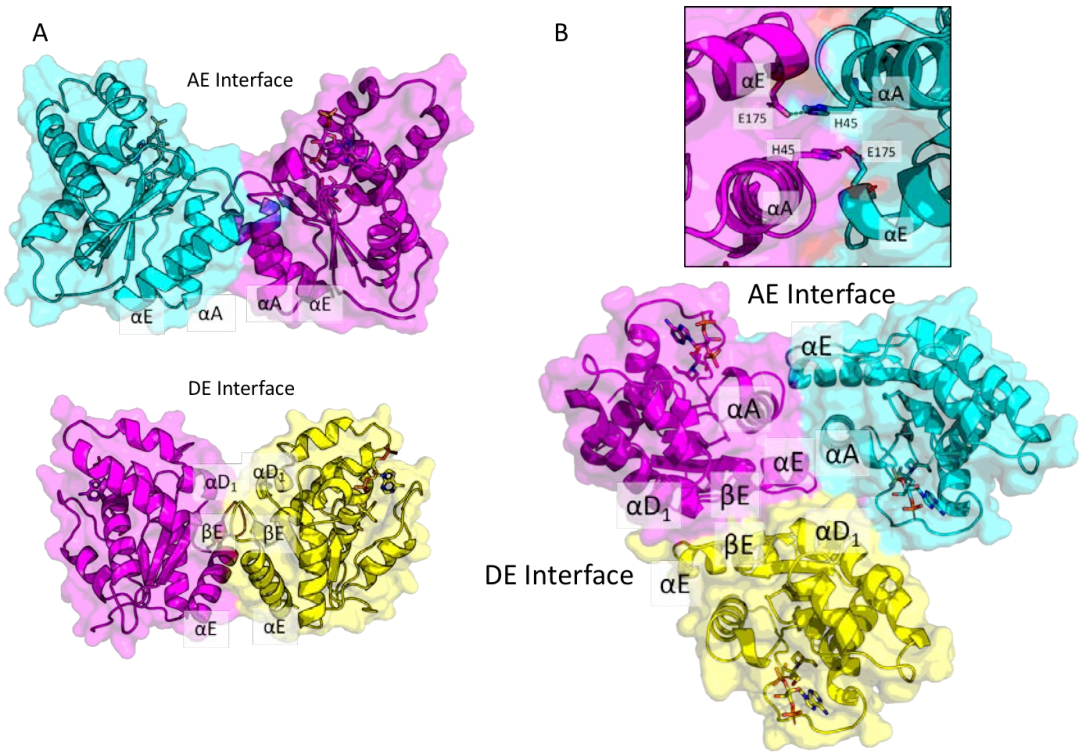

Fig. S26. AE and DE interfaces of RUN1^{TIR}. (**A**) The protomers interacting through the AE interface are shown in pink and cyan, while the protomers in the DE interface are shown in pink and yellow. (**B**) Both the AE and DE interfaces are observed in the crystals. The inset shows the stacking of H45 residues in the AE interface, reminiscent of other plant TIR domains (RPS4/RRS1, SNC1 and RPP1) (*6, 91*). The largest crystal lattice contact corresponds to the AE interface, with a combined buried surface area of ~1400 Å^2 (involving 18 interface residues from each TIR, 10 H-bonds and 2 salt bridges). The conserved histidine motif is at the center of the interface. The second largest crystal lattice contact corresponds to a DE interface, with a combined surface area of ~1140 Å^2 (19 interface residues, 4 H-bonds and 4 salt bridges). R131 forms an H-bond with D172, and S185 with E181.

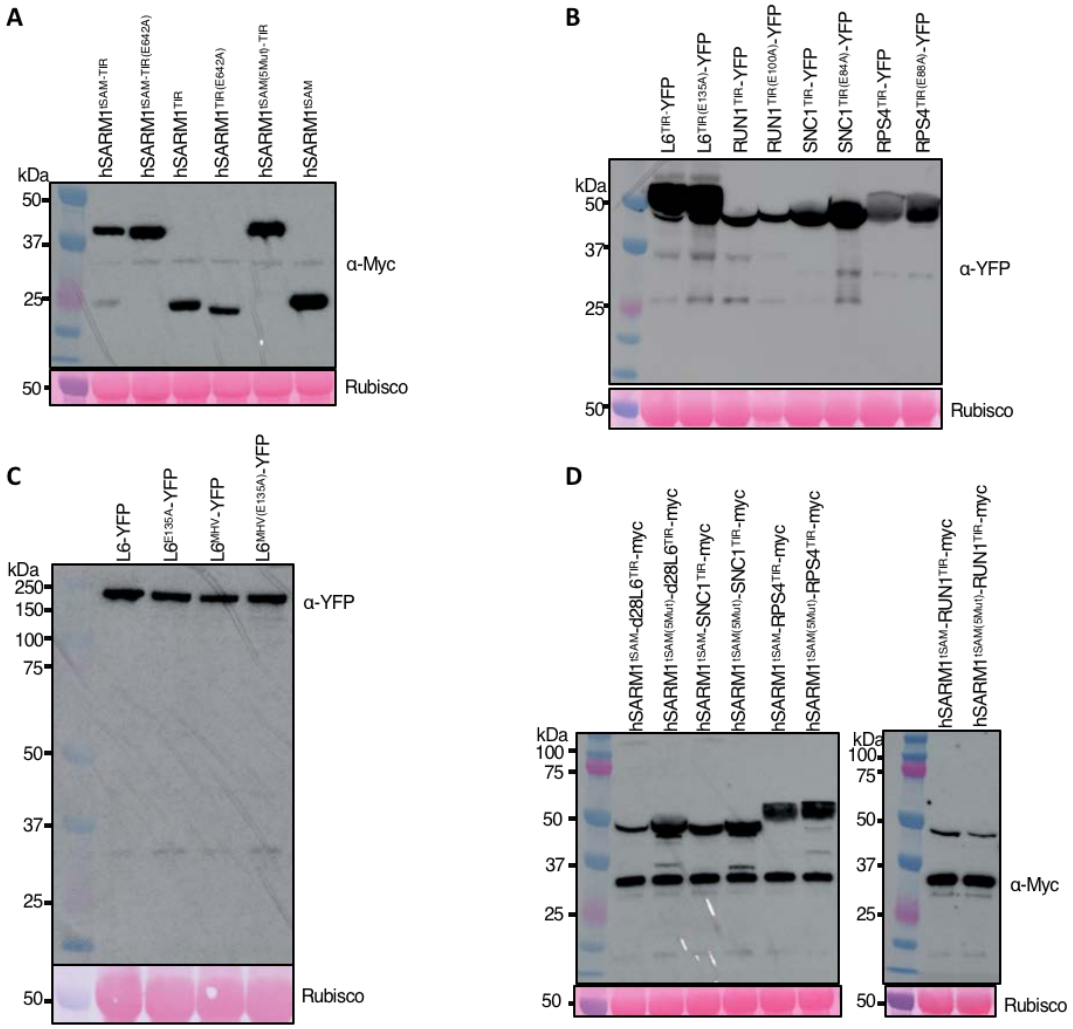

Fig. S27. Expression of proteins in plants. (**A**) Total proteins from *N. benthamiana* leaves with expression of Myc-fused hSARM1$^{tSAM\text{-}TIR}$, hSARM1$^{tSAM\text{-}TIR(E642A)}$, hSARM1^{TIR}, hSARM1$^{TIR(E642A)}$, hSARM1$^{tSAM(5Mut)\text{-}TIR}$ and hSARM1^{tSAM} were extracted and further immunoblotted with anti-Myc antibodies. Staining of RuBisCO with Ponceau S was used as a loading control. (**B**) Total proteins from *N. benthamiana* leaves with expression of YFP-fused L6^{TIR}, L6$^{TIR(E135A)}$, RUN1^{TIR}, RUN1$^{TIR(E100A)}$, SNC1^{TIR}, SNC1$^{TIR(E84A)}$, RPS4^{TIR}, and RPS4$^{TIR(E88A)}$ were extracted and further immunoblotted with anti-YFP antibodies. Staining of RuBisCO with Ponceau S was used as a loading control. (**C**) Total proteins from *N. tabacum* leaves with expression of YFP-fused L6, L6^{E135A}, L6^{MHV} and L6$^{MHV(E135A)}$ were extracted and further immunoblotted with anti-YFP antibodies. Staining of RuBisCO with Ponceau S was used as a loading control. (**D**) Total proteins from *N. benthamiana* leaves with expression of Myc-fused hSARM1^{tSAM}-d28L6^{TIR}, hSARM1$^{tSAM(5Mut)}$-d28L6^{TIR}, hSARM1^{tSAM}-SNC1^{TIR}, hSARM1$^{tSAM(5Mut)}$-SNC1^{TIR}, hSARM1^{tSAM}-RPS4^{TIR}, hSARM1$^{tSAM(5Mut)}$-RPS4^{TIR}, hSARM1^{tSAM}-RUN1^{TIR}, and hSARM1$^{tSAM(5Mut)}$-RUN1^{TIR}, were extracted and further immunoblotted with anti-Myc antibodies. Staining of RuBisCO with Ponceau S was used as a loading control.

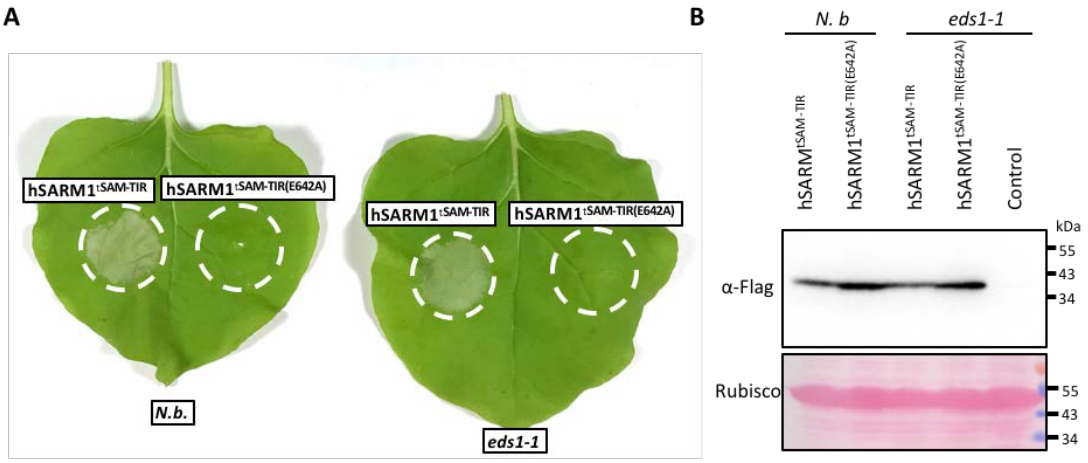

Fig. S28. Effect of EDS1 on hSARM1$^{tSAM\text{-}TIR}$-induced cell death in plants. (**A**) Hypersensitive response (HR) in leaves of wild-type (N.b.) and the eds1-1 *N. benthamiana* with agrobacterium-mediated transient expression of hSARM1$^{tSAM\text{-}TIR}$ and hSARM1$^{tSAM\text{-}TIR(E642A)}$. Images were taken 3 days post-infiltration. (**B**) Total protein from an eds1-1 leaf (control), or from N. b. and eds1-1 leaves with expression of Flag-fused hSARM1$^{tSAM\text{-}TIR}$ and hSARM1$^{tSAM\text{-}TIR(E642A)}$, was extracted and further immunoblotted with anti-Flag antibodies. Staining of RuBisCO with Ponceau S was used as a loading control.

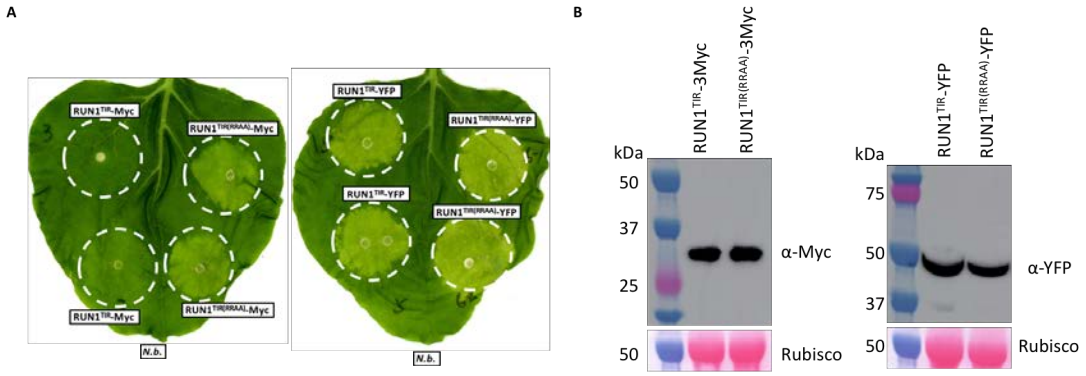

Fig. S29. Effect of R64A+R65A mutations on RUN1^{TIR}-induced cell death in plants. (A) Hypersensitive response (HR) in leaves of wild-type (N.b.) *N. benthamiana* with agrobacterium-mediated transient expression of RUN1^{TIR}-YFP, RUN1$^{TIR(RRAA)}$-YFP, RUN1^{TIR}-Myc and RUN1$^{TIR(RRAA)}$-Myc. Images were taken 3 days post-infiltration. (**B**) Total protein from the leaves, expressing the constructs as indicated, was extracted and further immunoblotted with antibodies, as indicated. Staining of RuBisCO with Ponceau S was used as a loading control.

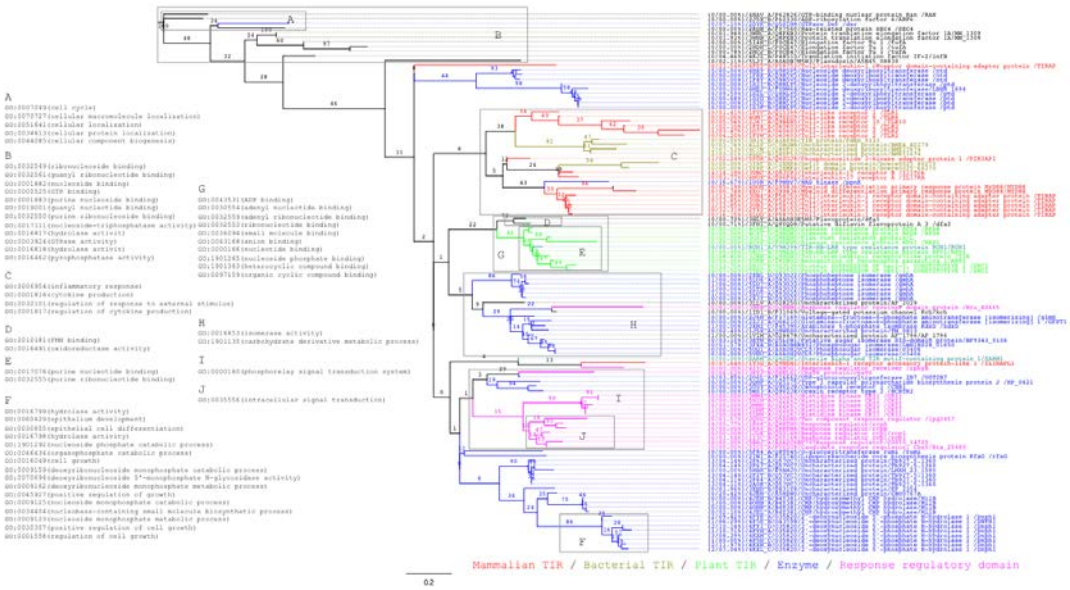

Fig. S30. Phylogenetic tree of proteins containing TIR domains and structurally-related domains. The phylogenetic tree includes 114 proteins from the intersection of DALI searches on hSARM1^{TIR} and RUN1^{TIR}. These proteins were superimposed by jCE (Java combinatorial extension (*92*)). Only non-redundant proteins with structures at 4 Å resolution or better and superpositions covering 125 residues or more in length were used. The tree was inferred by maximum likelihood using an evolutionary model of secondary structure developed by Lai et al. (*37*); this model is an adaptation of Dayhoff, Schwartz and Orcutt's original model of amino-acid changes. Numbers on branches are standard bootstrap values (by resampling 100 times). Sub-trees are colored to indicate kingdom and broad function, and annotated with Gene Ontology terms that are statistically enriched for the group of proteins at the leaves. Each leaf specifies PDB and UniProt identifiers, protein and gene names; in addition, the absolute number of mutated amino acids and the ratio of missing residues in the structure relative to the protein sequence are provided.

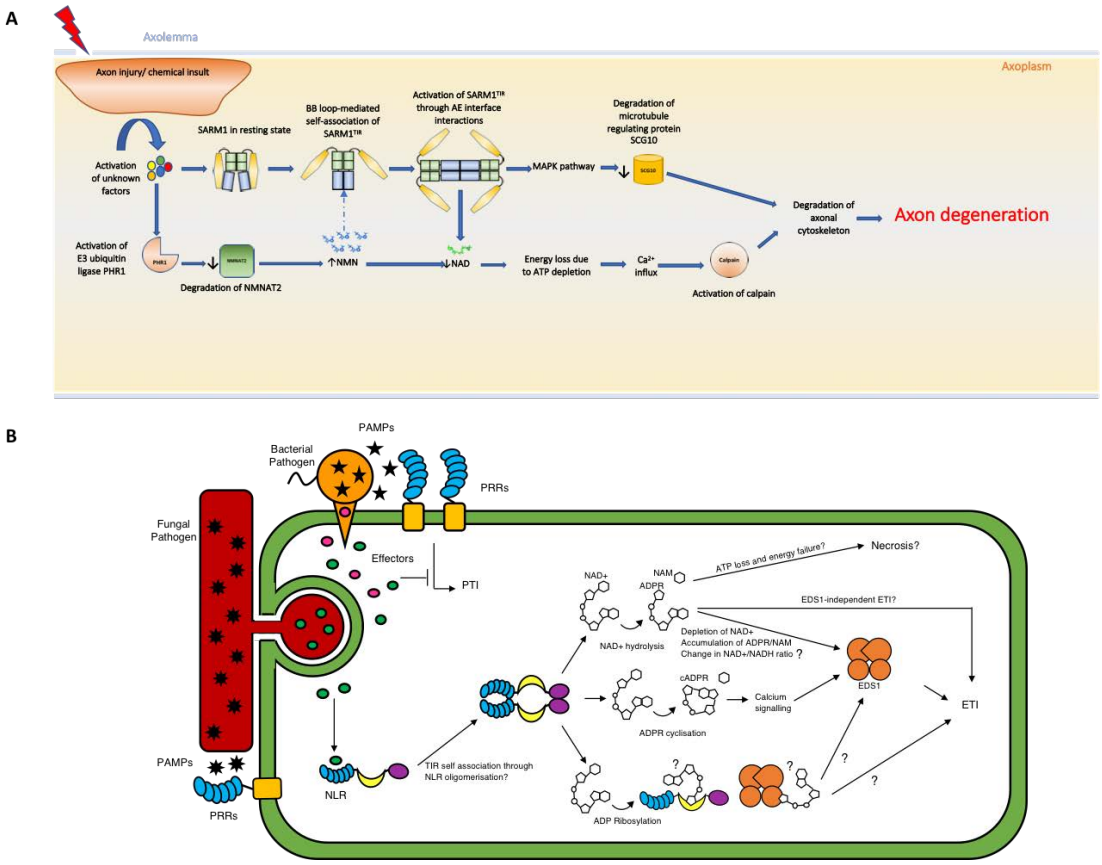

Fig. S31. Schematic models of hSARM1 and plant TIR domain functions. (**A**) SARM1 function in axon degeneration. (**B**) Potential functions for NAD^+ cleavage by plant TIR domain in plant immunity.

Supplementary Tables

Table S1. Crystallographic data.

	hSARM1^{tSAM}	hSARM1$^{tSAM(3M)}$	hSARM1^{TIR} :glycerol	hSARM1^{TIR} :ribose	hSARM1$^{TIR(G601P)}$ ("ligand-free")	hSARM1$^{TIR(G601P)}$:MES ("MES-bound")	hSARM1$^{TIR(H685A)}$	RUN1^{TIR}: NADP*:BisTris
Data collection								
Space group	I 1 2 1	I 1 2 1	P 2 2_1 2_1	P 2 2_1 2_1	P 2_1 2_1 2_1	P 2_1 2_1 2_1	P 1 2_1 1	C 1 2 1
Cell dimensions								
a, b, c (Å)	94.61, 154.46, 121.88	94.24, 154.08 120.99	33.06, 86.13, 116.76	32.99, 86.02, 116.73,	66.62, 80.10, 111.76	32.74, 54.14, 74.91	33.00, 71.31, 57.24	69.08, 79.40, 34.27
α, β, γ (°)	90, 93.82, 90	90, 94.55, 90	90, 90, 90	90, 90, 90	90, 90, 90	90, 90, 90	90, 97.52, 90	90, 107.42, 90
Resolution (Å)	95.55 - 2.70 (2.79 - 2.70)	47.49 - 2.80 (2.91 - 2.80)	48.33 - 1.80 (1.84 - 1.80)	48.33 - 1.80 (1.84 - 1.80)	46.56 - 2.07 (2.13 - 2.07)	43.88 1.67 (1.70 - 1.67)	44.40 - 3.03 (3.21 - 3.03)	39.70-1.75 (1.78-1.75)
Total reflections	174,053 (17,262)	129,699 (13,751)	229,464 (13,832)	236,306 (14,282)	501,965 (34,996)	113,515 (5456)	29,188 (4589)	122,888 (5707)
Unique reflections	47,692 (4,647)	41,934 (4,410)	31,910 (1902)	31,114 (1,803)	37, 025 (2,763)	16,080 (792)	5,181 (818)	17,742 (899)
Completeness (%)	99.6 (99.7)	99.0 (96.9)	100.0 (100.0)	98.0 (95.2)	99.8 (97.1)	99.9 (99.1)	99.85 (100.00)	99.6 (93.3)
Multiplicity	3.6 (3.7)	3.1 (3.1)	7.2 (7.3)	7.6 (7.9)	13.6 (12.7)	7.1 (6.9)	5.6 (5.6)	6.9 (6.3)
Wilson plot B (Å^2)	44.3	49.1	12.4	21.4	27.9	17.4	27.2	24.8
Rmeas (%)	11.3 (93.6)	18.2 (141.2)	22.0 (262.1)	8.8 (84.3)	11.5 (66.0)	5.0 (29.5)	30.6 (80.9)	8.4 (69.1)
Rmerge (%)	9.1 (77.8)	15.2 (118.5)	20.4 (243.5)	8.1 (79.4)	11.1 (63.4)	4.6 (27.3)	27.7 (73.2)	7.8 (63.6)
Rpim (%)	7.8 (64.9)	9.9 (76.0)	8.1 (96.3)	3.1 (29.9)	3.1(18.3)	1. 9 (11.1)	12.8 (34.0)	3.2 (26.7)
<I/σ(I)>	9.0 (1.7)	6.8 (1.3)	9.6 (1.0)	13.1 (2.3)	12.1 (2.7)	19.6 (4.9)	4.8 (1.8)	10.4 (1.4)
$CC_{1/2}$	0.997 (0.809)	0.988 (0.431)	0.996 (0.285)	0.999 (0.884)	0.998 (0.928)	0.999 (0.976)	0.971 (0.734)	0.997 (0.869)
Refinement								
Rwork (%)	20.45 (33.50)	20.09 (31.71)	18.92 (35.37)	17.18 (27.93)	19.14 (22.25)	18.50 (22.27)	18.43 (20.00)	16.67 (24.63)
Rfree (%)	22.64 (35.48)	23.73 (33.01)	23.16 (36.07)	21.00 (33.57)	22.97 (27.92)	23.10 (27.53)	23.44 (27.14)	19.49 (27.82)
Average B-factor (Å^2)	71.41	59.99	23.61	39.20	30.25	25.34	15.28	38.92
R.m.s. deviations								
Bond lengths (Å)	0.003	0.002	0.011	0.011	0.015	0.014	0.003	0.006
Bond angles (°)	0.62	0.51	1.00	1.01	1.49	1.41	0.54	0.74
Ramachandran plot (%)								
Favoured	97.12	97.73	97.10	97.83	97.27	97.81	96.74	97.60
Allowed	2.88	2.27	2.90	2.17	2.73	2.19	3.26	2.40
Outliers	0	0	0	0	0	0	0	0
PDB ID	6o0s	6o0t	6o0r	6o0q	6o0v	6o1b	6o0u	6o0w

The statistics were calculated using AIMLESS (*58*) and MolProbity (*63*).

Statistics for the highest-resolution shell are shown in parentheses.

$R_{merge} = \sum_{hkl}\sum_j |I_{hkl,j} - < I_{hkl} > |/(\sum_{hkl}\sum_j I_{hkl,j})$

R_{work} / $R_{free} = \sum_{hkl} \left|F_{hkl}^{obs} - F_{hkl}^{calc}\right| / (\sum_{hkl} F_{hkl}^{obs})$; R_{free} was calculated using randomly chosen 5-10 % fraction of data that was excluded from refinement.

Table S2. Proteins structurally similar to hSARM1^{tSAM}, based on program Dali.

hSARM1^{SAM1}			
PDB ID	Z score	RMSD (Å)	Description
3bs5	11.9	0.8	PROTEIN AVEUGLE
3bq7	11.3	1.1	DIACYLGLYCEROL KINASE DELTA
5j8y	11.1	1.2	POLYCOMB PROTEIN SCM
3tad	10.9	1.1	LIPRIN-ALPHA-2
5jti	10.6	1.5	TANKYRASE-1
4nl9	10.6	1.5	ANKYRIN REPEAT AND SAM DOMAIN-CONTAINING PROTEIN
5jrt	10.5	1.6	TANKYRASE-2
3tac	10.4	1.4	PERIPHERAL PLASMA MEMBRANE PROTEIN CASK
2f3n	10.4	1.2	SH3 AND MULTIPLE ANKYRIN REPEAT DOMAINS 3
4rqm	10.4	1.7	PROTEIN BICAUDAL C HOMOLOG 1
5zrz	10.3	1.5	EPHRIN TYPE-A RECEPTOR 5
4pzn	10.3	1.1	POLYHOMEOTIC-LIKE PROTEIN 3
3sen	10.2	1.4	CASKIN-1
1b4f	10.2	1.5	EPHB2
1b0x	10.1	1.5	EPHA4 RECEPTOR TYROSINE KINASE
5zrx	9.9	1.7	PHOSPHATIDYLINOSITOL 3,4,5-TRISPHOSPHATE 5-PHOSPHATASE 2
2ean	9.9	1.2	CONNECTOR ENHANCER OF KINASE SUPPRESSOR OF RAS 2
6brh	9.8	1.8	DEOXYNUCLEOSIDE TRIPHOSPHATE TRIPHOSPHOHYDROLASE
hSARM1^{SAM2}			
5zrx	10.3	1	PHOSPHATIDYLINOSITOL 3,4,5-TRISPHOSPHATE 5-PHOSPHATASE
5zry	10.1	1	ANKYRIN REPEAT AND SAM DOMAIN-CONTAINING PROTEIN

2qkq	10.1	1.1	EPHRIN TYPE-B RECEPTOR 4
3sen	9.8	1.2	CASKIN-1
4rqn	9.5	1.4	PROTEIN BICAUDAL C HOMOLOG 1
5jti	9.5	1.3	TANKYRASE-1
5l1m	9.4	1.3	CASKIN-2
4rqm	9.4	1.5	PROTEIN BICAUDAL C HOMOLOG 1
1b0x	9.2	1.1	EPHA4 RECEPTOR TYROSINE KINASE
2f44	9	1.4	SH3 AND MULTIPLE ANKYRIN REPEAT DOMAINS 3
5jrt	9	1.5	TANKYRASE-2
2k4p	9	1.3	PHOSPHATIDYLINOSITOL-3,4,5-TRISPHOSPHATE 5-PHOSPHATASE 2
2gle	10.4	1.9	NEURABIN-1
1kw4	10.4	1.5	POLYHOMEOTIC
5jti	10.3	1.5	TANKYRASE-1
4nl9	10.3	1.5	ANKYRIN REPEAT AND SAM DOMAIN-CONTAINING PROTEIN
1v85	10.2	1.9	SIMILAR TO RING FINGER PROTEIN 36
hSARM1^{tSAM} (both domains)			
3bs5	12.9	1	PROTEIN AVEUGLE
3bq7	12.5	1.1	DIACYLGLYCEROL KINASE DELTA
5j8y	12.3	1.2	POLYCOMB PROTEIN SCM
3bs7	12.2	1.7	PROTEIN AVEUGLE
4pzn	11.6	1.1	POLYHOMEOTIC-LIKE PROTEIN 3
3tad	11.6	5.6	LIPRIN-ALPHA-2
2f44	11.4	1.2	SH3 AND MULTIPLE ANKYRIN REPEAT DOMAINS 3
3tac	11.1	7.9	PERIPHERAL PLASMA MEMBRANE PROTEIN CASK
1pk1	11	1.4	POLYHOMEOTIC-PROXIMAL CHROMATIN PROTEIN

1pk3	10.9	1.3	SEX COMB ON MIDLEG CG9495-PA
2ean	10.9	3.2	CONNECTOR ENHANCER OF KINASE SUPPRESSOR OF RAS 2
6brh	10.7	3.7	DEOXYNUCLEOSIDE TRIPHOSPHATE TRIPHOSPHOHYDROLASE

Table S3. Interactions between SAM domains in the hSARM1^{tSAM} octamer.

hSARM1^{SAM1}: hSARM1^{SAM2} intramolecular interface							
Number	Surface region	Residue	Atom	Distance (Å)	Surface region	Residue	Atom
1	SAM1	Y479	OH	3.8	SAM2	R499	O
2	SAM1	T471	OG1	3.5	SAM2	Q500	OE1
3	SAM1	D441	OD1	2.4	SAM2	Y503	OH
4	SAM1	T475	O	3	SAM2	R499	NH1
5	SAM1	A477	O	2.9	SAM2	R499	NH1
6	SAM1	Y479	O	3	SAM2	C482	N
7	SAM1	Y479	O	3.7	SAM2	C482	SG
8	SAM1	Y479	O	2.8	SAM2	D483	N
9	SAM1	S480	O	3.3	SAM2	R484	NH1
hSARM1^{SAM1}:hSARM1^{SAM1} intermolecular interface							
Number	Surface region	Residue	Atom	Distance (Å)	Surface region	Residue	Atom
1	ML	R439	OD2	3.2	EH	R468	NH1
2	ML	Q436	OE1	2.4	EH	S459	OG
3	ML	D454	OD2	2.9	EH	G460	N
4	ML	D454	OD2	3.3	EH	I461	N
5	ML	E450	OE1	3.2	EH	K464	NZ
6	ML	R445	O	3	EH	K464	NZ
7	ML	Q437	OE1	3.3	EH	R465	NE
8	ML	Q437	O	3.2	EH	R465	NH1
9	ML	D439	OD2	3.7	EH	R465	NH1
10	ML	D439	OD1	3.3	EH	R468	NH1
11	ML	D441	OD2	2.8	EH	R468	NH1
12	ML	D439	OD2	3	EH	R468	NH2
13	ML	E450	OE2	2.9	EH	K464	NZ
14	ML	D441	OD2	4	EH	R468	NE
15	ML	Q436	OE1	3.7	EH	T462	OG1
hSARM1^{SAM2}:hSARM1^{SAM2} intermolecular interface							
Number	Surface region	Residue	Atom	Distance (Å)	Surface region	Residue	Atom
1	ML	Q522	NE2	3.5	EH	G532	O
2	ML	C508	O	3.3	EH	H534	NE2

3	ML	D526	OD1	3.1	EH	G532	N
4	ML	D526	OD2	3	EH	V533	N

Table S4: Proteins structurally similar to hSARM1^{TIR}, based on program Dali.

PDB ID	Z score	RMSD (Å)	Description
4w8g	16.2	2.2	TOLL-RECEPTOR-RELATED 2
5ku7	15.1	2.7	RPV1^{TIR}
5teb	14.1	2.5	RPP1^{TIR}
5y8f	13.7	2.5	SEFIR DOMAIN PROTEIN
5uzb	13.7	2.2	MAL^{TIR} FILAMENT
5h3c	13.5	2.4	SNC1^{TIR}
1o77	13.5	2.7	TOLL-LIKE RECEPTOR 2
4om7	13.3	2.8	TOLL-LIKE RECEPTOR 6
3jrn	13.3	2.2	AT1G72930 PROTEIN (AtTIR)
4c6r	13.2	2.6	RPS4^{TIR}
1t3g	13	2.7	X-LINKED INTERLEUKIN-1 RECEPTOR ACCESSORY
3ozi	13	2.9	L6^{TIR}
4c6t	12.8	2.6	RRS1^{TIR}
2j67	12.7	3	TOLL LIKE RECEPTOR 10
1fyv	12.4	2.7	TOLL-LIKE RECEPTOR 1
5for	11.9	2.5	PHOSPHOINOSITIDE 3-KINASE ADAPTER PROTEIN 1
3j0a	11.7	2.6	TOLL-LIKE RECEPTOR 5
4jem	11.3	2.9	CMP/HYDROXYMETHYL CMP HYDROLASE
4kxm	11.2	2.7	2'-DEOXYNUCLEOSIDE 5'-PHOSPHATE N-HYDROLASE 1
4fyi	11.1	2.7	DEOXYRIBONUCLEOSIDE 5'-MONOPHOSPHATE N-GLYCOSIDASE
3vbc	10.9	2.7	INTERLEUKIN-17 RECEPTOR B

4dom	10.8	2.9	MYELOID DIFFERENTIATION PRIMARY RESPONSE PROTEIN
4nux	10.6	2.6	INTERLEUKIN-17 RECEPTOR A
4jen	10.5	2.9	CMP N-GLYCOSIDASE
4c7m	9.3	3.4	TIR DOMAIN-CONTAINING PROTEIN (TcpB/BtpA)

Table S5: Inhibition of hSARM1$^{tSAM\text{-}TIR}$ by NAD$^+$ analogs. NR: nicotinamide riboside.

Compound	hSARM1$^{tSAM\text{-}TIR}$ IC_{50} (μM)
Nam	42
NR	30
NMN	60
cADPR	>100
NAD$^+$	71
NADH	>100

Table S6: Interactions in the crystals of hSARM1^{TIR}.

AE interface (nearly symmetric)							
Number	Surface region	Residue	Atom	Distance (Å)	Surface region	Residue	Atom
1	αA (chain B)	H685	NE2	2.8	αA (chain A)	Y568	OH
2	αA (chain B)	Q688	NE2	2.8	αA (chain A)	S578	OG
3	αA (chain B)	Q575	NE2	2.5	αA (chain A)	D658	OD2
4	αA (chain B)	R570	NH2	3.6	αA (chain A)	E686	OE1
5	αA (chain B)	Y568	OH	2.8	αA (chain A)	H685	NE2
6	αA (chain B)	Q575	OE1	3.5	αA (chain A)	W683	NE1
7	αA (chain B)	S578	OG	2.7	αA (chain A)	Q688	NE2
8	αA (chain B)	D658	OD2	2.7	αA (chain A)	Q575	NE2
9	αA (chain B)	E686	OE2	3.6	αA (chain A)	R570	NH2
10	αA (chain B)	W683	NE1	3.6	αA (chain A)	Q575	OE1
BB-loop interface (asymmetric)							
Number	Surface region	Residue	Atom	Distance (Å)	Surface region	Residue	Atom
1	BB loop	F603	N	3.4	DE loop	T677	O
2	BB loop	L598	O	3.4	βE	N679	ND2
3	BB loop	E599	O	3.1	βE	N679	ND2
4	BB loop	G601	O	2.9	βE	N679	N
Catalytic interface							
Number	Surface region	Residue	Atom	Distance (Å)	Surface region	Residue	Atom
1	-	Glycerol	O2	2.7	αE	E642	OE1
2	-	Glycerol	O2	3.7	βA	S567	OG
3	-	Glycerol	O1	2.6	αE	E642	OE2
4	-	Glycerol	O2	3	□A	Y568	N
5	-	Glycerol	O2	3.3	□A	Y568	O2

AE interface (nearly symmetric)							
Number	Surface region	Residue	Atom	Distance (Å)	Surface region	Residue	Atom
1	αA (chain B)	H685	NE2	2.8	αA (chain A)	Y568	OH
2	αA (chain B)	Q688	NE2	2.8	αA (chain A)	S578	OG
3	αA (chain B)	Q575	NE2	2.5	αA (chain A)	D658	OD2
4	αA (chain B)	R570	NH2	3.6	αA (chain A)	E686	OE1
5	αA (chain B)	Y568	OH	2.8	αA (chain A)	H685	NE2
6	αA (chain B)	Q575	OE1	3.5	αA (chain A)	W683	NE1
7	αA (chain B)	S578	OG	2.7	αA (chain A)	Q688	NE2
8	αA (chain B)	D658	OD2	2.7	αA (chain A)	Q575	NE2
9	αA (chain B)	E686	OE2	3.6	αA (chain A)	R570	NH2
10	αA (chain B)	W683	NE1	3.6	αA (chain A)	Q575	OE1

BB-loop interface (asymmetric)							
Number	Surface region	Residue	Atom	Distance (Å)	Surface region	Residue	Atom
1	BB loop	F603	N	3.4	DE loop	T677	O
2	BB loop	L598	O	3.4	βE	N679	ND2
3	BB loop	E599	O	3.1	βE	N679	ND2
4	BB loop	G601	O	2.9	βE	N679	N
Catalytic interface							
Number	Surface region	Residue	Atom	Distance (Å)	Surface region	Residue	Atom
1	-	Glycerol	O2	2.7	αE	E642	OE1
2	-	Glycerol	O2	3.7	βA	S567	OG
3	-	Glycerol	O1	2.6	αE	E642	OE2
4	-	Glycerol	O2	3	αA	Y568	N
5	-	Glycerol	O2	3.3	αA	Y568	O2

Table S7: Root-mean-squared fluctuations (RMSF) of binding-site residues of hSARM1^{TIR}, calculated from the final 20 ns of MD simulations.

Residue	Monomer RMSF (Å)	Hexamer RMSF (Å)
565	1.05	0.45
566	1.00	0.57
567	0.64	0.42
568	0.71	0.43
569	0.60	0.58
570	1.18	0.75
571	1.57	1.20
592	1.57	0.54
594	1.91	0.73
598	3.99	0.72
603	3.35	1.22
604	2.20	1.79
607	1.50	0.96
628	1.45	1.39
637	0.99	0.62
638	2.12	1.73
639	0.59	0.75
640	0.95	0.65
641	1.46	0.99
642	0.94	0.67

Table S8. Effects of mutations in other plant NLRs of residues analogous to the residues in the $NADP^+$/Bis-Tris binding site in $RUN1^{TIR}$.

NLR	Mutation position	RUN1 equivalent residue	Binding site	Assay host	Effect on TIR auto-activity	Effect on effector-dependent HR	Reference
RPV1							
	R36A	R39	$NADP^+$	*N. benthamiana*	Abolish	-	(*52*)
	W93A	W96	$NADP^+$	*N. benthamiana*	Abolish	-	(*52*)
	C94S	C97	Bis-Tris	*N. benthamiana*	Abolish	-	(*52*)
N							
	R24A	R39	$NADP^+$	*N. tabacum*	-	Abolish	(*93*)
	D45A	D60	Bis-Tris	*N. tabacum*	-	No effect	(*93*)
	K47A	K62	-	*N. tabacum*	-	No effect	(*93*)
	S80A	S94	$NADP^+$	*N. tabacum*	-	Abolish	(*93*)
	W82S/A	W96	$NADP^+$	*N. tabacum*	-	Partial loss of function	(*94*)
L6							
	R73A	R39	$NADP^+$	*L. usitatissimum*	Abolish	-	(*32*)
	K100A	R65	$NADP^+$	*L. usitatissimum*	Partial loss of function	-	(*32*)
	G101C	G66	-	*L. usitatissimum*	Abolish	-	(*32*)
	I104A	I69	-	*L. usitatissimum*	Abolish	-	(*32*)
	S129A	S94	$NADP^+$	*L. usitatissimum*	Abolish	-	(*32*)
	W131A	W96	$NADP^+$	*L. usitatissimum*	Abolish	-	(*32*)
	C132S	C97	Bis-Tris	*L. usitatissimum*	Abolish	-	(*32*)
RPS4							
	D49A	D60	Bis-Tris	*N. tabacum*	Abolish*	-	(*95*)
	R54N	R65	$NADP^+$	*N. tabacum*	Abolish*	-	(*95*)
	W84A	W96	$NADP^+$	*N. tabacum*	Increase*	-	(*95*)
	C85A	C97	Bis-Tris	*N. tabacum*	Abolish*	-	(*95*)
	E88A	E100	Bis-Tris	*N. tabacum*	Abolish*	-	(*95*)
RPP1-WsB							
	E158A	E100	Bis-Tris	*N. tabacum*	-	Abolish	(*96*)

References

1. T. Ve, S. J. Williams, B. Kobe, Structure and function of Toll/interleukin-1 receptor/resistance protein (TIR) domains. *Apoptosis* **20**, 250-261 (2015).
2. N. J. Gay, M. F. Symmons, M. Gangloff, C. E. Bryant, Assembly and localization of Toll-like receptor signalling complexes. *Nat. Rev. Immunol.* **14**, 546-558 (2014).
3. T. Ve, P. R. Vajjhala, A. Hedger, T. Croll, F. DiMaio, S. Horsefield, X. Yu, P. Lavrencic, Z. Hassan, G. P. Morgan, A. Mansell, M. Mobli, A. O'Carroll, B. Chauvin, Y. Gambin, E. Sierecki, M. J. Landsberg, K. J. Stacey, E. H. Egelman, B. Kobe, Structural basis of TIR-domain-assembly formation in MAL- and MyD88-dependent TLR4 signaling. *Nat. Struct. Mol. Biol.* **24**, 743-751 (2017).
4. P. R. Vajjhala, T. Ve, A. Bentham, K. J. Stacey, B. Kobe, The molecular mechanisms of signaling by cooperative assembly formation in innate immunity pathways. *Mol. Immunol.* **86**, 23-37 (2017).
5. S. Latty, J. Sakai, L. Hopkins, B. Verstak, T. Paramo, N. A. Berglund, N. J. Gay, P. J. Bond, D. Klenerman, C. E. Bryant, Activation of Toll-like receptors nucleates assembly of the MyDDosome signaling hub. *Elife* **7**, (2018).
6. X. Zhang, M. Bernoux, A. R. Bentham, T. E. Newman, T. Ve, L. W. Casey, T. M. Raaymakers, J. Hu, T. I. Croll, K. J. Schreiber, B. J. Staskawicz, P. A. Anderson, K. H. Sohn, S. J. Williams, P. N. Dodds, B. Kobe, Multiple functional self-association interfaces in plant TIR domains. *Proc. Natl. Acad. Sci. U. S. A.* **114**, E2046-E2052 (2017).
7. M. T. Nishimura, R. G. Anderson, K. A. Cherkis, T. F. Law, Q. L. Liu, M. Machius, Z. L. Nimchuk, L. Yang, E. H. Chung, F. El Kasmi, M. Hyunh, E. Osborne Nishimura, J. E. Sondek, J. L. Dangl, TIR-only protein RBA1 recognizes a pathogen effector to regulate cell death in Arabidopsis. *Proc. Natl. Acad. Sci. U. S. A.* **114**, E2053-E2062 (2017).
8. M. Carty, R. Goodbody, M. Schroder, J. Stack, P. N. Moynagh, A. G. Bowie, The human adaptor SARM negatively regulates adaptor protein TRIF-dependent Toll-like receptor signaling. *Nat. Immunol.* **7**, 1074-1081 (2006).
9. P. Panneerselvam, J. L. Ding, Beyond TLR signaling-the role of SARM in antiviral immune defense, apoptosis & development. *Int. Rev. Immunol.* **34**, 432-444 (2015).
10. J. M. Osterloh, J. Yang, T. M. Rooney, A. N. Fox, R. Adalbert, E. H. Powell, A. E. Sheehan, M. A. Avery, R. Hackett, M. A. Logan, J. M. MacDonald, J. S. Ziegenfuss, S. Milde, Y. J. Hou, C. Nathan, A. Ding, R. H. Brown, Jr., L. Conforti, M. Coleman, M. Tessier-Lavigne, S. Zuchner, M. R. Freeman, dSarm/Sarm1 is required for activation of an injury-induced axon death pathway. *Science* **337**, 481-484 (2012).
11. Y. Kim, P. Zhou, L. Qian, J. Z. Chuang, J. Lee, C. Li, C. Iadecola, C. Nathan, A. Ding, MyD88-5 links mitochondria, microtubules, and JNK3 in neurons and regulates neuronal survival. *J. Exp. Med.* **204**, 2063-2074 (2007).

12. J. Gerdts, E. J. Brace, Y. Sasaki, A. DiAntonio, J. Milbrandt, SARM1 activation triggers axon degeneration locally via NAD(+) destruction. *Science* **348**, 453-457 (2015).
13. P. N. Dodds, J. P. Rathjen, Plant immunity: towards an integrated view of plant-pathogen interactions. *Nat. Rev. Genet.* **11**, 539-548 (2010).
14. J. Gerdts, D. W. Summers, J. Milbrandt, A. DiAntonio, Axon self-destruction: new links among SARM1, MAPKs, and NAD+ metabolism. *Neuron* **89**, 449-460 (2016).
15. J. Wang, Q. Zhai, Y. Chen, E. Lin, W. Gu, M. W. McBurney, Z. He, A local mechanism mediates NAD-dependent protection of axon degeneration. *J. Cell Biol.* **170**, 349-355 (2005).
16. Y. Sasaki, T. Nakagawa, X. Mao, A. DiAntonio, J. Milbrandt, NMNAT1 inhibits axon degeneration via blockade of SARM1-mediated NAD(+) depletion. *Elife* **5**, (2016).
17. J. Gerdts, D. W. Summers, Y. Sasaki, A. DiAntonio, J. Milbrandt, Sarm1-mediated axon degeneration requires both SAM and TIR interactions. *J. Neurosci.* **33**, 13569-13580 (2013).
18. M. J. Knight, C. Leettola, M. Gingery, H. Li, J. U. Bowie, A human sterile alpha motif domain polymerizome. *Protein Sci.* **20**, 1697-1706 (2011).
19. F. Qiao, J. U. Bowie, The many faces of SAM. *Sci. STKE* **2005**, re7 (2005).
20. K. Essuman, D. W. Summers, Y. Sasaki, X. Mao, A. DiAntonio, J. Milbrandt, The SARM1 Toll/interleukin-1 receptor domain possesses intrinsic NAD+ cleavage activity that promotes pathological axonal degeneration. *Neuron* **93**, 1334-1343 e1335 (2017).
21. M. Bienz, Signalosome assembly by domains undergoing dynamic head-to-tail polymerization. *Trends Biochem. Sci.* **39**, 487-495 (2014).
22. L. Holm, L. M. Laakso, Dali server update. *Nucleic Acids Res.* **44**, W351-355 (2016).
23. Q. Zhang, C. M. Zmasek, X. Cai, A. Godzik, TIR domain-containing adaptor SARM is a late addition to the ongoing microbe-host dialog. *Dev. Comp. Immunol.* **35**, 461-468 (2011).
24. G. Pergolizzi, J. N. Butt, R. P. Bowater, G. K. Wagner, A novel fluorescent probe for NAD-consuming enzymes. *Chem. Commun.* **47**, 12655-12657 (2011).
25. S. Nimma, T. Ve, S. J. Williams, B. Kobe, Towards the structure of the TIR-domain signalosome. *Curr. Opin. Struct. Biol.* **43**, 122-130 (2017).
26. D. W. Summers, D. A. Gibson, A. DiAntonio, J. Milbrandt, SARM1-specific motifs in the TIR domain enable NAD+ loss and regulate injury-induced SARM1 activation. *Proc. Natl. Acad. Sci. USA* **113**, E6271-E6280 (2016).
27. N. Czudnochowski, A. L. Wang, J. Finer-Moore, R. M. Stroud, In human pseudouridine synthase 1 (hPus1), a C-terminal helical insert blocks tRNA from binding in the same orientation as in the Pus1 bacterial homologue TruA, consistent with their different target selectivities. *J. Mol. Biol.* **425**, 3875-3887 (2013).
28. Q. Liu, R. Graeff, I. A. Kriksunov, H. Jiang, B. Zhang, N. Oppenheimer, H. Lin, B. V. Potter, H. C. Lee, Q. Hao, Structural basis for enzymatic evolution from a dedicated ADP-ribosyl cyclase to a multifunctional NAD hydrolase. *J. Biol. Chem.* **284**, 27637-27645 (2009).

29. S. Han, J. A. Craig, C. D. Putnam, N. B. Carozzi, J. A. Tainer, Evolution and mechanism from structures of an ADP-ribosylating toxin and NAD complex. *Nat. Struct. Biol.* **6**, 932-936 (1999).
30. X. Zhang, P. N. Dodds, M. Bernoux, What do we know about NOD-like receptors in plant immunity? *Annu. Rev. Phytopathol.* **55**, 205-229 (2017).
31. Y. Gibon, F. Larher, Cycling assay for nicotinamide adenine dinucleotides: NaCl precipitation and ethanol solubilization of the reduced tetrazolium. *Anal. Biochem.* **251**, 153-157 (1997).
32. M. Bernoux, T. Ve, S. Williams, C. Warren, D. Hatters, E. Valkov, X. Zhang, J. G. Ellis, B. Kobe, P. N. Dodds, Structural and functional analysis of a plant resistance protein TIR domain reveals interfaces for self-association, signaling, and autoregulation. *Cell Host Microbe* **9**, 200-211 (2011).
33. M. Wiermer, B. J. Feys, J. E. Parker, Plant immunity: the EDS1 regulatory node. *Curr. Opin. Plant Biol.* **8**, 383-389 (2005).
34. A. Schultink, T. Qi, A. Lee, A. D. Steinbrenner, B. Staskawicz, Roq1 mediates recognition of the Xanthomonas and Pseudomonas effector proteins XopQ and HopQ1. *Plant J.* **92**, 787-795 (2017).
35. M. Bernoux, H. Burdett, S. J. Williams, X. Zhang, C. Chen, K. Newell, G. J. Lawrence, B. Kobe, J. G. Ellis, P. A. Anderson, P. N. Dodds, Comparative analysis of the flax immune receptors L6 and L7 suggests an equilibrium-based switch activation model. *Plant Cell* **28**, 146-159 (2016).
36. C. P. Ponting, R. R. Russell, The natural history of protein domains. *Annu. Rev. Biophys. Biomol. Struct.* **31**, 45-71 (2002).
37. J. S. Lai, B. Rost, B. Kobe, M. Boden, Evolutionary model of protein secondary structure capable of revealing new biological relationships. *bioRxiv*, (2019).
38. K. Essuman, D. W. Summers, Y. Sasaki, X. Mao, A. K. Y. Yim, A. DiAntonio, J. Milbrandt, TIR domain proteins are an ancient family of NAD(+)-consuming enzymes. *Curr. Biol.* **28**, 421-430 e424 (2018).
39. S. L. Chan, L. Y. Low, S. Hsu, S. Li, T. Liu, E. Santelli, G. Le Negrate, J. C. Reed, V. L. Woods, Jr., J. Pascual, Molecular mimicry in innate immunity: crystal structure of a bacterial TIR domain. *J. Biol. Chem.* **284**, 21386-21392 (2009).
40. M. Alaidarous, T. Ve, L. W. Casey, E. Valkov, D. J. Ericsson, M. O. Ullah, M. A. Schembri, A. Mansell, M. J. Sweet, B. Kobe, Mechanism of bacterial interference with TLR4 signaling by Brucella Toll/interleukin-1 receptor domain-containing protein TcpB. *J. Biol. Chem.* **289**, 654-668 (2014).
41. B. Kaplan-Turkoz, T. Koelblen, C. Felix, M. P. Candusso, D. O'Callaghan, A. C. Vergunst, L. Terradot, Structure of the Toll/interleukin 1 receptor (TIR) domain of the immunosuppressive Brucella effector BtpA/Btp1/TcpB. *FEBS Lett.* **587**, 3412-3416 (2013).
42. G. A. Snyder, D. Deredge, A. Waldhuber, T. Fresquez, D. Z. Wilkins, P. T. Smith, S. Durr, C. Cirl, J. Jiang, W. Jennings, T. Luchetti, N. Snyder, E. J. Sundberg, P. Wintrode, T. Miethke, T. S. Xiao, Crystal structures of the Toll/Interleukin-1 receptor (TIR) domains from the Brucella protein TcpB and host adaptor TIRAP reveal mechanisms of molecular mimicry. *J. Biol. Chem.* **289**, 669-679 (2014).
43. M. Matyszewski, W. Zheng, J. Lueck, B. Antiochos, E. H. Egelman, J. Sohn, Cryo-EM structure of the NLRC4(CARD) filament provides insights into

how symmetric and asymmetric supramolecular structures drive inflammasome assembly. *J. Biol. Chem.* **293**, 20240-20248 (2018).
44. L. Hunt, F. Lerner, M. Ziegler, NAD – new roles in signalling and gene regulation in plants. *New Phytol.* **163**, 31-44 (2004).
45. B. Gakière, J. Hao, L. De Bont, P. Pétriacq, A. Nunes-Nesi, A. R. Fernie, NAD+ biosynthesis and signaling in plants. *Crit. Rev. Plant Sci.* **2018**, 1-49 (2018).
46. N. J. Oppenheimer, A. J. Handlon, in *The Enzymes,* D. S. Sigman, Ed. (Academic Press, 1992).
47. H. C. Lee, Structure and enzymatic functions of human CD38. *Mol. Med.* **12**, 317-323 (2006).
48. M. Landau, I. Mayrose, Y. Rosenberg, F. Glaser, E. Martz, T. Pupko, N. Ben-Tal, ConSurf 2005: the projection of evolutionary conservation scores of residues on protein structures. *Nucleic Acids Res.* **33**, W299-302 (2005).
49. L. Stols, M. Gu, L. Dieckman, R. Raffen, F. R. Collart, M. I. Donnelly, A new vector for high-throughput, ligation-independent cloning encoding a tobacco etch virus protease cleavage site. *Protein Expr. Purif.* **25**, 8-15 (2002).
50. F. W. Studier, Protein production by auto-induction in high density shaking cultures. *Protein Expr. Purif.* **41**, 207-234 (2005).
51. T. Ve, S. Williams, E. Valkov, J. G. Ellis, P. N. Dodds, B. Kobe, Crystallization, X-ray diffraction analysis and preliminary structure determination of the TIR domain from the flax resistance protein L6. *Acta Crystallogr. Sect. F Struct. Biol. Cryst. Commun.* **67**, 237-240 (2011).
52. S. J. Williams, L. Yin, G. Foley, L. W. Casey, M. A. Outram, D. J. Ericsson, J. Lu, M. Boden, I. B. Dry, B. Kobe, Structure and function of the TIR domain from the grape NLR protein RPV1. *Front. Plant Sci.* **7**, 1850 (2016).
53. K. J. Schreiber, A. Bentham, S. J. Williams, B. Kobe, B. J. Staskawicz, Multiple domain associations within the Arabidopsis immune receptor RPP1 regulate the activation of programmed cell death. *PLoS Pathog.* **12**, e1005769 (2016).
54. L. Wan, X. Zhang, S. J. Williams, T. Ve, M. Bernoux, K. H. Sohn, J. D. Jones, P. N. Dodds, B. Kobe, Crystallization and preliminary X-ray diffraction analyses of the TIR domains of three TIR-NB-LRR proteins that are involved in disease resistance in Arabidopsis thaliana. *Acta Crystallogr. Sect. F Struct. Biol. Cryst. Commun.* **69**, 1275-1280 (2013).
55. N. C. Gassner, B. W. Matthews, Use of differentially substituted selenomethionine proteins in X-ray structure determination. *Acta Crystallogr. D Biol. Crystallogr.* **55**, 1967-1970 (1999).
56. T. M. McPhillips, S. E. McPhillips, H. J. Chiu, A. E. Cohen, A. M. Deacon, P. J. Ellis, E. Garman, A. Gonzalez, N. K. Sauter, R. P. Phizackerley, S. M. Soltis, P. Kuhn, Blu-Ice and the Distributed Control System: software for data acquisition and instrument control at macromolecular crystallography beamlines. *J. Syncrotron Radiat.* **9**, 401-406 (2002).
57. T. G. Battye, L. Kontogiannis, O. Johnson, H. R. Powell, A. G. Leslie, iMOSFLM: a new graphical interface for diffraction-image processing with MOSFLM. *Acta Crystallogr. D Biol. Crystallogr.* **67**, 271-281 (2011).
58. P. Evans, Scaling and assessment of data quality. *Acta Crystallogr. D Biol. Crystallogr.* **62**, 72-82 (2006).

59. M. D. Winn, C. C. Ballard, K. D. Cowtan, E. J. Dodson, P. Emsley, P. R. Evans, R. M. Keegan, E. B. Krissinel, A. G. Leslie, A. McCoy, S. J. McNicholas, G. N. Murshudov, N. S. Pannu, E. A. Potterton, H. R. Powell, R. J. Read, A. Vagin, K. S. Wilson, Overview of the CCP4 suite and current developments. *Acta Crystallogr. D Biol. Crystallogr.* **67**, 235-242 (2011).
60. P. D. Adams, D. Baker, A. T. Brunger, R. Das, F. DiMaio, R. J. Read, D. C. Richardson, J. S. Richardson, T. C. Terwilliger, Advances, interactions, and future developments in the CNS, Phenix, and Rosetta structural biology software systems. *Annu. Rev. Biophys.* **42**, 265-287 (2013).
61. A. J. McCoy, Solving structures of protein complexes by molecular replacement with Phaser. *Acta Crystallogr. D Biol. Crystallogr.* **63**, 32-41 (2007).
62. P. Emsley, B. Lohkamp, W. G. Scott, K. Cowtan, Features and development of Coot. *Acta Crystallogr. D Biol. Crystallogr.* **66**, 486-501 (2010).
63. V. B. Chen, W. B. Arendall, 3rd, J. J. Headd, D. A. Keedy, R. M. Immormino, G. J. Kapral, L. W. Murray, J. S. Richardson, D. C. Richardson, MolProbity: all-atom structure validation for macromolecular crystallography. *Acta Crystallogr. D Biol. Crystallogr.* **66**, 12-21 (2010).
64. W. Kabsch, XDS. *Acta Crystallogr. D Biol. Crystallogr.* **66**, 125-132 (2010).
65. N. Stein, CHAINSAW: a program for mutating pdb files used as templates in molecular replacement. *J. Appl. Cryst.* **41**, 641-643 (2008).
66. A. Feechan, C. Anderson, L. Torregrosa, A. Jermakow, P. Mestre, S. Wiedemann-Merdinoglu, D. Merdinoglu, A. R. Walker, L. Cadle-Davidson, B. Reisch, S. Aubourg, N. Bentahar, B. Shrestha, A. Bouquet, A. F. Adam-Blondon, M. R. Thomas, I. B. Dry, Genetic dissection of a TIR-NB-LRR locus from the wild North American grapevine species Muscadinia rotundifolia identifies paralogous genes conferring resistance to major fungal and oomycete pathogens in cultivated grapevine. *Plant J.* **76**, 661-674 (2013).
67. E. Krissinel, K. Henrick, Inference of macromolecular assemblies from crystalline state. *J. Mol. Biol.* **372**, 774-797 (2007).
68. J. Wen, T. Arakawa, J. S. Philo, Size-exclusion chromatography with on-line light-scattering, absorbance, and refractive index detectors for studying proteins and their interactions. *Anal. Biochem.* **240**, 155-166 (1996).
69. P. V. Konarev, M. V. Petoukhov, V. V. Volkov, D. I. Svergun, ATSAS 2.1, a program package for small-angle scattering data analysis. *J. Appl. Crystallogr.* **39**, 277-286. (2006).
70. R. P. Rambo, J. A. Tainer, Accurate assessment of mass, models and resolution by small-angle scattering. *Nature* **496**, 477-481 (2013).
71. D. Franke, M. V. Petoukhov, P. V. Konarev, A. Panjkovich, A. Tuukkanen, H. D. T. Mertens, A. G. Kikhney, N. R. Hajizadeh, J. M. Franklin, C. M. Jeffries, D. I. Svergun, ATSAS 2.8: a comprehensive data analysis suite for small-angle scattering from macromolecular solutions. *J. Appl. Crystallogr.* **50**, 1212-1225 (2017).
72. N. R. Hajizadeh, D. Franke, C. M. Jeffries, D. I. Svergun, Consensus Bayesian assessment of protein molecular mass from solution X-ray scattering data. *Sci. Rep.* **8**, 7204 (2018).
73. J. Gilley, M. P. Coleman, Endogenous Nmnat2 is an essential survival factor for maintenance of healthy axons. *PLoS Biol.* **8**, e1000300 (2010).

74. C. Y. Chen, C. W. Lin, C. Y. Chang, S. T. Jiang, Y. P. Hsueh, Sarm1, a negative regulator of innate immunity, interacts with syndecan-2 and regulates neuronal morphology. *J. Cell Biol.* **193**, 769-784 (2011).
75. H. Inoue, H. Nojima, H. Okayama, High efficiency transformation of Escherichia coli with plasmids. *Gene* **96**, 23-28 (1990).
76. A. Buchholz, R. Takors, C. Wandrey, Quantification of intracellular metabolites in Escherichia coli K12 using liquid chromatographic-electrospray ionization tandem mass spectrometric techniques. *Anal. Biochem.* **295**, 129-137 (2001).
77. M. Bernoux, T. Timmers, A. Jauneau, C. Briere, P. J. de Wit, Y. Marco, L. Deslandes, RD19, an Arabidopsis cysteine protease required for RRS1-R-mediated resistance, is relocalized to the nucleus by the Ralstonia solanacearum PopP2 effector. *Plant Cell* **20**, 2252-2264 (2008).
78. P. N. Dodds, G. J. Lawrence, A. M. Catanzariti, M. A. Ayliffe, J. G. Ellis, The Melampsora lini AvrL567 avirulence genes are expressed in haustoria and their products are recognized inside plant cells. *Plant Cell* **16**, 755-768 (2004).
79. W. Sherman, T. Day, M. P. Jacobson, R. A. Friesner, R. Farid, Novel procedure for modeling ligand/receptor induced fit effects. *J. Med. Chem.* **49**, 534-553 (2006).
80. R. A. Friesner, J. L. Banks, R. B. Murphy, T. A. Halgren, J. J. Klicic, D. T. Mainz, M. P. Repasky, E. H. Knoll, M. Shelley, J. K. Perry, D. E. Shaw, P. Francis, P. S. Shenkin, Glide: a new approach for rapid, accurate docking and scoring. 1. Method and assessment of docking accuracy. *J. Med. Chem.* **47**, 1739-1749 (2004).
81. T. A. Halgren, R. B. Murphy, R. A. Friesner, H. S. Beard, L. L. Frye, W. T. Pollard, J. L. Banks, Glide: a new approach for rapid, accurate docking and scoring. 2. Enrichment factors in database screening. *J. Med. Chem.* **47**, 1750-1759 (2004).
82. M. P. Jacobson, R. A. Friesner, Z. Xiang, B. Honig, On the role of the crystal environment in determining protein side-chain conformations. *J. Mol. Biol.* **320**, 597-608 (2002).
83. M. Abraham, T. Murtola, R. Schulz, S. Páll, J. C. Smith, B. Hess, E. Lindahl, GROMACS: High performance molecular simulations through multi-level parallelism from laptops to supercomputers. *SoftwareX* **1-2**, 19-25 (2015).
84. V. Hornak, R. Abel, A. Okur, B. Strockbine, A. Roitberg, C. Simmerling, Comparison of multiple Amber force fields and development of improved protein backbone parameters. *Proteins* **65**, 712-725 (2006).
85. S. Páll, B. Hess, A flexible algorithm for calculating pair interactions on SIMD architectures. *Comput. Phys. Commun.* **184**, 2641–2650 (2013).
86. T. Darden, D. York, L. Pedersen, Particle mesh Ewald (PME): a N log(N) method for Ewald sums in large systems. *J. Chem. Phys.* **98**, 10089–10092 (1993).
87. U. Essmann, L. Perera, M. L. Berkowitz, T. Darden, H. Lee, L. G. Pedersen, A smooth particle mesh Ewald method. *J. Chem. Phys.* **103**, 8577–8593 (1995).
88. H. J. C. Berendsen, J. P. M. Postma, W. F. van Gunsteren, A. DiNola, J. R. Haak, Molecular dynamics with coupling to an external bath. *J. Chem. Phys.* **81**, 3684 (1984).

89. B. Hess, P-LINCS: A Parallel Linear Constraint Solver for molecular simulation. *J. Chem. Theory Comput.* **4**, 116-122 (2008).
90. S. Unni, Y. Huang, R. M. Hanson, M. Tobias, S. Krishnan, W. W. Li, J. E. Nielsen, N. A. Baker, Web servers and services for electrostatics calculations with APBS and PDB2PQR. *J. Comput. Chem.* **32**, 1488-1491 (2011).
91. S. J. Williams, K. H. Sohn, L. Wan, M. Bernoux, P. F. Sarris, C. Segonzac, T. Ve, Y. Ma, S. B. Saucet, D. J. Ericsson, L. W. Casey, T. Lonhienne, D. J. Winzor, X. Zhang, A. Coerdt, J. E. Parker, P. N. Dodds, B. Kobe, J. D. Jones, Structural basis for assembly and function of a heterodimeric plant immune receptor. *Science* **344**, 299-303 (2014).
92. A. Prlic, S. Bliven, P. W. Rose, W. F. Bluhm, C. Bizon, A. Godzik, P. E. Bourne, Pre-calculated protein structure alignments at the RCSB PDB website. *Bioinformatics* **26**, 2983-2985 (2010).
93. P. Mestre, D. C. Baulcombe, Elicitor-mediated oligomerization of the tobacco N disease resistance protein. *Plant Cell* **18**, 491-501 (2006).
94. S. P. Dinesh-Kumar, W. H. Tham, B. J. Baker, Structure-function analysis of the tobacco mosaic virus resistance gene N. *Proc. Natl. Acad. Sci. USA* **97**, 14789-14794 (2000).
95. M. R. Swiderski, D. Birker, J. D. Jones, The TIR domain of TIR-NB-LRR resistance proteins is a signaling domain involved in cell death induction. *Mol. Plant Microbe Interact.* **22**, 157-165 (2009).
96. K. V. Krasileva, D. Dahlbeck, B. J. Staskawicz, Activation of an Arabidopsis resistance protein is specified by the in planta association of its leucine-rich repeat domain with the cognate oomycete effector. *Plant Cell* **22**, 2444-2458 (2010).